Organic Photovoltaics and Concentrators

by

Jonathan King Mapel

S.M. Electrical Engineering and Computer Science
Massachusetts Institute of Technology, 2006

B.S. Electrical Engineering
University of Southern California, 2003

SUBMITTED TO THE DEPARTMENT OF ELECTRICAL ENGINEERING AND COMPUTER SCIENCE IN PARTIAL FULFILLMENT FOR THE DEGREE OF

DOCTORATE OF PHILOSOPHY IN
ELECTRICAL ENGINEERING AND COMPUTER SCIENCE
AT THE
MASSACHUSETTS INSTITUTE OF TECHNOLOGY

JUNE 2008

Signature of Author:_____
Department of Electrical Engineering and Computer Science
May 29, 2008

Certified by:_____
Marc A. Baldo
Esther and Harold Edgerton Assistant Professor of
Electrical Engineering and Computer Science
Thesis Supervisor

Accepted by:_____
Terry P. Orlando
Chairman, Department Committee on Graduate Students
Electrical Engineering and Computer Science

Organic Photovoltaics and Concentrators

by

Jonathan King Mapel

Submitted to the Department of Electrical Engineering and Computer Science
on May 29, 2008 in partial fulfillment of the
requirements for the degree of
Doctorate of Philosophy in Electrical Engineering and Computer Science

ABSTRACT

The separation of light harvesting and charge generation offers several advantages in the design of organic photovoltaics and organic solar concentrators for the ultimate end goal of achieving a lower cost solar electric conversion. In this work, we explore two new device architectures.

In antenna organic solar cells, we utilize external energy transfer mediated by surface plasmon polaritons to increase the efficiency of existing organic photovoltaic devices limited in performance by the exciton diffusion bottleneck. This unique architecture is analyzed for its functionality and the efficiencies of each added step is quantified. Although the introduction of additional energy transduction will ultimately introduce more losses, bypassing the exciton diffusion bottleneck offers the potential for increased efficiency through judicious device design.

We also seek to enable the use of high efficiency inorganic solar cells in organic solar concentrators which aim to exploit high performance of the PV cells in low cost, non-tracking configurations. By utilizing thin films of organic chromophores on high refractive index glass substrates, we are able to apply the recent advances of organic optoelectonics to the fluorescent concentrator platform, including near field energy transfer, solid state solvation, and phosphorescence. By reducing self-absorption losses, we demonstrate optical flux gains an order of magnitude greater than previously published results and thereby reduce the effective cost of inorganic solar cells by at least a factor of ten. Combined with the potential for low cost solution processing, the high flux gains and power efficiencies realized here should enable a new source of inexpensive solar power.

Thesis Supervisor: Marc A. Baldo
Title: Associate Professor of Electrical Engineering and Computer Science

Acknowledgements

I am wholly indebted to my research advisor, Marc Baldo, whose sound guidance and openness to exploratory deviations contributed to making my graduate studies challenging and pleasurable. He was always available to discuss new ideas in all fields of thought and fully encouraged me to take risks to push the boundary of what is possible.

I would further like to thank everyone I've worked with in the Soft Semiconductor Group. High standards are contagious and I've grown immensely though our time together. We've left an indelible mark on each other and I look forward to keeping strong connections to everyone I've worked with along the way. Through my time at MIT I've become affected with the passion to invent, an affliction I hope to never lose.

Engaging with the whole MIT community has been a genuinely rewarding experience. From my first day I've been continuously amazed by the talented, intelligent, and passionate people that have surrounded me. I firmly believe that these are the conditions where one can truly grow.

I also thank the research foundations, organizations, and kind sponsors whose support helped me and continues to help push the scientific envelope for the whole world: the Link Foundation for Energy, the Martin Family Society for Sustainability, the Arunas Chessonis Foundation, the ARCS Foundation, the UC Davis Center for Entrepreneurship, Total Energie, Centre National de la Recherche Scientifique (France), the Air Force Office of Scientific Research, the Defense Advanced Research Projects Agency, the National Science Foundation, and the Department of Energy.

My deepest gratitude is reserved for Audrey, my strength and my sustenance, whose presence was always felt no matter the working distance. Our common passion to understand the world and affect it for the better drove and continues to drive me.

Jonathan Mapel,
Cambridge,
May 5, 2008

List of Publications, Conference Contributions, and Patents

Publications

1. “Organic solar concentrators employing phycobilisomes,” C.L. Mulder, L. Theogarajan, M.J. Currie, **J.K. Mapel**, M.A. Baldo. *In preparation*, 2008.
2. “Organic solar concentrators utilizing perylenes,” S. Goffri, **J.K. Mapel**, M.A. Baldo. *In preparation*, 2008.
3. “High efficiency organic solar concentrators,” **J.K. Mapel**, M.J. Currie, T.D. Heidel, S. Goffri, M.A. Baldo. *Submitted*, 2008.
4. “Analysis of surface plasmon polariton mediated energy transfer in organic photovoltaic devices” T. D. Heidel, **J.K Mapel**, K. Celebi, M. Singh, M.A. Baldo, Proceedings of the Society of Photo-Optical Instrumentation Engineers (SPIE), **6656**, 66560I1-8, (2007).
5. “Surface plasmon polariton mediated energy transfer in organic photovoltaic devices,” **J.K. Mapel**, T.D. Heidel, M. Singh, K. Celebi, and M.A. Baldo, Applied Physics Letters, 91 , 093506 (2007).
6. “Plasmonic excitation of organic double heterostructure solar cells,” **J.K. Mapel**, K. Celebi, M. Singh, and M.A. Baldo.” Applied Physics Letters 90, 121102 (2007).
7. "The Application of Photosynthetic Materials and Architectures to Solar Cells," **J.K. Mapel** and M.A. Baldo. Chapter in *Nanostructured Materials for Solar Energy Conversion*, ed. T. Soga (Elsevier, Amsterdam, 2006).
8. “Effects of film morphology and gate dielectric surface preparation on the electrical characteristics of organic-vapor-phase-deposited pentacene thin-film transistors,” M. Shtein, **J.K. Mapel**, J.B. Benziger, S.R. Forrest, Applied Physics Letters, 81(2) , 268-280 (2002).

Conference Contributions

1. "Increased indoor light harvesting efficiency utilizing luminescent solar concentrators," T.D. Heidel, M.J. Currie, **J.K. Mapel**, S. Goffri, M.A. Baldo. International Solid State Circuits Conference, 2008.
2. "High efficiency organic solar concentrators." **J.K. Mapel**, M.J. Currie, S. Goffri, M.A. Baldo. Electronic Materials Conference (The Metals, Minerals, and Materials Society), Santa Barbara, CA. June 2008.
3. "Luminescent solar concentrators using optimized resonant energy transfer." M.J. Currie, **J.K. Mapel**, S. Goffri, M.A. Baldo. Meeting of the Materials Research Society, San Francisco, CA. March 2008.
4. "Organic solar concentrators." **J.K. Mapel**. MIT Microsystems Technology Laboratory Annual Research Review. New Hampshire, January 2008. *Winner, Best Presentation.*
5. "Surface plasmon polariton mediated energy transfer in organic photovoltaic devices ," T.D. Heidel, **J.K. Mapel**, K. Celebi, M. Singh, M.A. Baldo. Electronic Materials Conference (The Metals, Minerals, and Materials Society), Notre Dame, IN. June 2007.
6. "Photosynthetic solar cells, organic semiconductor solar cells, and diffuse solar concentrators." **J.K. Mapel**, M.A. Baldo. Meeting of the Alliance for Global Sustainability. Barcelona, Spain. March 2007.
7. "External energy transfer into organic photovoltaic devices**." J.K. Mapel**. Department seminar at *L'Ecole Polytechnique*, Palaiseau, France. February, 2007.
8. "Photosynthetic solar cells." **J.K. Mapel**. T.D. Heidel, K. Celebi, M. Currie, M. Singh, M.A. Baldo. Energy Nanotechnology International (American Society for Mechanical Engineers) June 2006. *Winner, Best Poster.*
9. "Organic photovoltaics with external antennas." **J.K. Mapel**, T.D. Heidel, K. Celebi. M.A. Baldo. Electronic Materials Conference (The Metals, Minerals, and Materials Society), State College, PA. June 2006.
10. "External energy transfer in organic photovoltaics." **J.K Mapel**, T.D. Heidel, K.Celebi, M. Singh, M.A. Baldo. Meeting of the Materials Research Society, Boston, MA. December 2005.
11. "Photosynthesis inspired redesign of organic photovoltaics." **J.K. Mapel**. Center for Integrated Photonic Systems (Seminar), Massachusetts Institute of Technology. April 2005.

Patents

1. "Solar concentrators and device and methods using them," Filed US 61/020,946, January 2008.
2. "Photovoltaic cell," Filed US 20070119496, November 2005.

Contents

Figures

Chapter 1 The Solar Motivation

1.1 Solar power

Global energy demand is projected to double by mid-century.[1] Incremental improvement in existing energy infrastructures and technologies will not satisfy these needs in a sustainable way. Procuring adequate energy supplies without large carbon dioxide emissions is one of society's most pressing challenges. Without viable pathways for addressing these demands, the world's economic, technological, and political horizons will be severely limited. Solar power is unique in that it could singly supply the enormous power requirements of mankind without widespread degradation to the global environment.

Sunlight is by far the largest of all carbon-neutral energy sources. More energy from sunlight strikes the Earth in one hour (4.3×10^{20} J) than all the energy consumed on the planet in a year (4.1×10^{20} J).[2] It also has a successful track record; through photosynthesis, it has powered the earth for billions of years and is responsible for our atmosphere and all forms of life. Annual worldwide solar energy conversion in photosynthetic bacteria and plants corresponds to ten times the amount used by all of mankind. Drawing energy from the sun does not deplete its energy potential, which will continue over astronomical timescales. The sun is a remote fusion reactor and, through the solar cycle, runs without our need to maintain its operation, infrastructure, or waste

products. In addition, the sun is unique in that it is a widely distributed resource, available to all and blind to geographical and geological luck. Unlike other energy supplies, it cannot be hoarded, traded, or used to extort. Solar power single handedly possesses the long term potential to provide enough energy to power all of humanity with reasonable amounts of infrastructure.[†]

1.2 Solar electricity

Energy is consumed by humanity in multiple forms, but one of the most useful and portable is electricity. This work is primarily concerned with the transduction of light to electrical power though the photovoltaic (PV) effect in semiconductors. Edmund Becquerel discovered the PV effect in the mid-nineteenth century, when he observed that a voltage and a current were produced when a silver chloride electrode immersed in an electrolyte and connected to another metal electrode was illuminated with light.[3] The birth of the modern era of PV solar cells occurred in 1954 as Bell Labs demonstrated solar cells based on p-n junctions in silicon.[4]

Although substantial gains in solar cell technical performance have been achieved in the past fifty years, widespread adoption of solar cells remains limited by their high cost per Watt of generated power ($/$W_P$). Power conversion efficiencies in well engineered systems have reached 80-90% of their thermodynamic limits.[5] The primary

[†] A note on land use: For latitudes in the United States, a 10% efficient solar energy "farm" covering 1.6% of the U.S. land area would meet the entirety of domestic energy needs. For comparison, the required land area is about ten times the area of all single-family residential rooftops and is comparable with the land area covered by national highways.[2]

challenge is achieving high efficiencies in cost competitive systems. Their cost per Watt must be reduced by a factor of three to ten to compete with fossil and nuclear electricity.

The disparity in cost between solar electricity and its alternatives has largely limited its deployment, although the discrepancy has diminished over time. In 2001, solar power accounted for less than 0.1% of global electricity generation and has grown in total capacity at a rate of 45% annually over the last decade.[6] This is largely due to increases in efficiencies and reductions in manufacturing costs, drawing heavily upon the advances of the semiconductor industry and catalyzed by government support.

In 2006, 2.2 GW_P of solar cells were installed.[6] This capacity was heavily comprised of silicon PV in its several forms; see Figure 1.1. Thin film technologies currently account for 8.3% of capacity, but this market share is forecasted to increase to 20% by 2012 due to polysilicon supply constraints.[7] The average module level production cost was \$2.89/W_P. However, solar cells compete on installed system price, which includes the balance of systems costs (grid-tie inverter, charge controller, circuit breaker, cables, mounting frames, and miscellaneous accessories) and other installation costs (real estate, labor, warranties, and maintenance). These extra costs are much larger than the module costs, and the average system level price was \$7.50/W_P.[7]

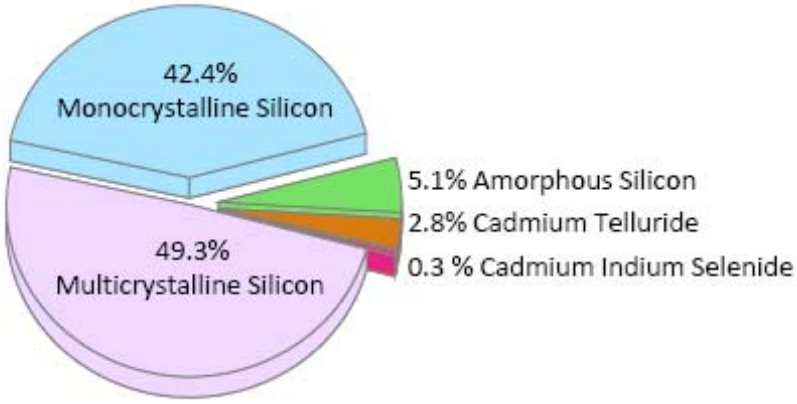

Figure 1.1 Installed PV capacity by technology in 2006.

Amorphous silicon is the most mature of thin film technologies. Over the last several years, cadmium telluride has rapidly grown in importance and will soon overtake amorphous silicon in capacity and is forecasted to approach 20% of total PV capacity market share around 2012. As of 2007, there were 24 companies actively pursuing amorphous silicon technology, 7 pursuing cadmium telluride, and 16 pursuing cadmium indium gallium selenide. [7] Market segmentation from Solarbuzz[6].

These high prices partially reflect the very high demand for solar electricity coinciding with polysilicon supply shortages. Prices are expected to decrease over the next few years as polysilicon supplies increase, independent of technical and manufacturing improvements. But they provide a comparison point for how far solar costs need to decrease. To be competitive with electricity across large parts of the United States, system level prices need to drop below $\$1/W_P$,[8] indicating that an order of magnitude levels of cost reductions are needed. Although significant cost reductions can occur through scaling[9] and incremental technical improvements, there is much need for technological paradigm shifts to make solar economical.

There are two major new technology shifts that have the potential for significant cost reductions: thin film and concentrator solar cells. Recent technical advances show

great promise and their relative importance should grow in the coming years. To motivate the work described in this thesis, we will review the cost models for these two technologies. They are useful in highlighting the technological improvements that perhaps hold the greatest potential real world impact. Together, they represent two methods for decreasing the most expensive components of the solar module: high-quality semiconductors.

1.3 Thin film solar cells

The great promise of thin films is that they are comprised mostly of low cost materials (glass, metal, plastic) and very little high-cost semiconductor. If semiconductor active layers thicknesses can be reduced to microns, large areas can be coated with very little material. A micron of semiconductor over 1 m^2 is possible with about 5 g of material. Even if the starting material is expensive, ($1,000-5,000/kg), this may translate to $0.03-0.15/$W_P$. This idea, although simple, has been frustrated by the absence of semiconductors that both work at high enough efficiency and are manufacturable cheaply at large scales at high yield.

The two major thin film solar cell technologies that are promising candidates for achieving low cost solar are cadmium telluride (CdTe) and cadmium indium gallium selenide (CIGS). There are numerous companies pursuing the development and commercialization of each. They are typically possess lower conversion efficiencies (9-13%) than their crystalline silicon counterparts (12-18%), but their primarily advantage is that they are manufacturable with lower cost processing (chemical vapor deposition or printing) using much less material (≈1 micron active layers instead of hundreds of

micron-thick wafers) deposited on low cost substrates (glass or plastic). Their lower conversion efficiency can be competitive in the important $/W$_P$ metric if their manufacturing costs are low.

First Solar is has been very successful in commercializing their cadmium telluride thin film technology at a cost less than half ($1.25/W$_P$) of the market average for crystalline silicon ($2.89/W$_P$), which comprises over 92% of the market. This significant achievement has catalyzed their rapid growth, with analysts forecasting their market share to increase from 2.5% to 10% in ~3 years.[10]

A detailed cost model was published by Zweibel at the U.S. National Renewable Energy Laboratory outlining the production level materials cost breakdown for First Solar's cadmium telluride manufacturing process in 2000;[11,12] see Table 1.1. It is useful in that it demonstrates where the major costs reside and how proposed technical alternatives will affect those costs. In addition to these direct costs, indirect manufacturing costs can be substantial, including capital, labor, factory rent, overhead, utilities, R&D, and maintenance.

An interesting characteristic of this model is that the manufacturers of cadmium telluride solar cells have managed to reduce the cost of the expensive semiconductors to only roughly 10% of the total materials cost, comparable in magnitude to the shipping carton or encapsulant. Even if First Solar were able to eliminate this cost entirely, the relative module cost decrease would be approximately 4%. We also note that the cost of the transparent conductor that serves as a top electrode is 50% more expensive than the active semiconductors and presents a target for elimination. We can conclude that any alternative technology that is equivalent excepting a semiconductor substitution has little

to gain from an uncertain and risky development cycle. In fact, only a significant technological change, such as elimination of the transparent conductor or dramatically cheaper manufacturing technology, hold substantial promise for significant cost reductions.

The other primary conclusion one can draw is the importance of power conversion efficiency. At an end user system price of $\$7.5/W_P$ (margins included), a 1% absolute increase in efficiency translates to system level price decrease of $\$0.40\text{-}0.70/W_P$, far greater than the cost decrease of roughly $\$0.05/W_P$ gained from changing the semiconductor material. Thus, any technological alternative that sacrifices efficiency will be hard pressed to compete economically with CdTe solar cells.

Material	Cost ($/m^2)	Cost ($/$W_P$)	Comments
Glass/TCO	11	0.11	Superstrate version. Substrate glass would require metal coating
Modularization parts	6	0.06	Receptacle, plug, electrical connector, inserts, glass primer, metal tape
Panelization	5	0.05	Strut and bold (to connect to BOS structures)
Back glass or metal	5	0.05	For encapsulation
EVA	4	0.04	Either front of back pottant for encapsulation
Most expensive semi-conductor (Te, Ga, In, Ge)	3	0.03	Depends on form of feedstock pre-processed forms are more expensive
Shipping carton	2	0.02	Depends on quantities
Other active materials (semiconductors, metals)	2	0.02	Depends on form of feedstock pre-processed forms are more expensive
Waste processing	1	0.01	
Other process expendables	1.6	0.016	Hepafilters, chemicals, buff wheels, rubbing compound, detergent
Bypass diode	0.3	0.003	May not be required
Urethane (potting)	1	0.01	May not be required
Al target	0.3	0.003	Back contact
Miscellaneous	1.8	0.018	Numerous, inexpensive items
Total	44	0.44	

Table 1.1 Module component materials cost for thin film cadmium telluride systems.
These are direct costs; other indirect manufacturing costs are not included. To translate costs per area to cost per generated Watt, a power conversion efficiency of 10% is assumed.

1.4 Concentrator photovoltaics

Concentrators utilize optical systems to focus sunlight onto solar cells, allowing for a reduction in the cell area required for generating a given amount of power. Concentrated photovoltaics (CPV) can significantly reduce electricity cost by replacing expensive PV

converter area with a less expensive optical collector. CPV also provides the opportunity to use very high efficiency solar cells that would otherwise be prohibitively expensive. High efficiency solar cells typically utilize more exotic materials (gallium, indium, arsenic, germanium) in stacked (multijunction) geometries to extract more electrical power out of each spectral band of light.

These solar cells are expensive because of the methods used to manufacture them (metalorganic chemical vapor deposition) and their scarce material inputs. For instance, in 2007 Spectrolab set record efficiencies in a triple junction concentrator device grown on germanium.[13] However, germanium is scarce; if the entire US germanium reservoir[14] of 400,000 kg were depleted for the manufacturing of germanium wafers to amount to 200 MW_P.[15] Cells of this type are only commercially tenable under very high optical concentration, since the level of concentration dilutes their cost.

Large CPV systems exist only as pilot installations. However, some authors have estimated the total plant capital cost and levelized cost of electricity for mature technologies and large scale production. We reproduce the major costs from Swanson in Table 1.2.[16] These costs are significantly less than current system prices, but the relative costs between technologies are useful for comparison.

Medium plant — Albuquerque	GaAs dish	GaAs 2-axis	Si dish	2-axis static	Si 2-axis Fresnel	Thin film
Desert (Albuquerque) kWh/m^2/day	6·566	6·566	6·566	8·624	6·566	6·336
Diffuse (Boston) kWh/m^2/day	3·626	3·626	3·626	5·782	3·626	4·554
Albedo factor	1	1	1	1	1	1
BOS area (low) $/$m^2$	70	70	70	70	70	70
BOS area (high) $/$m^2$	140	140	140	140	140	140
BOS power (low) $/W	0·3	0·3	0·3	0·3	0·3	0·3
BOS power (high) $/W	0·6	0·6	0·6	0·6	0·6	0·6
Tracking (low) $/$m^2$	35	35	35	35	35	0
Tracking (high) $/$m^2$	67	67	67	67	67	0
Module (low) $/$m^2$	90	115	90	115	115	75
Module (high) $/$m^2$	160	230	160	230	230	150
Cell (low) $/$m^2$	30,000	30,000	15,000	300	15,000	0
Cell (high) $/$m^2$	100,000	100,000	20,000	1000	20,000	30
Cell efficiency (high)	0·3325	0·35	0·26	0·21	0·27	0·12
Cell efficiency (low)	0·285	0·3	0·23	0·17	0·24	0·08
Operating temperature	65	65	65	60	65	55
deta/dteta	2·20E-03	1·90E-03	2·20E-03	3·30E-03	2·20E-03	2·00E-03
Concentration	1000	1000	400	4	400	1
Module transmission	0·85	0·85	0·85	0·9	0·85	0·95
BOS eff.	0·85	0·85	0·85	0·9	0·85	0·9
Conc. premium	0	0	0	0	0	0
O&M cost (low) ¢/kWh	0·8	0·8	0·8	0·8	0·8	0·2
O&M cost (high) ¢/kWh	2·0	2·0	2·0	2·0	2·0	0·8
Cost-diff low ¢/kWh	12·8	13·2	15·8	13·7	16·6	13·2
Cost-diff high ¢/kWh	30·0	31·8	32·4	37·5	35·4	41·1
Cost-desert low ¢/kWh	7·4	7·7	9·1	9·4	9·5	9·6
Cost-desert high ¢/kWh	17·5	18·4	18·8	25·8	20·4	29·7
Cost-low $/W	1·59	1·64	1·99	2·71	2·10	2·16
Cost-high $/W	3·70	3·94	4·02	7·49	4·42	6·69

Table 1.2 Cost breakdown for a 100 kW_P-10 MW_P concentrator photovoltaics installation. Specific assumption in this analysis are listed in reference 16. Major assumptions include: high direct solar insolation (Albuquerque) and the availability of full time maintenance staff. GaAs and Si dish is a point focus parabolic dish system. GaAs and Si 2-axis are point focus Fresnel concentrators. Thin film assume costs that are approximately 50% lower than current production.

There are two major cost components that exist of CPV systems that are absent or significantly diminished compared to thin film PV: tracking and operations and maintenance (O&M) costs. To achieve high concentration, it is necessary to track the sun

throughout the day (see Section 3.1 for discussion). These mechanical systems are large and need to be maintained. In addition, high concentration systems must be actively cooled to dissipate additional thermal loading associated with higher photon fluxes and higher currents. O&M costs are four times higher for CPV versus thin film systems, and a tracking system can total up to 75% of the module cost. The values in Table 1.2 are estimates of the eventual system cost of economically relevant system, not of current prices. For instance, in a recent survey of two axis trackers in Photon International,[17] costs of a wide range of systems fell between \$200-300/m^2, substantially higher than \$35-67/m^2. These high accessory costs of CPV systems have frustrated wide scale deployment of CPV electricity generation.

1.5 Photosynthesis

This thesis began with a motivation for solar power referring to the photosynthesis precedent: it has powered the earth for billions of years at energy levels exceeding human energy consumption by an order of magnitude. Solar photovoltaics are, in essence, a type of artificial photosynthesis stopped short. Instead of proceeding directly to the production of organic matter, the intermediate products of electrons are harvested directly for human use. To motivate the novel architectures explored in Chapters 2 and 3 of this work, we continue with a brief summary of the events and structures of the primary reactions of photosynthesis.

Photosynthesis efficiently converts solar to electrical energy, which then drives a series of chemical reactions. This ubiquitous, time-tested energy transduction method is the source of all current biomass and fossil fuels relied upon today and sustains life on

Earth. Photosynthetic plants and bacteria utilize organic molecules similar to those used in organic PV to fix more than 100 Gtons of carbon annually, equivalent to 100 TW, a feat accomplished without high temperature processing or huge initial energetic expenditures. From a manufacturing standpoint, the utilization of photosynthetic organism represents the ultimate in low cost processing. A field of soybeans, for example, can be grown at very low cost but contains the equivalent of several times its area worth of PV cells.[‡] However, as with more mature silicon technologies, the cost of raw material may not be the main determinant of end energy cost.

The characteristic of photosynthesis that interests us most here is the architectural organization of components. In contrast to the conventional photovoltaics, the architecture of photosynthesis employs separate components for light absorption and charge generation, allowing these two functions to be optimized independently. Overall, photosynthesis can be divided into at least three distinct phases: (1) light absorption and energy transport by antenna systems, (2) energy collection and charge separation in reaction centers, and (3) stabilization by secondary reactions for use in the synthesis of sugars. The first two components are the biological equivalent of a PV cell, albeit with a

[‡] **Agricultural Production of Solar Cell Raw Materials.** Organic semiconductor PV utilizes materials most similar to photosynthesis, where the organic materials commonly consist of thin, amorphous films. I assume that photosynthetic pigment molecules, mainly chlorophyll, would take on this role in photosynthetic PV in an identical role. The total number of chlorophyll molecules can be calculated by assuming a molecular density in the thin film and a film thickness. The molecular density of bacteriochlorophyll c in the chlorosomes of green photosynthetic bacteria is 2×10^{21} cm^{-3}.[19] This is nearly identical to the molecular density of copper phthalocyanine molecules in thin films, justifying the validity of this assumption.[20] Assuming an active film thickness of 1 μm, 2×10^{17} chlorophyll molecules are needed per square cm of PV cells. To determine chlorophyll production rates, switchgrass (*Panacum virgatum L.*) was chosen as the model organism. Switchgrass grows quickly as is currently being investigated as a biofuel energy crop for co-firing fuel in coal plants and for cellulosic ethanol biofuel production.[18] The dry matter yield of switchgrass is assumed to be 15×10^6 g per hectare per year.[18] I then assume that 80% of this weight originates from grass leaves. The specific leaf weight (dry matter weight per surface area of exposed leaf) of switchgrass is roughly 40 g/m^2.[17] The number of chlorophyll molecules per unit of exposed leaf surface area is roughly 3×10^{16} per cm^2.[21]

These growth rates result in 3×10^5 m^2 of PV raw material per field (8 hectare) annually. Stated as the ratio of land necessary for production, agricultural methods could produce enough raw materials to make five times its area annually in solar cells.

very different architecture; see Figure 1.2. We continue with a brief description of these two components.

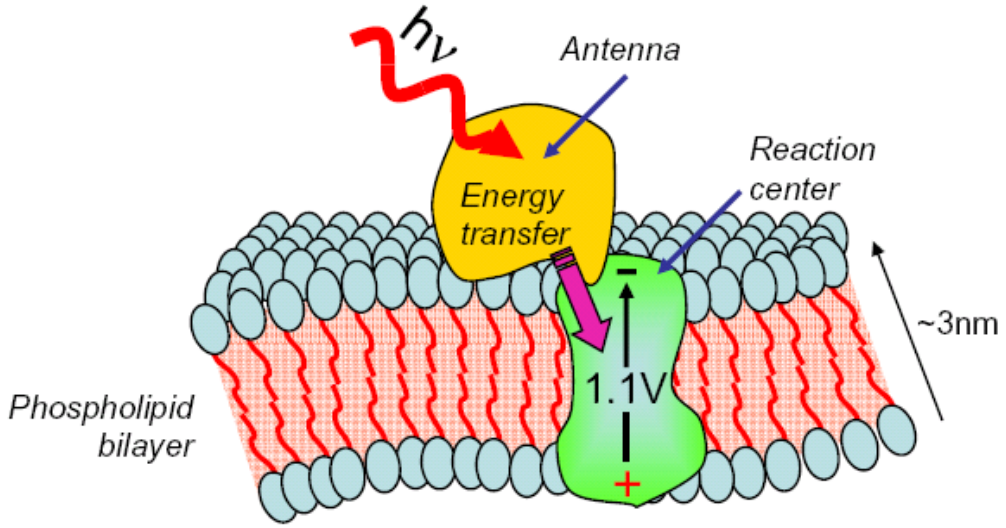

Figure 1.2 Molecular machinery of photosynthesis.
This simplified representation illustrates the spatial distribution of the light harvesting antenna and reaction center, the sites of photon absorption and exciton dissociation, respectively. The reaction center is remarkably preserved across all photosynthetic organisms, but there are diverse structural variations in the light harvesting antenna corresponding to the wide variation in light conditions in the many ecological niches these organisms occupy. After Purves, et al.[23]

1.5.1 Photosynthetic antenna complexes

All photosynthetic organisms contain light-gathering antenna systems; as such, they are remarkably diverse. Antenna types can be divided into several categories: (1) light harvesting complexes of purple bacteria, (2) light harvesting complexes of plants and algae, (3) phycobilisomes of cyanobacteria and red algae, (4) peridinin-chlorophyll proteins of dinoflagellate algae, and (5) chlorosomes of green bacteria.[24]

Antennas contain high concentrations of pigment molecules, including chlorophylls, bilins, carotenoids, and their derivatives. Photons captured by these pigments generate excitons, the products of absorbed light, that are energetically funneled the charge generation complexes. For example, phycobilisomes possess pigments at the periphery of the complex that absorb at higher energies than those at the core; these unique structures are discussed in Section 3.13. These excitons eventually reach the reaction center, where they can be changed into separate charges.

1.5.2 Photosynthetic reaction centers

In photosynthesis, the role of the *pn* interface is performed by the reaction center. The dissociation of excitonic energy states and formation of separated charges occurs at the reaction center via a series of electron transfer reactions. The reaction center is a membrane-bound, multi-subunit, pigment-protein complex which incorporates chlorophyll derivatives and other electron transfer cofactors such as quinones. The pigments and cofactors are held together by van der Waals interactions with the protein matrix; their positioning and orientations are important in facilitating electron transfer.

The ultimate collection point for excitons from neighboring antenna complexes is a chlorophyll dimer in the reaction center known as the special pair. This is the lowest energy site in the photosynthetic optical circuit. It is also the primary electron donor for the subsequent electron transfer cascade that carries the electron across the membrane while the hole remains at the special pair, thereby separating the exciton into isolated charges; see Figure 1.3. Recombination, or the back transfer of the electron to the special pair, is prevented by the electron transfer cascade which occurs in a series of very fast (1-

100 ps) electron transfer reactions, rapidly separating the charges to ~3 nm and strongly reducing the rate of recombination. Exciton dissociation in reaction centers thus proceeds with high efficiency; the quantum yield of products to photons is nearly unity.[25] The potential of the separated charges varies from approximately 0.5 V in primitive purple bacteria, to approximately 1.1 V in more advanced systems[26]. The secondary reactions that follow stabilize the oxidized and reduced species, yielding a chemical potential across the photosynthetic membrane that can then be used to drive cellular metabolism.

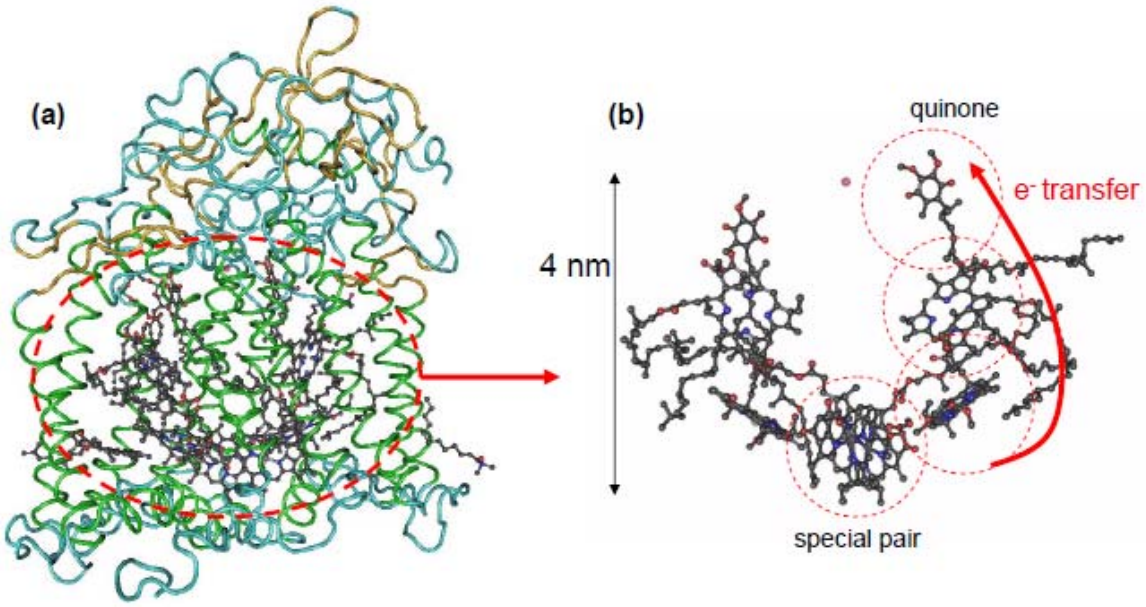

Figure 1.3 Structure of the reaction center complex of *Rhodobacter spaeroides*.
(A) Entire complex, including the L, M, and H cofactors. **(B)** Cofactors only. The special pair is the primary electron donor of the electron transfer cascade, illustrated by the arrow. Figure produced from the Protein Data Bank file 1AIJ using Visual Molecular Dynamics.[27]

Unlike antenna complexes, reaction center complexes are remarkably well preserved across plants and photosynthetic bacteria. All reaction centers follow the above described general structure of electron transfer cofactors embedded in a protein matrix. In plants and cyanobacteria, two special reaction centers called photosystems I and II operate in tandem to split water and create molecular oxygen, a highly energetic reaction since water is an extremely poor electron donor. Oxygen produced by photosynthesis is the source of oxygen in the atmosphere and fundamentally affected the development of life on Earth.

1.6 Conclusions

We can draw several major conclusions from the preceding sections.

1. Thin film inorganic solar cells can be made inexpensively, since the amount of expensive semiconductors has been reduced to a level where continued reduction provides little economic incentive. Reducing semiconductor cost is a futile aim.
2. Efficiency is vitally important in cost reduction. Any sacrifice in efficiency comes with high economic penalty.
3. Very high efficiencies are possible in concentrator systems, but the additional components that accompany high concentration make overall systems economically unattractive at present. Like thin films, the amount of expensive semiconductor is decreased, but the cost reductions of high concentration are attractive.

4. In photosynthesis, the processes of light absorption and charge generation are separated. The photosystem architecture allows independent optimization of light absorption and charge generation.

The two device architectures explored in this thesis address these conclusions. We apply the photosystem architecture to improve the efficiency of thin film organic PV cells and solar concentrators, using 1) antenna organic solar cells, and 2) organic solar concentrators, respectively.

1.7 Antenna organic solar cells

The high costs of solar electricity is due in part to the expensive equipment and energy hungry processes required in the manufacture of conventional semiconductor-based photovoltaic (PV) cells.[28] On the other hand, PV cells made from organic semiconductors such as films of molecules or polymers hold the promise of low cost production. Organic semiconductors can be deposited in thin film heterostructures to form solar cells that function similar to their conventional counterparts. Kim, et al have demonstrated tandem organic polymer solar cells with power conversion efficiencies of 6.4%,[29] and Xue, et al demonstrated tandem small molecule organic solar cells of 5.0%.[30] These laboratory record setting devices are far too low for commercial application. Even if they could be manufactured for free, their low efficiencies would still set a lower bound on the system cost because of non-module system costs.

There are several reasons why organic solar cell efficiency is low, but the work here is motivated by an inherent tradeoff made to maximize light absorption and free

charge creation. The inability of organic semiconductors to transport excitons, the bound pre-charge precursors, over long distances to a heterojunction interface for charge creation limits overall device thickness. Although organic materials can have very high absorption coefficients, the thickness limit set by the low exciton diffusion length is too low for complete light absorption. This design tradeoff limits performance and is called the exciton diffusion bottleneck.[31] See Section 2.2 for an in-depth discussion of this bottleneck.

While researchers have adopted several techniques to bypass this bottleneck, this thesis is concerned with a novel biomimetic method to spatially separate the functions of light absorption and charge generation into two different physical components (see Figure 1.4). Light energy is directly absorbed in an external 'antenna' layer adjacent to the metal film that forms the electrode of the solar cell. The light energy is then transferred across the metal electrode by guided energy transfer mediated by surface plasmon polaritons to an organic heterojunction, where charge separation and current collection occurs, completing the photovoltaic transduction.

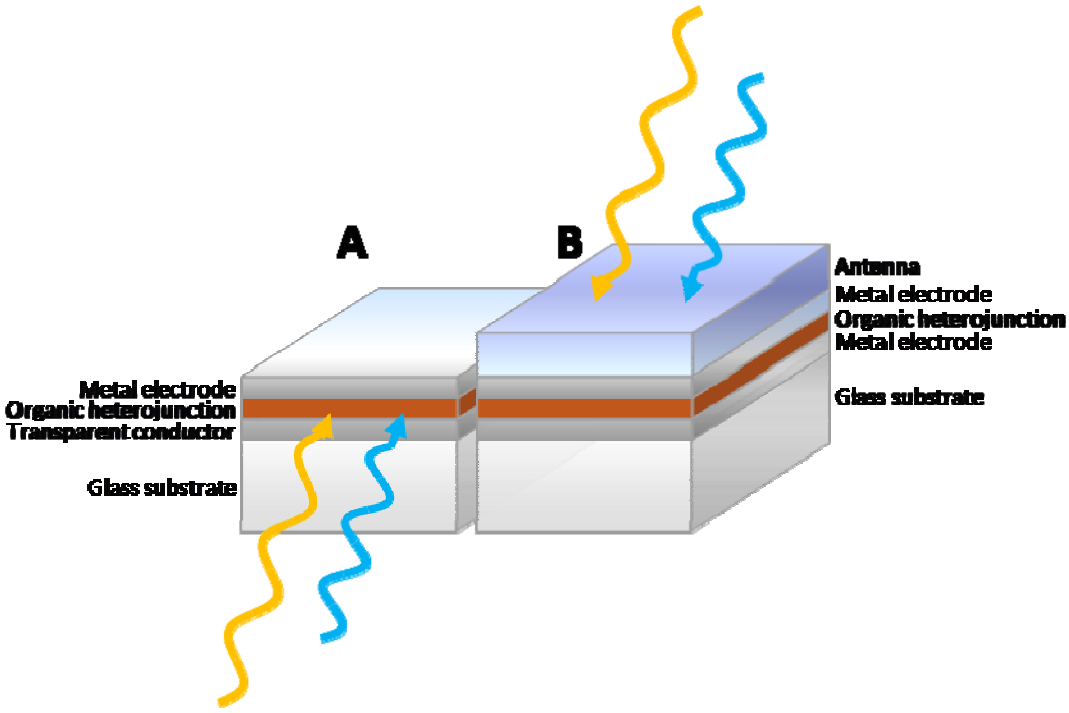

Figure 1.4 Structural comparison between conventional organic (A) and antenna organic PV (B).

The key structural differences of the proposed antenna organic PV configuration include the use of the glass as a substrate instead of superstrate and the absence of the expensive transparent conductive layer.

External energy transfer necessarily adds another step to photovoltaic conversion, but it uncouples the competing processes of light absorption and charge generation, similar to the spatial compartmentalization that occurs in photosynthesis. By separating these processes, each component can be optimized separately and the strict requirements of high optical and electrical performance can reside in materials well suited to perform each, as finding materials that can adequately perform both are difficult to design. By separating these functions, we desire to increase efficiencies such that the low cost manufacturing processes will enable very low cost, high efficiency organic solar cells. In

this thesis, this novel device architecture is investigated to assess its operational feasibility, and the efficiency of its sub-processes is quantified.

1.8 Organic solar concentrators

We also explore a second novel solar energy conversion device called the organic solar concentrator. Similar to antenna organic solar cells, we split the processes of light absorption and charge generation into two separate components. However, we now transfer energy between the two via waveguided photons. These photons can travel over longer distances than surface plasmon polaritons, so we can additionally configure the two components such that light is concentrated. That is, the size of the light collection element is much larger than the charge creation element. If the size difference is large enough, high efficiency solar cells can be used for the charge creation element (see Figure 1.5).

To efficiently concentrate light, we utilize thin films of organic chromophores as an ‘antenna’ to absorb and re-emit waveguided photons. These chromophores must be highly efficiency emitters and be transparent to their own radiation.

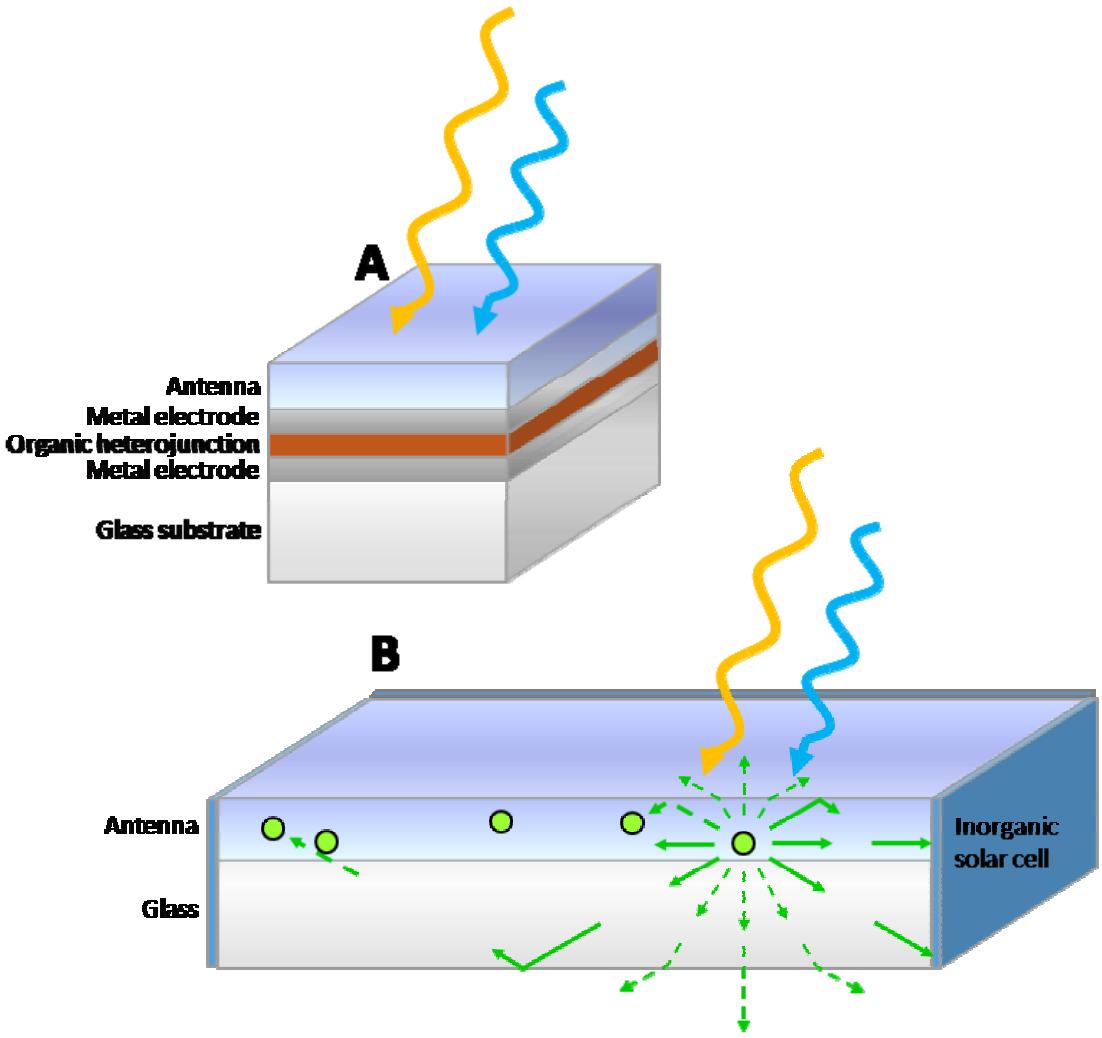

Figure 1.5 Structural comparison between antenna organic PV (A) and organic solar concentrators (B).

While the antenna layer in the organic solar concentrator is distributed over the whole collection face, the charge generation resides at the edges and covers far less area. As opposed to conventional fluorescent concentrators, organic solar concentrators utilize a thin, index matched chromophore film, enabling energy transfer from closely spaced emitters. Dashed lines represent light eventually lost and not available for conversion, including facial emission and self-absorption. Since there are no metals over the collection area, non-absorbed light can be transmitted through the whole structure.

This architecture is especially promising, as it can operate without tracking or cooling, two major costs in other concentrator systems. If the optical concentration can be made very high, we are able to utilize very high efficiency solar cells, as the concentration ratio effectively diminishes the amount of solar cells needed. We again utilize the biomimetic spatial compartmentalization approach to design high system efficiencies with high optical concentration ratios, which have the potential to result in total systems with low cost per Watt. In this thesis, this novel device architecture is investigated to assess its operational feasibility, and its overall efficiency is quantified.

1.9 Outline

In Chapter 2 of this thesis, we will explore the application of photosynthetic antenna architectures to organic PV. After an overview of organic materials characteristics (Section 2.1) and organic solar cell device physics (Section 2.2), we discuss the antenna architecture in detail and consider its benefits and drawbacks in Section 2.3. We continue in Section 2.5 with an overview of energy transfer mechanisms, including investigations of direct surface plasmon excitation of organic heterojunction bilayer devices.

To properly assess the technical feasibility of antenna organic solar cells, we would like to know the efficiency of the newly introduced process of antenna energy transfer. In Section 2.6, we consider the theoretical models of exciton coupling to guided modes in multilayer stacks, building off the framework laid by Chance, Prock, and Silbey.[32] We then seek to directly measure dipole transport efficiency across a thin silver layer that doubles as the organic superlattice photodetector cathode in Section 2.7.

After quantifying energy transfer, we integrate the processes in the design, fabrication, and measurement of antenna organic solar cells (Section 2.8). The dual requirements of strong absorption and photoluminescence efficiency are crucial to increased device performance; in Section 2.9, we describe ways in which absorption can be augmented by enclosing the antenna in a cavity resonator and describe initial demonstrations of performance. Finally, we speculate on efficiency limits as we conclude the topic in Section 2.10.

In Chapter 3, we consider energy transfer in organic solar concentrators. We review the characteristics of concentrator systems and discuss the features of active optical concentration. We discuss the constraints of tracking and cooling for both passive and active concentrators in Section 3.1 and Section 3.2, respectively. We explore the thermodynamic limits of optical concentration in Section 3.3. The stringent requirement of dye self-transparency has frustrated demonstrations of high efficiency systems in the past. In Section 3.4, we introduce methods to greatly reduce self-absorption and increase conversion efficiencies. After self absorption, the next biggest loss in well designed organic solar concentrators is from imperfect confinement of emitted light. In Section 3.5, we discuss this loss and suggest methods for reduction. Thermal limits on optical concentration for both passive systems and organic solar concentrators are discussed in Section 3.6. Chromophore stability is a crucial factor in understanding the practical utilization of fluorescent concentrators. Literature on the lifetime of the dyes utilized in this work when used in organic light emitting diodes is reviewed in Section 3.7. To improve performance, we apply the advances of organic optoelectronics to the organic solar concentrators. We review the physics of these advances in Sections 3.8.

In Sections 3.9 through 3.11, we describe several concentrators in multiple geometries and their discuss performance limiting processes. In Section 3.12, we adapt the analytical treatment of Batchelder and Zewail in understanding these devices as a function of optical concentration levels. In Section 3.14, we explore the theoretical and practical performance limits of each device configuration. We finish with a discussion on costs, which sets practical thresholds on how high the optical concentration must be.

We end in Chapter 4 with a summary and discussion of the prospects for organic materials in solar electricity generation.

Chapter 2 Antenna Organic Solar Cells

2.1 Organic materials

There is widespread interest in organic semiconducting materials for their potential for low cost, ease of processing, and compatibility with flexible substrates. Many of these materials are compatible with high throughput web processing. The printing, paint, and packaging industries routinely spray-coat, stamp, and evaporate molecular and polymeric materials onto flexible plastics and foils.[28] If similar web-based processing is realized for organic PV cells, organic devices need only reach performance levels commensurate to inorganic PV technologies to decrease the cost per Watt of PV power. In addition, large scale chemical synthesis capabilities exist to reform petrochemical products into an abundant raw material stream. Two classes of suitable molecular PV materials, the phthalocyanine[33] and perylene[34] pigments, are currently produced in quantities exceeding 80,000,000[35] kg and 1,500,000[34] kg annually.

These characteristics are ideal for a PV device, and as such, many researchers are actively pursuing a variety of devices with organic components.[31,36-39] The major classes of devices are dye sensitized solar cells,[40-45] organic/inorganic hybrid cells,[46-48] and

organic PV cells based on a heterojunction between polymeric[29] or small molecule molecular weight materials.[49]

This chapter is concerned with small molecular weight organic solar cells. The design of these cells needs is inherently different from inorganic cells,[36] due to the differences in physical properties and processes between organic and inorganic semiconductors. For example, light absorption in an organic material results in the creation of an exciton, or bound electron–hole pair, as opposed to the creation of free charges that typically result from absorption in inorganic solids. This is due to the weak, non-covalent, van der Waals interactions between molecules which hold the solid together which result in low intermolecular orbital overlap and low dielectric constants. In addition, organic semiconductors have low charge carrier mobilities (typically 10^{-5} – 10^{-1} cm^2/Vs) and short exciton diffusion lengths ($L_D \approx$ 4–50 nm). Many organic materials have high absorption coefficients ($\alpha > 10^5$ cm^{-1}), so layer thicknesses can be kept thin to reduce materials utilization.

2.2 Organic solar cells

We begin by briefly reviewing the processes and structures commonly used in organic semiconductor heterostructure PV. For an in depth review of these devices, see Peumans, 2003.[49] Similar to their inorganic counterparts, organic PV devices are comprised of donor and acceptor semiconducting regions sandwiched between conducting electrodes. Usually, these materials are different semiconductors, as reliable doping to control majority carrier type is difficult to achieve.

The sequence of processes yielding light to electrical energy transduction in organic PV can be divided into four phases, as summarized in Figure 2.1. In the first, upon optical excitation in one or both organic materials, localized Frenkel or charge transfer excitons are generated.[50,51] These tightly-bound, charge-neutral species diffuse until they recombine or dissociate. Excitons that reach an interface between the donor and acceptor layers will dissociate if the energetic offsets favor the process. For large offsets, dissociation occurs over time scales of a few hundred femtoseconds[52] and results in free electrons in the lowest unoccupied molecular orbital of the electron transport material and free holes in the highest occupied molecular orbital of the hole transport material. These free carriers diffuse out towards the contact and are available to perform electrical work.

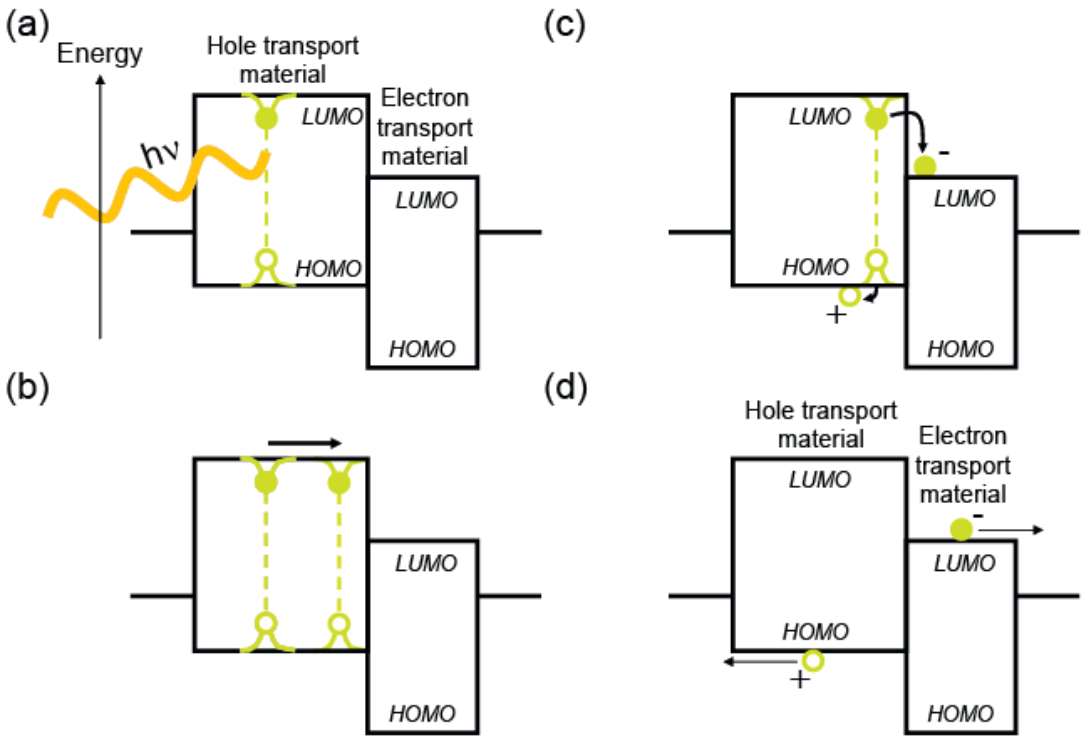

Figure 2.1 Summary of processes in organic PV leading to energy conversion.
(A) Optical absorption in one or more active semiconducting layers creates an exciton, an electron-hole pair localized on a single molecule. **(B)** Excitons diffuse in the thickness of the film. **(C)** Those that reach the interface between the donor and acceptor layers can dissociate. In this example, an excited molecule in the donor hole transport material reduces an nearby acceptor molecule in the adjacent electron transport material. **(D)** The separated free electrons and holes diffuse out towards the metal electrodes, completing the energy transduction process.

The useful thickness of an organic PV cell is restricted to the distance that excitons can travel before recombining, typically on the order of 10 nm.[49] Within this region the internal quantum efficiency (the ratio of charge extracted to absorbed photons) can be 100%. But the quantum efficiency drops dramatically in thicker devices due to exciton recombination losses.[31] Thus, despite optical absorption coefficients exceeding 10^5 cm^{-1} averaged over the visible spectrum, organic PV is limited by an inability to

absorb enough light. Several classes of solar cells have emerged whose device architectures address this concern, including dye-sensitized nanostructured oxide cells,[44] bulk organic heterojunction cells,[53,54] and organic-inorganic hybrid composites.[47,55,56] These approaches share the characteristic of increased surface area of the exciton dissociation interface, increasing the useful thickness of the cell by decreasing the distance between exciton generation and dissociation. However, the necessity for continuous pathways within the two phases can hinder charge collection and limit performance[57].

2.3 The antenna architecture

The low cost production potential of organic solar cells is promising, but low power conversion efficiencies have limited the practical application of organic technology, in part due to the exciton diffusion bottleneck. A unique approach that addresses this bottleneck exists in photosynthetic bacteria and plants, another much older and more sophisticated, example of organic electronics. In photosynthesis, light absorption and photochemical electron transfer occur in spatially distinct molecular components referred to as light harvesting antenna complexes and reaction centers[25]. In contrast, absorption, exciton dissociation and charge extraction all occur in the organic semiconductors that comprise the active donor and acceptor layers in organic PV. This characteristic frustrates materials selection for organic PV, as the organic semiconductors must simultaneously satisfy several constraints: (1) strong broadband optical absorption with an extinction coefficient of at least 10^5 cm^{-1} across the visible spectrum, (2) efficient long range exciton transport, (3) optimal energy level alignment for rapid exciton dissociation

efficiency, and (4) high electron and hole mobilities and continuous charge pathways to the two electrodes to minimize recombination losses.

Akin to photosynthesis, organic PV may benefit from separating the functions of light absorption and exciton dissociation into two spatially distinct structures, allowing individual optimization of each. We demonstrate separation of optical and electrical functions by utilizing guided wave mediated energy transfer across thin metal films. In such a device, energy transduction proceeds by photon absorption in an 'artificial antenna'. Excited molecular dipoles in the antenna either radiate into waveguide modes or non-radiatively couple to surface plasmon polariton (SPP) modes in the multilayer structure. By externalizing light absorption in a thick antenna, the reaction center component of the device can be sufficiently thin to yield devices with near unity internal quantum efficiencies[58].

A major advantage of coupling into guided modes is that these modes are absorbed even in very thin organic PV cells, optimized for maximum internal quantum efficiency. Guided modes propagate in the plane of the device, parallel to the charge generation interface. The dimensions of the cell in this plane are on the order of 10^{-2} m, rather than ~10^{-7} m perpendicular to the interface. The maximum distance of interaction between a reaction center and a guided mode is thus the distance that these modes travel at visible frequencies. For both SPPs and waveguide modes, they can be several orders of magnitude greater than the thickness of the reaction center, increasing the likelihood they will be absorbed; see Figure 2.2. Energy which propagates in these guided modes is absorbed in the 'artificial reaction center' of the PV, after which the processes of exciton diffusion, dissociation, and charge collection occur as before.

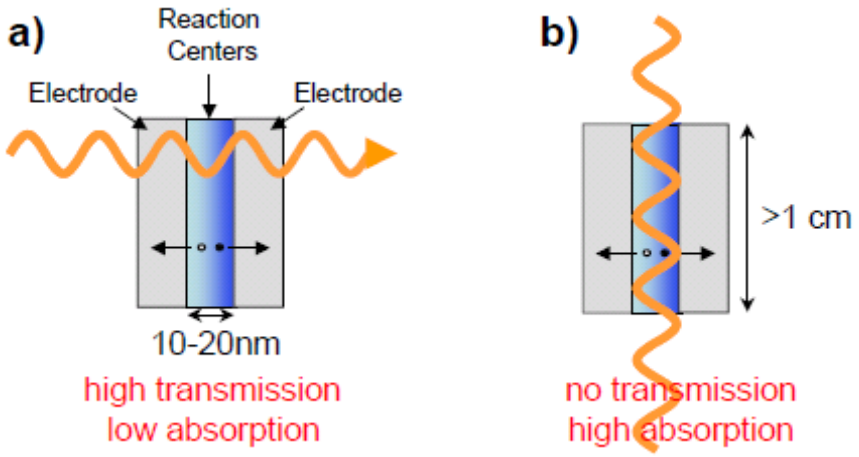

Figure 2.2 PV device excitation routes.

Excitation of solar cells under normal (perpendicular) **(A)** and parallel surface mode excitation **(B)**. The interaction distance of the electromagnetic fields and the absorbing artificial reaction center ratio between the two is several orders of magnitude. For very thin PV, high absorption and no transmission is preferred.

There are several advantages to the biomimetic approach of separating light absorption and exciton dissociation in organic PV:

1. By decoupling the optical and electrical components of the solar cell, the artificial reaction center can be made thinner than the exciton diffusion length, ensuring that all excitons are generated close to the location of exciton dissociation. The efficiency of this process should approach unity, resulting in internal quantum efficiencies approaching unity as well, as the efficiency of charge transfer and charge collection is known to be highly efficient.[54,59]
2. Molecular excitonic states exhibit highly structured absorption spectra. Thus, to increase the photocurrent in organic PV, one must choose a combination of active

materials that absorb evenly across the visible spectrum. In contrast, separating the optical and electrical functions allows the reaction center to be optimized at a single peak wavelength corresponding to the emission of the antenna.

3. Since the light absorbing antenna layer no longer needs to transport charge, new classes of solar cell materials can be used. The ideal antenna layer should be highly absorptive and have a high efficiency for photoluminescence (PL) such that reemission is strong. Candidate materials include those which absorb strongly like J-aggregates, nanometallic particles, quantum dots, and photosynthetic complexes that possess high quantum photoluminescent efficiency such as phycobilisomes from cyanobacteria and red algae. While quantum dots and nanometallic particles have been embedded as active layer of solar cells previously to increase absorption,[60,61] their poor charge transport characteristics have decreased overall device performance.
4. The energetic funneling that biological antennas like cholorosomes employ can be utilized in mixed antenna layers. In mixed layers, light can be absorbed in a host material and energy is funneled to a less absorptive, highly luminescent material for reemission into the bound modes.

To properly assess the technical feasibility of antenna organic solar cells, we would like to know the efficiency of the newly introduced process of antenna energy transfer. Photocurrent that originates from the antenna will result from the sequential completion of three processes:

$$\Delta\eta_{EQE} = \eta_{ABS}^{Antenna} \cdot \eta_{ET} \cdot \eta_{IQE} \quad (1)$$

where $\eta_{ABS}^{Antenna}$ is the absorption efficiency of the antenna layer, η_{ET} is the energy transfer efficiency across the silver electrode and is dependent on the photoluminescence efficiency of the antenna molecules, and η_{IQE} is the internal quantum efficiency of the artificial reaction center. Quantification of η_{ET} involves 1) assessing the efficiency of antenna excitation of guided modes and 2) assessing the efficiency of guided mode excitation of the modified organic solar cell.

To quantify η_{ET}, we may first start with a simpler system with the antenna removed, as in Figure 1.4a. By directly illuminating the structure with SPPs, we can attribute all current to having originated from the plasmon excitation. After the plasmon excitation efficiency (step 2) has been assessed, we can theoretically investigate the efficiency of antenna excitation of guided modes (step 1). Together, these should allow us to conclude if the overall architecture is technically feasible.

Before exploring the SPP excitation efficiency, we proceed with a discussion of the physics of SPPs.

2.4 Surface plasmon polaritons physics

Surface plasmon polaritons (SPPs) are a unique class of waves associated with interfaces between metals and dielectrics. They are comprised of a coupled oscillation of an electromagnetic field and surface charges at a metal-dielectric interface. SPPs propagate along the interface with electromagnetic fields, energy, and charges highly localized within the interface area. Their properties depend strongly on characteristics of both the metal (complex dielectric function, corrugations, roughness) and the dielectric (refractive

index). In the absence of the adjacent artificial reaction center, SPPs are internally damped by joule heating in the metal film. Recent advancements in the ability to control the structure of metals on the nanometer scale have spurred great interest in SPPs in the last decade. Their unique properties are of wide interest in many fields and are being explored for their potential in optics, magneto-optic data storage, microscopy, and sensors.

The existence of SPPs can be straightforwardly derived from Maxwell's equations and the application of appropriate boundary conditions. They are transverse magnetic in character and the existence of surface charge requires an electric field normal to the surface. Since these surface waves propagate along the interface, there is also an electric field in the propagation direction; see Figure 2.3. The high density of charges at the interfaces leads to a field enhancement at the interface which decays exponentially into the space normal to the surface. This field is referred to as evanescent, reflecting the bound, non-radiative nature of SPPs which restricts power from propagating away from the interface; see Figure 2.4. The field lines associated with SPPs are transverse magnetic and both transverse and longitudinal in electric describing the fluctuations in surface charge density, where the decay length into the metal is the classical skin depth.

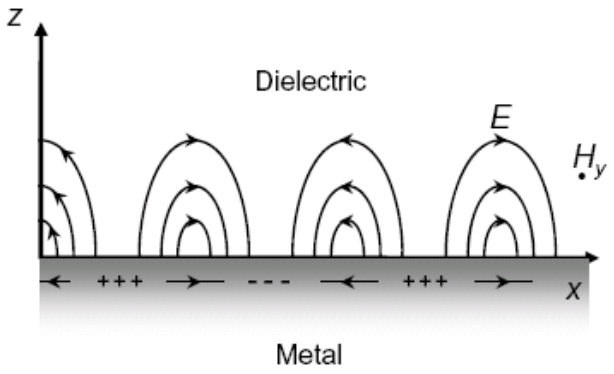

Figure 2.3 Surface plasmon polariton field orientations.

SPPs exhibit magnetic fields that are transverse in character, and the generation of surface charge requires an electric field normal to the surface (after Barnes, et al.[62]).

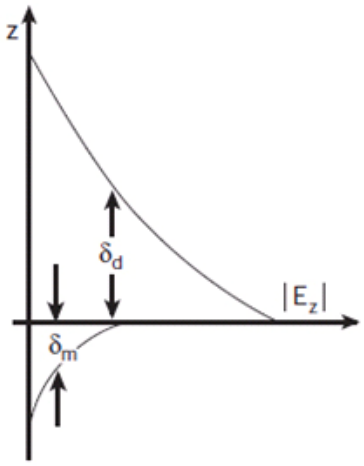

Figure 2.4 Surface plasmon polariton field magnitudes.

SPPs are evanescent waves localized at the interface between a noble metal and a dielectric. The electric field drops sharply in the metal layer with the classical skin depth. In a device structure, spatial overlap between the electric field and absorptive materials are an avenue for energy transfer. Figure from Barnes, et al.[62]

The electromagnetic field of the SPPs excite electron-hole pairs at the Fermi level of the silver; the following de-excitation produces phonons and thus heating. The propagation length of SPPs on a metal-dielectric interface is given by:[63]

$$\delta_{SPP} = \frac{c}{\omega}\left(\frac{\varepsilon_m^{'} + \varepsilon_d}{\varepsilon_m^{'}\varepsilon_d}\right)^{3/2} \frac{\left(\varepsilon_m^{'}\right)^2}{\varepsilon_m^{''}}. \qquad (2)$$

For visible wavelengths, the internal damping of SPPs is least for the noble metals and minimum for silver; δ_{SPP}^{Ag} at 530 nm is approximately 30 μm; see Figure 2.5.

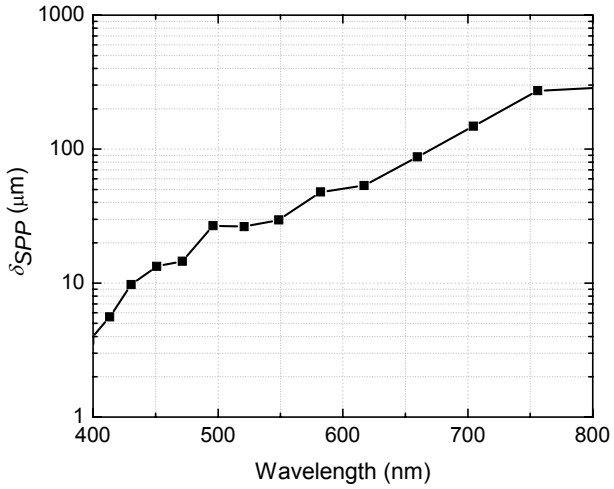

Figure 2.5 SPP propagation lengths on silver thin films.
At visible wavelengths, silver exhibits lowest losses when localized at an air interface. These lengths are calculated using the optical constants from Johnson and Christy.[64]

The frequency ω of SPP longitudinal oscillations is tied to its in-plane wave vector magnitude k_x by a dispersion relation $\omega(k_x)$, described by

$$\omega_{SPP} = c \cdot k_x \left(\frac{\varepsilon_m^{'} \varepsilon_d}{\varepsilon_m^{'} + \varepsilon_d} \right)^{-1/2} \tag{3}$$

where ε_d and ε_m are the permittivities in the dielectric and metal, respectively. This relation is plotted in Figure 2.6, which illustrates the polaritonic nature SPPs. At low frequencies, the SPP dispersion approaches that of photons that reside in the dielectric, characterized by the light line:

$$\omega_{photon} = \frac{c \cdot k_{photon}}{n_d} . \tag{4}$$

At these low frequencies, the SPP has the character of an evanescent photon and surface charge oscillations are weak. At very high frequencies, the SPP has the character of a plasma oscillation in a free electron gas, which is independent of wave vector:

$$\omega_{SPP} = \left(\frac{\omega_P^{\,2}}{1 + \varepsilon_d} \right)^{1/2} \tag{5}$$

where ω_P is the plasma frequency.

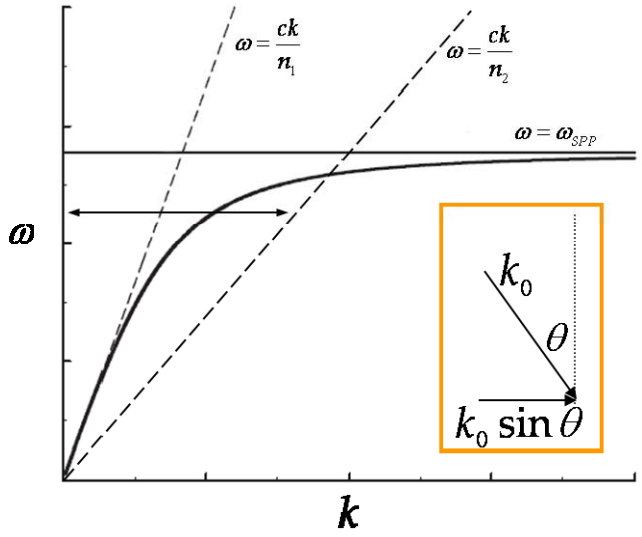

Figure 2.6 SPP dispersion relation.

The polaritonic nature of SPPs gives them the hybrid characteristics between photons and bulk plasmons. For smooth interfaces, neither photons nor plasmons can couple to SPPs, as the dual conservation requirements of energy and momentum cannot be satisfied. However, photons in a higher index medium (n_2) exhibit dispersion that allows scattering. k represents wavevector magnitude. The conservation of in-plane momentum ($k_0 \sin\theta$) must be conserved for coupling to occur. This value can be adjusted by altering the angle of incidence, θ.

The dispersion relation of SPPs intersects neither the photon or plasmon dispersions. At low frequencies, additional momentum associated with the oscillating electrons in an SPP which moves its dispersion to the right of photons. At high frequencies, the magnitude of electron oscillations in an SPP is always less than that of a pure plasma wave. To scatter between SPPs and either photons or plasmons, the dual conservation conditions for energy and in plane momentum must be satisfied. In the absence of other interactions, it is impossible to scatter from SPP to either photon or plasmon, and vice versa.

This characteristic necessitates the use of a special experimental configuration to excite SPPs, the Krestchmann geometry,[65] where the metal layer is a thin film adjacent to a second dielectric media with a index of refraction higher than the first; see Figure 2.7. Light incident from the second dielectric may interact with the first dielectric under the condition of total internal reflection, where an evanescent photon permeates the multilayered structure. As the angle of incidence of the incident light is varied, a resonance condition occurs where the dual conservation conditions are fulfilled and an SPP will propagate at the interface with the lower index medium, the only interface that can support SPP modes.

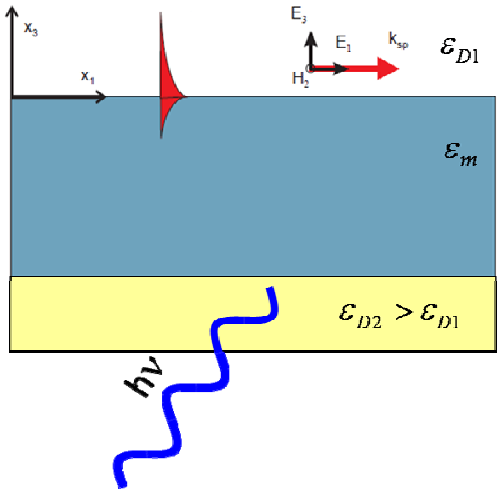

Figure 2.7 Kretschmann experimental configuration.
In this geometry, light is incident through medium 2, whose refractive index is greater than medium 1, which can support the propagation of SPPs. The evanescent wave permeates through the thin metal layers when the angle of incidence is greater than the angle of total internal reflection, allowing scattering with SPPs.

2.5 Organic solar cell SPP excitation efficiency

The direct sensing of surface plasmon resonance via the transduction of the surface wave electric field enhancement in solar cells is a direct demonstration of the utility of SPP in the excitation of photovoltaic devices.

In addition to characterizing organic solar cells, surface plasmon resonances (SPRs) are commonly used in the real-time detection of chemical and biomolecular interactions at metal interfaces.[66] The main SPR detection methods are based on either the direct measurement of the amplitude or momentum of the reflected optical wave near resonance. Both techniques interrogate the reflected wave using an external photodiode element or array. This section describes an integrated SPR detector using an organic photodetector whose upper electrode composes the active sensing element. Integration offers the benefits of miniaturization, and may have other wide commercial applications, including industrial process control, environmental testing, point of care diagnostics, and food safety.

Photocurrent enhancements in organic Schottky photodiodes under surface plasmon polariton (SPP) excitation have been previously demonstrated,[67,68] but typical external quantum efficiencies peaked at 0.05%.[68] We can detect the resonant change in total absorption within a thin film organic double heterojunction photovoltaic cell, illuminated with λ = 532 nm excitation in the Kretschmann geometry under attenuated total reflection. Light incident on the structure from the optically dense glass prism can excite SPPs at the silver cathode-air interface on the opposite side of the stack.

To measure the efficiency of SPP excitation, thin film double heterostructure organic photodiodes were fabricated on cleaned glass substrates. Commercially available

organic layers were purified by thermal gradient sublimation. Films were deposited at room temperature at high vacuum (~10^{-6} Torr) in the following order: 235Å silver, 190Å of the donor-like copper phthalocyanine (CuPC) and 200Å of the acceptor-like fullerene (C_{60}). Next, a 85Å thick layer of bathocuproine (BCP) was grown; BCP has been previously shown to function as an exciton blocking, electron transport layer solar cells.[69] This layer was followed by a 285Å thick layer of silver shadow-masked to define cathodes of area 1.4 x 10^{-2} cm^2.

Light was coupled to the diode via a hemicylindrical prism attached to the glass substrate with index matching fluid; see Figure 2.8. The prism and photodiode were mounted on a computer controlled rotating stage and illuminated with p-polarized light of wavelength λ = 532 nm with an incident power intensity of 50 μW. The intensity of the reflected beam is monitored with a Si photodetector. The measured photocurrent in air at zero bias is measured with a Keithley sourcemeter. Spectral external quantum efficiency measurements were made by using a xenon lamp with monochromator, chopped at ~90 Hz and measured with a lock-in amplifier. Light intensity was measured with a calibrated silicon photodiode. The indices of refraction and extinction coefficients of all modeled thin films were derived from measurements using an Aquila reflection-transmission thin film spectrophotometer. Because Ag penetrates the thin BCP layer during deposition,[70,71] the optical constants of the cathode were obtained from a BCP/Ag bilayer.

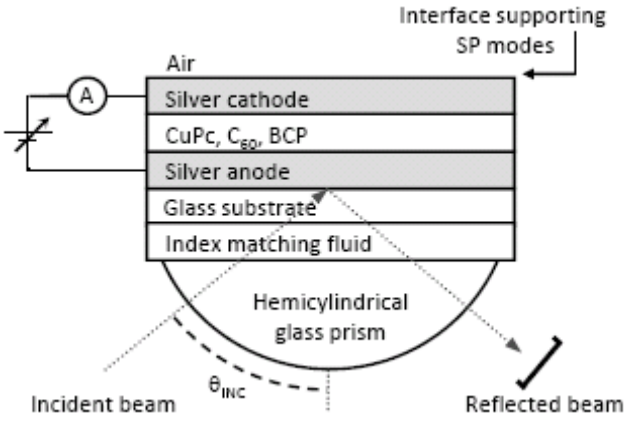

Figure 2.8 Kretschmann experimental configuration.

Monochromatic p-polarized laser light of wavelength 532 nm is incident on a prism coupled to the glass substrate through index matching fluid. The prism acts to retain a normal incidence coupling from air to glass. As θ_i increases the onset of total internal reflection precedes an immediate dip in reflected light intensity and increase in monitored photocurrent at SPP resonance. The only interface that can support SPPs in this geometry is at the Ag cathode-air interface. The device structure investigated was glass / Ag (235Å) / CuPC (190Å) / C_{60} (200Å) / BCP (75Å) / Ag (285Å).

We employ a plane wave matrix formulism to calculate the magnitude of the electric fields throughout the thickness of the device.[72] The electric field in any layer *j*, is given for TM polarization by:

$$E_j = \left(A_{1j}e^{-ik_{z,j}z}\left(1,0,k_x/k_{z,j}\right) + A_{2j}e^{ik_{z,j}z}\left(1,0,-k_x/k_{z,j}\right)\right)e^{i(k_x x-\omega t)} \qquad (6)$$

where k_x is the wavevector in the plane of the interfaces of the structure, calculated from the incident beam. Imposition of boundary conditions at each interface leads to a set of equations for the coefficients A_j that are solved using simple matrix methods. The magnetic fields in the structure can be calculated using the usual relation for

electromagnetic waves. This enables the calculation of the Poynting vector in each layer of the structure.

On the right side of the Figure 2.9a (negative distance from the prism-air interface), reflective interference controls the shape of the field magnitude. At surface plasmon resonance, the reflected field drops and a localized enhancement on the opposite side of the device is evident, and, more importantly, the field inside the organic heterostructure dramatically increases, coinciding with increased optical absorption.

The modeled total electric field intensity throughout the thickness dimension is shown in Figure 2.9b for θ_i at 30^o and 47^o. The field enhancement at the Ag-air interface is consistent with the SP propagation and is the only possible mode excitable through the prism coupled Kretschmann geometry. For incident radiation with $\lambda = 532$ nm, absorption is primarily in the CuPc layer. Total absorption is calculable by integrating the divergence of the Poynting vector $\vec{S}$ across the thickness of interest. At SPR, over 80% of absorbed light is absorbed in the CuPc layer. However, the CuPc layer is 400Å from the Ag-air interface. A stronger field enhancement is possible with decreasing distance from the SP supporting interface and will result in greater absorption.

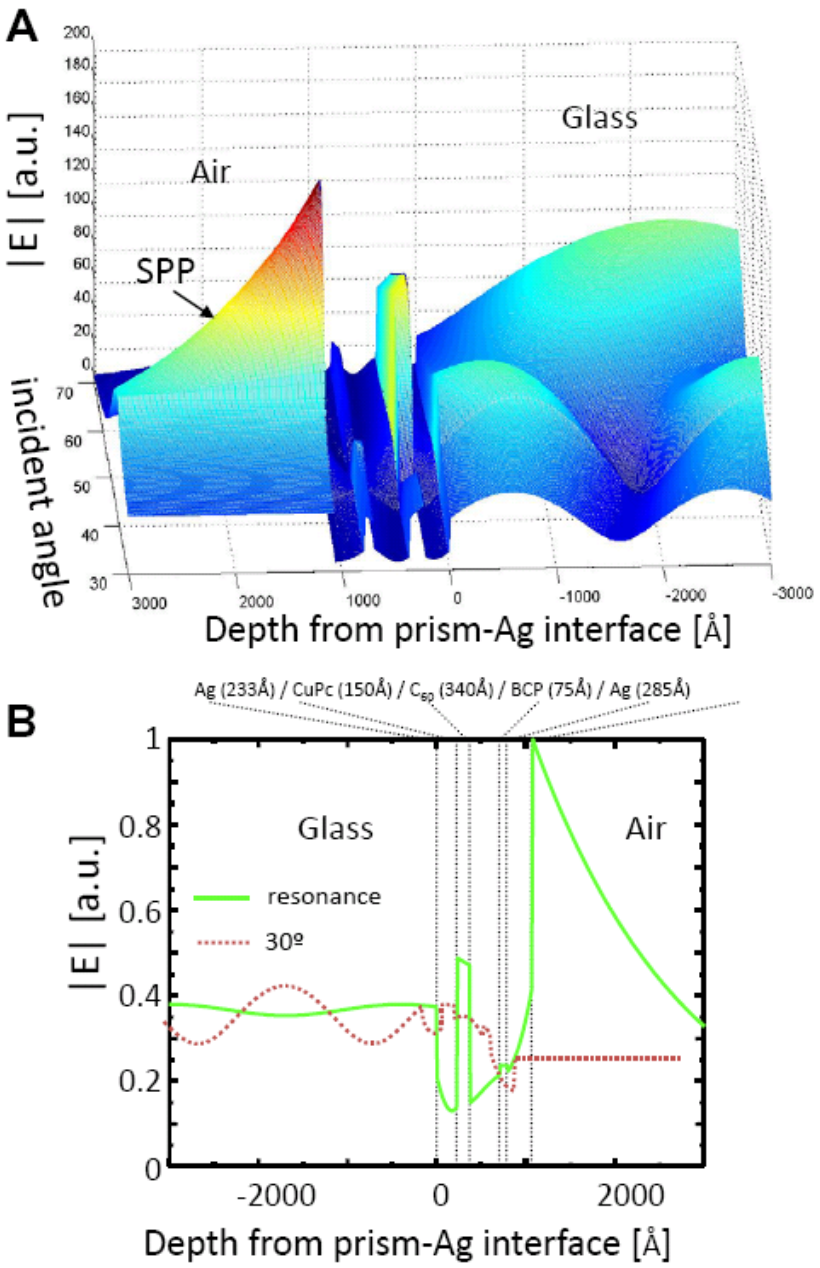

Figure 2.9 Magnitude of the electric field in surface plasmon excited photodiode

A pronounced enhancement at the silver-air interface indicates plasmon resonance. In **(B)**, the field lines at SPP resonance are compared to 30^{o} incidence. At resonance, the fields in the absorbing artificial reaction center (CuPC and C_{60}) are also enhanced, leading to an increase in external quantum efficiency.

In Figure 2.10a, we plot the measured reflected light intensity (reflectivity, R) versus incident illumination angle, θ_i, for p-polarized incident light. The mixed transversal and longitudinal electromagnetic field carried by SPPs can only be excited by p-polarized light and as such, only the p-polarized reflectivity exhibits a sudden decrease corresponding to SPP excitation at the condition of momentum conservation.[63] As θ_i increases, two features are observed: the increase at 44°, which corresponds to the onset of total internal reflection; and a decrease at 52º, which corresponds to destructive interference of backscattered light back into the glass hemicylinder given evanescent excitation of a SPP at the Ag cathode-air interface. This back scattered light is 180° out of phase with the incident light; at resonance this backscattered light can destructively interfere with the incoming wave resulting in the sharp drop in reflectivity observed SPR.

Besides the back-radiation damping of SPs at the Ag-air interface, the surface wave vector of the SPP can linearly combine with the vectors which compose the Fourier spectrum of the rough surface. These scattering events allow the non-radiative SPPs to forward scatter photons in the dielectric (air) at the interface of field enhancement. The correlation between surface roughness and directional light emission has been measured by several authors[73-75]. According to Tajima et al, the efficiency of light emission from films of 15Å rms roughness is about 10%. This value is adequately describes the deviation from the measured and modeled reflectivity for $\theta_i > \theta_{SPR}$.

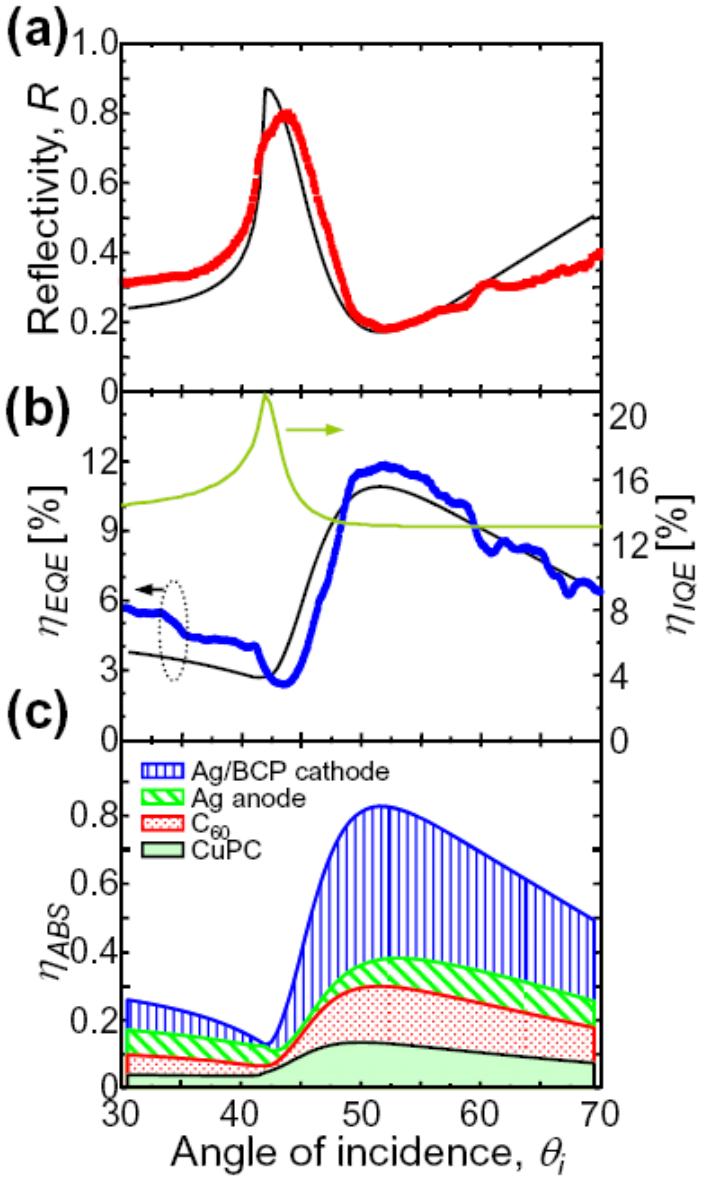

Figure 2.10 Direct SPP excitation optical spectra

(A) The measured (■) and modeled (solid line) reflectivity spectra sharply increase at $\theta_i = 40^\circ$ corresponding to the onset of total internal reflection from the stack. As θ_i increases the reflectivity sharply drops, reaching a minimum at surface plasmon resonance when $\theta_i = 52^\circ$. **(B)** The angular positions of maximum and minimum reflectivity align with the measured (●) and modeled (solid line) minimum and maximum external quantum efficiencies. At resonance, $\eta_{EQE} = 12\%$, reaching twice the efficiency of off resonance excitation at $\theta_i = 30^\circ$. The modeled internal quantum efficiency decreases slightly under plasmon illumination from 14% to 13%. **(C)** Modeled optical absorption in all device layers increases by a factor of three at resonance.

In Figure 2.10b, the external quantum efficiency, η_{EQE}, is plotted versus θ_i. The resonance dip in reflectivity correlates to a peak in quantum efficiency of 12%, double that at plane wave illumination. Disparities between η_{EQE} and η_{ABS} as a function of θ_i is attributable to two phenomena associated with SPP propagation on metal surfaces. First, as the angle of incidence is increased, more light energy is guided into SPP modes. At plasmon resonance, energy dissipation reaches a maximum, resulting in a decrease in internal QE. Second, light emission associated with propagating SPPs results in the outcoupling of useful energy. Both phenomena compete with light absorption in the artificial reaction center and constitute loss.

In Figure 2.10c, we plot the modeled absorption in each layer of the detector. To estimate the optical absorption within each layer of the SPP detector, we employ the plane wave matrix formulism to calculate the magnitude of the electromagnetic fields throughout the thickness of the device.[72] At low angles of incidence, $\theta_i < \theta_{SPR}$, photocurrent is primarily limited by low light absorption. For instance, at $\theta_i = 30^\circ$, the absorption within the active organic layers, CuPC and C_{60}, $\eta_{ABS}^{Org} = 10\%$. At SPR, absorption in the complete stack, η_{ABS}^{Total}, increases by more than a factor of three to 83%, and the absorption within the active layers is $\eta_{ABS}^{Org} = 30\%$. The increase in η_{ABS}^{Org} by a factor of three at SPR mirrors the factor of three increase in η_{EQE}, confirming that SPP detection is mediated by an increase in absorption. The ratio $\eta_{ABS}^{Org} / \eta_{ABS}^{Total}$ decreases by 2% in resonance, indicating that there is a negligible increase in the fraction of energy lost to joule heating and roughness induced scattering under SPP excitation.

To confirm the modeling results, η_{EQE} of this device is plotted in Figure 2.11 as a function of wavelength at normal incidence. Below λ = 525 nm, photocurrent is primarily generated in the C_{60} layer, while the CuPC layer primarily absorbs above λ = 525 nm. At λ = 532 nm, the extinction coefficients of C_{60} and CuPC are approximately equal at k = 0.10 and 0.08, respectively, as modeled from the reflectivity-transmission spectra; for derived n and k, see Figure 2.12.

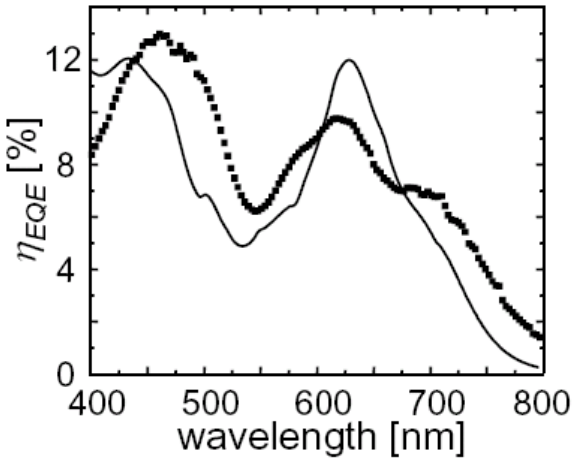

Figure 2.11 External quantum efficiency spectra

The measured (■) and modeled (line) external quantum efficiency versus wavelength for this device. The angular dependent quantum efficiency was interrogated at $\lambda = 532$ nm, where light absorption occurs nearly equally in CuPC and C_{60}.

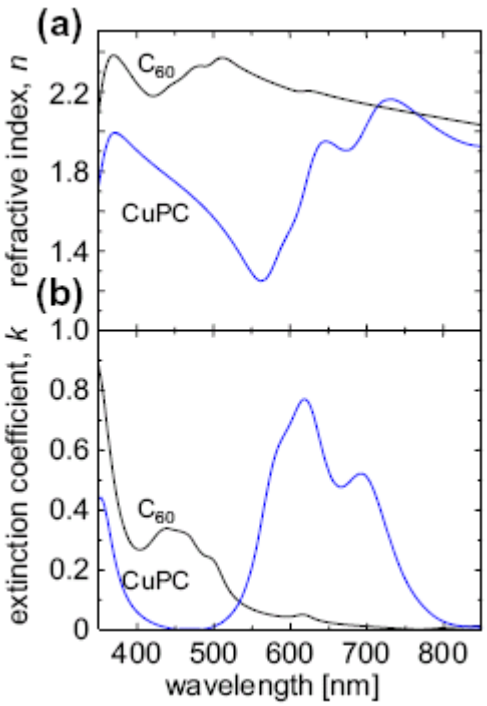

Figure 2.12 Optical constancies of C_{60} and CuPC.

The refractive indices **(A)** and extinction coefficients **(B)** for the CuPC and C_{60} were used in device modeling. The values were modeled from thin film reflectance-transmittance spetrophotometry.

To model the photocurrent spectrum of Figure 2.11, we fit the exciton diffusion lengths by $L_D^{CuPc} = 70$ Å and $L_D^{C_{60}} = 100$ Å, similar to previously reported values of 100 ± 30 Å for CuPC,[49] and 141 Å for C_{60}.[76] The fit is confirmed by comparison of the measured and modeled $R(\theta)$ and $\eta_{EQE}(\theta)$ spectra, as plotted in Figure 2.10a and Figure 2.10b. The modeling accurately predicts the angular location and intensity of SPR for both $R(\theta)$ and $\eta_{EQE}(\theta)$ to within 0.5° and 1%, respectively.

We modeled the BCP/Ag cathode bilayer as a single homogenous film. Seumori et al previously observed deep penetration of evaporation metal on amorphous organic films[70] and Rand et al examined solar cells where silver penetration into very thin BCP

yielded trap states and lowered the barrier to electron extraction.[71] These observations suggest that the BCP cannot be optically modeled as a uniform film; consistent with our findings. We evaporated a bilayer film of BCP and Ag with thicknesses identical to those in the solar cell and measured its absorption spectrum to derive its optical characteristics. The silver penetration into the BCP layer results in a film bilayer that is more absorptive (see Figure 2.13), independent of whether excitation is via SPPs or photons, suggesting that the reduction of metal penetration by alternative electrode deposition methods may increase the internal quantum efficiency in organic PV.

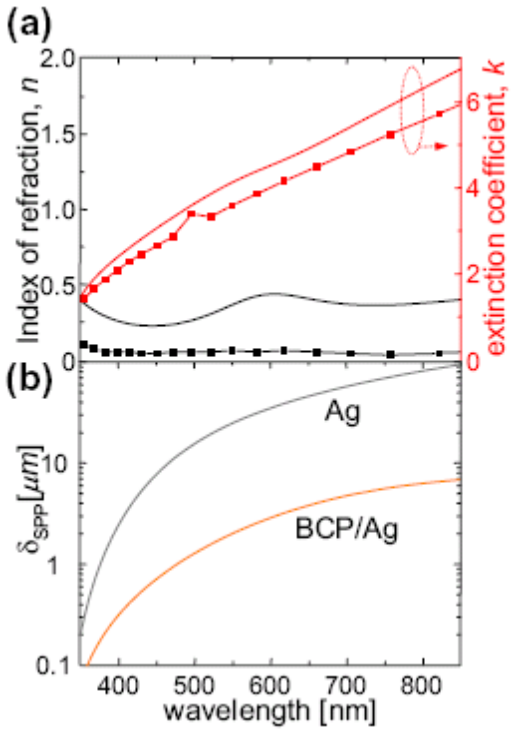

Figure 2.13 Silver penetration into BCP.

(A) The BCP-Ag bilayer was modeled as a single layer with the optical characteristics as shown (line). For comparison, the values as reported by Johnson & Christy are also shown (■).[64] **(B)** The propagation length, δ_{SPP}, which characterizes its propagation loss at a simple metal-air interface, is an order of magnitude smaller for the BCP/Ag bilayer at $\lambda = 532$ nm.

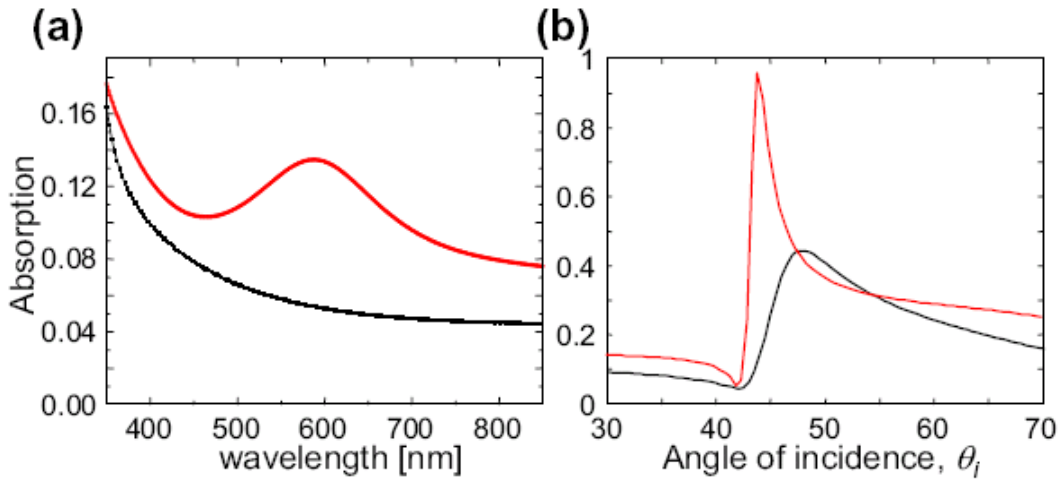

Figure 2.14 Silver penetration optical effects

(A) The measured spectral absorption at $\theta_i = 30^\circ$ of a 270 Å film of Ag on a 100 Å film of BCP on glass (●) is substantially greater than that of a 270 Å film of Ag deposited directly on glass (■). Absorption is calculated from $1 - R - T$, and cannot be distinguished from scattering. But when we assume scattering is negligible the determination of n and k yields an accurate model of the experimental photocurrent spectrum; see Figure 2.11. **(B)** The modeled angular absorption when $\lambda = 532$ nm is also greater for the Ag/BCP bilayer (red) compared to Ag only (black). In this simulation, light is incident from the glass.

Finally, the performance limits of the SPP detector may be assessed from the modeled internal quantum efficiency of the device, defined by the relation $\eta_{EQE} = \eta_{ABS} \cdot \eta_{IQE}$ and shown in Figure 2.10b. η_{IQE} incorporates all losses that can occur in photocurrent generation subsequent to light absorption in the stack, including exciton losses during diffusion, and insufficient charge collection. Small deviations in η_{IQE} are expected near total internal reflection due to spatial modulation of the optical field within the detector, which in turn varies the relative absorption of CuPC and C_{60}. But the main conclusion is that the organic SPP detector is primarily limited by exciton diffusion

losses which yield an internal quantum efficiency of only 13% near resonance. This may be due in part to photo oxidation of C_{60}.[69] To increase the sensitivity, the active absorbing layers can be made thinner, which has previously been shown to significantly increase η_{IQE} by increasing the probability of exciton dissociation at the active interface.[58] In addition, the relative enhancement in detection efficiency compared to the plane wave excitation will also increase. Thus, we expect that higher sensitivities are possible given device structure optimization.

The efficient excitation of organic photodiodes via photon-launched surface plasmon polaritons demonstrates that the efficiency of artificial reaction centers is enhanced when the incident radiation is coupled into a guided SPP mode. The enhancement of efficiency is most pronounced for thin reaction centers, with low exciton diffusion losses and low optical absorption, but very high internal quantum efficiency. We have reported a photocurrent increase of ~ 200% under resonance, but further optimization is possible. In absorption limited devices, the thickness of the active absorbing layers can be made thinner, which has previously been shown to significantly increase η_{IQE} by increasing the probability of exciton dissociation at the active interface[58]. Active semiconductor layers with thicknesses greater than the exciton diffusion length lowers dissociation efficiency. In addition, positioning the active absorbing organic semiconductor closer to the interface supporting SPPs should increase coupling into these modes. The peak external quantum efficiency of 12% represents a factor of 240 improvement in quantum efficiency over previous results. SPP excitation in the Kretschmann configuration resulting in internal QEs that are independent of

excitation method suggests SPP excitation of artificial reaction centers can proceed with high efficiency.

2.6 Energy transfer from antenna excitons to surface mode

The oscillating electric field of the radiative dipole at an excited molecule in the antenna layer can be damped by several mechanisms, resulting in energy transfer. These mechanisms are: (1) non radiative decay into phonons, (2) radiation of photons into free space modes not guided within the PV, (3) radiation into dielectric waveguide modes in the antenna/PV stack, and (4) non-radiative energy transfer into surface plasmon polariton modes at the adjacent metal interface. Photons in waveguide modes interact with the absorbing active layers in the artificial reaction center identically to normal light illumination.

Non-radiative decay is minimized in efficient antenna dye molecules. Thus, radiation into free space modes is the dominant process for an *isolated* oscillating dipole on an efficient dye molecule. But within a multilayer stack composed of metals and dielectrics, this process can be minimized. The rate of photon emission is described by Fermi's golden rule and depends on photonic mode density. For example, near a metal film, photonic mode density drops dramatically as visible light is strongly absorbed by free charges in the metal. Energetic transfer from excited molecules to SPP modes can occur with high efficiency to metallic slabs[77,78] and thin films.[79] The theoretical basis for dipole coupling to modes in a multilayer stack is well understood[32] and agrees well with experiments.[80]

The near field of the dipole is composed of an infinite sum of plane waves; it therefore contains components of a large range of wavevectors. Thus, the near field of the dipole has dispersion like this horizontal line, which can couple to photon modes in the various layers of the structure, plasmon modes, and waveguide modes; see Figure 2.15. The relative efficiency of coupling to each mode depends on its mode density and is governed by Fermi's golden rule.[78]

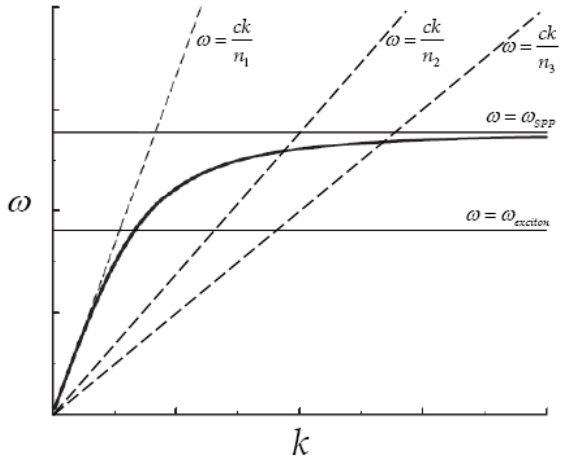

Figure 2.15 Dispersion relation, including excitons

Unlike photons, excitons can couple to photons (both in guided and unguided) and SPPs due to its broad range of accessible wavevectors in its near field. The dipole coupling rate will depend on local photonic mode density and relative orientation as dictated by Fermi's golden rule.

Within a multilayer stack energy transfer to guided electromagnetic modes is preferred. The stack acts as a waveguide since its refractive index, n ~ 2, higher than air or the glass substrate. To examine dipole coupling to thin silver films comprising the cathode of an organic PV, we use the method of Chance et al.[32] to simulate classical damping of an oscillating charge distribution near a multilayer stack to investigate energy

transfer to our artificial reaction center. Energy transfer is calculated directly from the Poynting vector.[81]

We model energy transfer within a multilayer organic PV following the demonstration in Celebi *et al*,[81] using dyadic Green's functions. To examine and quantify the efficiency of energy transfer within a multilayer organic PV stack, antenna excitons are modeled as oscillating charge dipoles and the efficiency of energy transfer from the antenna to the PV charge generating layers is found by evaluating the Poynting vector, $\boldsymbol{P}$. For each radiating dipole, total energy transfer to the charge generating organic semiconductors is found by calculating $\Delta\boldsymbol{P}$ within the photovoltaic charge generating layers.

Our prototype structure is a photovoltaic similar to a standard small molecular weight organic bilayer heterojunction cell:[82] glass/ Ag (400 Å)/ copper phthalocyanine (CuPC, 180 Å)/ CuPC:3,4,9,10 perylenetetracarboxylic bisbenzimidazole (PTCBI, 1:1, 180 Å)/ PTCBI (180 Å)/ bathocuproine (BCP, 100 Å)/ Ag (130 Å) / Antenna (1070 Å). We employ aluminum tris(8-hydroxyquinoline) (AlQ_3) as the antenna material. The dipole was located in the middle of the antenna layer for these calculations.

The coupling probability density of antenna excitons is shown in Figure 2.16 as a function of distance to the antenna-silver layer interface and the parallel component of the wavevector, u, normalized by the wavevector of an unconfined photon in the antenna layer. Normalized wavevectors with $u < 1$ correspond to radiative modes; $u > 1$ corresponds to non-radiative energy transfer. Since the energy coupling is dependent on the transition dipole orientation with respect to the plane of the interface, we consider the cases of perpendicular (Figure 2.16a) and parallel (Figure 2.16b) orientation separately.

In an isotropic film, the transition dipoles are 1/3 perpendicular and 2/3 parallel. At a given dipole distance, integration of the energy dissipation across wavevectors u yields unity.

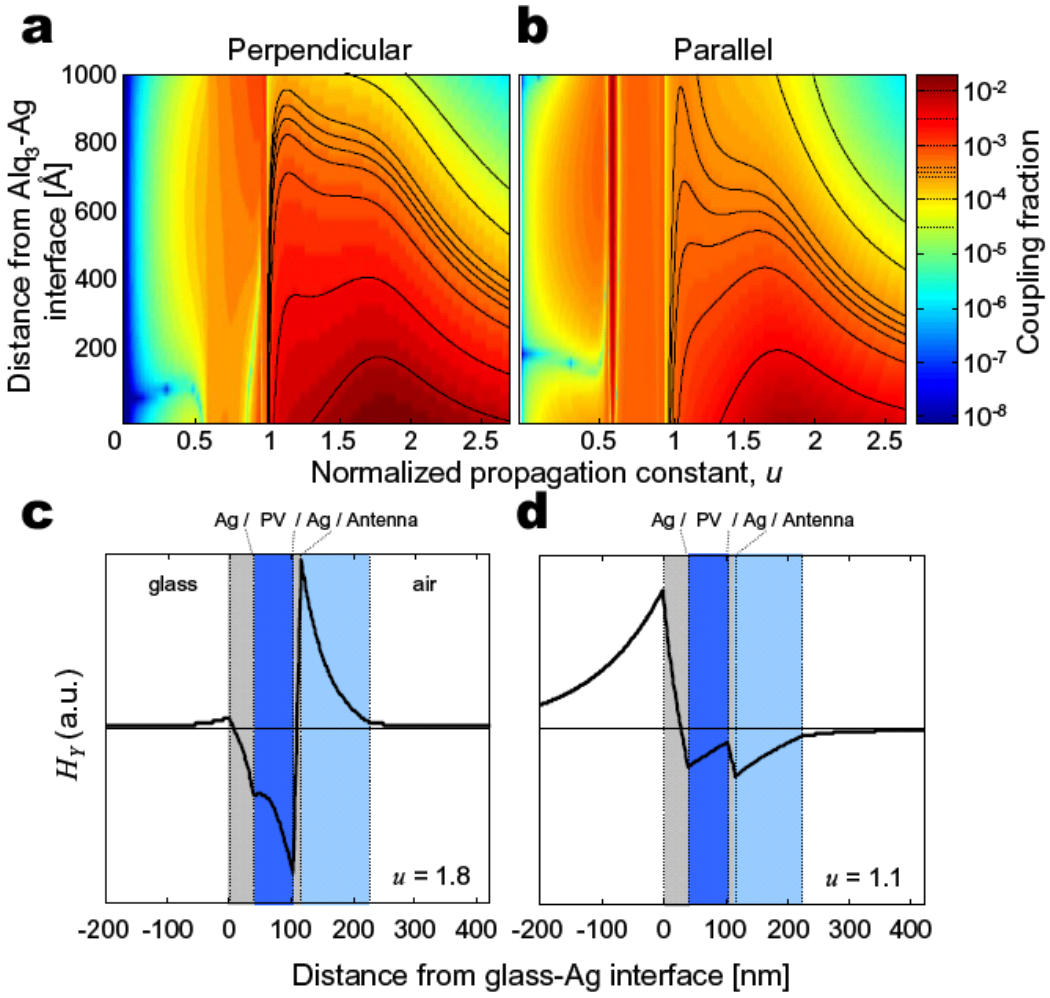

Figure 2.16 Exciton coupling fraction for (A) perpendicular and (B), parallel orientated dipoles with respect to the device plane

Modeling the exciton by a dipole, the probability of coupling is greatest for perpendicularly oriented dipoles into modes with $u>1$, corresponding to SPPs. Coupling to dielectric waveguide modes with $u<1$ is strongest for dipoles oriented parallel to the Ag-antenna interface. Coupling fractions are plotted on a logarithmic scale to facilitate visual interpretation. Contours are added (for $u > 1$ only, dotted lines on colorbar) to emphasize peaks in coupling fraction at $u \approx 1.8$ and $u \approx 1.1$. **(C)** The transverse magnetic (H_y) mode profile at $u = 1.8$ confirms that the SPP is localized at the antenna/photovoltaic interfaces and has significant overlap with the photovoltaic active semiconductor layers. **(D)** The SPP peak at $u = 1.1$ is localized at the glass/photovoltaic interface. The mode profiles were calculated by artificially setting absorption losses to zero in each layer, and calculating the stationary states of the stack.

One distinct SPP mode is evident in the calculations of exciton decay with a normalized propagation constant of u = 1.8, corresponding to localization at the antenna-silver interface (Figure 2.16c). A second mode with much weaker overlap with antenna excitons is also visible at u = 1.1, corresponding to the localization at the glass-silver interface (Figure 2.16d). Coupling to SPPs is especially strong approaching the thin silver electrode. For dipoles oriented parallel to the interface, both dielectric waveguide and SPP modes are significant, with radiation into dielectric waveguide modes dominant far from the antenna-silver interface. Total energy transfer as a function of dipole location and orientation is shown in Figure 2.17. For these calculations, we assume that the AlQ_3 antenna is doped with a randomly-oriented fluorescent dye with a free space photoluminescent (PL) efficiency of 70% and an emission wavelength of $\lambda = 615$ nm where CuPC absorbs strongly.

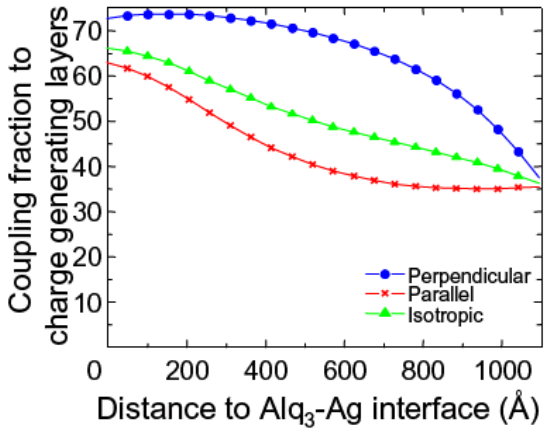

Figure 2.17 Antenna energy transfer to organic layers

Close to the AlQ_3-Ag interface, stronger energy coupling across the metal film occurs for perpendicularly oriented dipoles (■) due to their stronger emission into SPP modes. Over the first 1000 Å, the mean exciton coupling fraction to the organic layers is 52% for an isotropic distribution of dipoles.

In this PV stack, the average efficiency of energy transfer to the PV is 52% over the thickness of the antenna layer. Consistent with calculations of exciton coupling fractions in Figure 2.16, we find that energy transfer occurs predominantly via Förster coupling to the photovoltaic, mediated by the non radiative SPP mode localized at the top silver electrode. If the silver electrode separating the PV and antenna is thick, the SPP is confined to either the antenna or the PV. When the cathode is thin, the SPP mode extends into both the antenna and PV, and can mediate the transfer of energy. Consequently, the efficiency of energy transfer is maximized for thinner top silver contacts. In Figure 2.17, we observe that energy coupling via SPPs effectively increases the length of Förster energy transfer to ~ 1000 Å.

2.7 Experimental investigation of antenna organic photodetectors

To directly measure the efficiency of energy transfer from an antenna layer to an organic photodiode, η_{ET}, we fabricate an organic superlattice photodetector; see Figure 2.18. While energy transfer from external antennae has been proposed before[83], this work describes the first successful application to a photovoltaic device and quantification of energy transfer quantum efficiency.

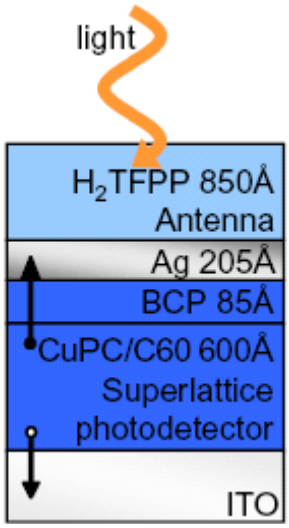

Figure 2.18 Structural configuration for antenna superlattice photodetectors

For measurement of energy transfer efficiency, high internal quantum efficiency superlattice photodetectors are used with the structure: glass/ ITO (1100Å)/ 20 alternating layers of CuPC and 3,4,9,10-perylenetetracarboxylic bisbenzimidazole (PTCBI) (each layer 15Å)/ BCP(85Å)/ Ag (205Å)/ 5,10,15,20-tetrakis(pentafluorophenyl)porphyrin (H_2TFPP) (850Å). The photoluminescent (PL) efficiency of the H_2TFPP antenna is tuned by adding 4,4'-Bis(*N*-carbazolyl)-1,1'-biphenyl (CBP) at varying concentrations. The devices are illuminated from the antenna side.

Under an applied bias, the organic superlattice photodetector is expected to exhibit an internal quantum efficiency close to 100% for excitation by SPP-modes.[84] We assume $\eta_{IQE} = 100\%$ which gives a lower bound for η_{ET}. The antenna material in this device is tetrakis(pentafluorophenyl)porphyrin (H_2TFPP). It is chosen for its combination of moderate PL efficiency ($\eta_{PL} = 2\text{-}3\%$) and high absorption coefficient ($\alpha = 10^6$ cm^{-1} at $\lambda = 400$nm) that allows nearly 100% of incident radiation to be absorbed in the absence of a cavity within the ~100 nm range of SPP-mediated energy transfer.

External quantum efficiency measurements were made at a reverse bias of 3.5V. The *measured* absorption and PL efficiency of the H_2TFPP antenna is used to determine η_{ET} from the increase in external quantum efficiency, $\Delta\eta_{EQE}$, i.e. $\eta_{ET} = \Delta\eta_{EQE}/\eta_{ABS}/\eta_{PL}$. Four H_2TFPP antennas were fabricated with varying PL efficiencies by blending H_2TFPP with different concentrations of CBP. The addition of CBP reduces concentration quenching. To eliminate energy transfer altogether, additional devices were fabricated with non-functional antennas comprised of H_2TFPP codeposited with 3.5% of CuPC. Using the quenched antenna as the baseline, and noting that the absorption of H_2FTPP is $\eta_{ABS} = 75\%$ for $\lambda \leq 450$ nm, we obtain $\eta_{ET} = (51\pm10)\%$, substantially higher than the resonant antenna result; see the inset of Figure 2.19. Note that the overall change in quantum efficiency is lower, however, due to the weak η_{PL} of H_2TFPP.

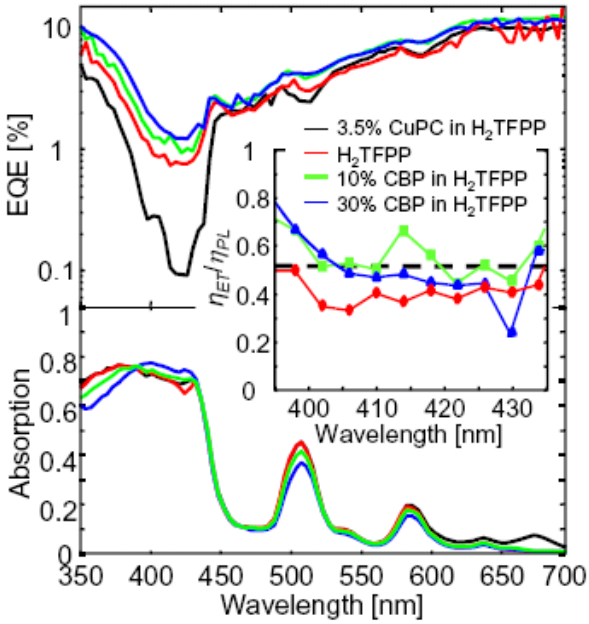

Figure 2.19 Measurement of energy transfer efficiency using superlattice organic photodetectors

(Top) Measurement of external quantum efficiency of devices with different antenna compositions: 3.5% CuPC in H_2TFPP $\eta_{PL} = 0\%$ (solid), 100% H_2TFPP $\eta_{PL} = (2.4\pm0.2)\%$ (long dashed), 90:10 H_2TFPP:CBP $\eta_{PL} = (2.5\pm0.3)\%$ (short dashed), 70:30 H_2TFPP:CBP $\eta_{PL} = (3.4\pm0.3)\%$ (dotted). **(Bottom)** Absorption spectra of different antenna layers on glass. **(Inset)** Calculation of energy transfer efficiency lower bound normalized by the PL efficiencies of the various antennas yields $\eta_{ET} = (51\pm10)\%$.

2.8 Experimental investigation of antenna organic solar cells

While the introduction of the antenna necessarily adds a step into the energy transduction process, it can be successfully employed in spectral regions where the absorption fraction of a PV cell drops below η_{ET}. The magnitude of energy transfer is approximately proportional to the free space photoluminescence (PL) efficiency of the antenna layer. Therefore, to test the activity of the antenna while avoiding interference effects due to

changes in device structure we fabricate identical photovoltaic cells with antennas of varying photoluminescence efficiency.

The optical characteristics of four antenna layers on bare glass are shown in Figure 2.20. In Figure 2.20a, the absorption of all layers are spectrally similar, with maximum absorption nearly identical at λ = 430 nm, corresponding to the Soret band absorption in the tetraphenyl porphyrin macrocycle centered at λ = 420 nm. The four remaining peaks at λ = 511, 540, 591, and 642 nm correspond to Q-band transitions. In addition, a single peak in the CuPc doped film at λ = 680 nm corresponds to the strong Q-band transition of the phthalocyanines.

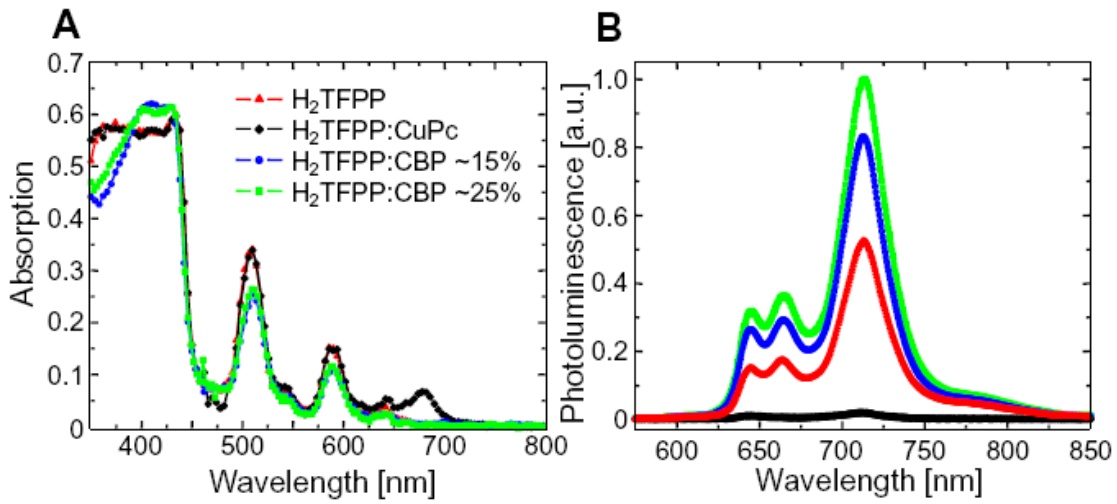

Figure 2.20 Optical characteristics of antenna layers

(A) The absorption of four 700 Å films deposited on bare glass under s-polarized illumination with $\theta_i = 30^\circ$ shows similar light extinction for all antenna layers. Maximum absorption occurs near $\lambda = 430$ nm, corresponding to the Soret band absorption in fluorinated tetraphenyl porphyrin. The peaks at $\lambda > 500$ nm correspond to Q-band transitions. Absorption in the H_2TFPP:CuPc film (♦) exhibits an additional peak at $\lambda = 680$ nm corresponding to the strong Q-band transition of the CuPc. **(B)** The photoluminescence of each film under unpolarized illumination at $\lambda = 408$ nm show maximum emission at $\lambda = 713$ nm, with two higher energy peaks at $\lambda = 644$ and 665 nm. The efficiency of re-emission is tuned by the incorporation of either a strong quencher (CuPc, ♦) or transparent, inert spacer molecule (CBP, ● and ■) to reduce the effect of H_2TFPP luminescence concentration quenching. The PL efficiencies of the four antenna layers are 0%, 2.4%, 3.5%, and 4.3% for H_2TFPP:CuPc, H_2TFPP, H_2TFPP:CBP(15%), and H_2TFPP:CBP(25%) films, respectively.

In Figure 2.20b, the three prominent emission peaks of H_2TFPP are visible at $\lambda = 644$, 665, and 713 nm. Photoluminescence (PL) of H_2TFPP molecules in solid films are limited by concentration quenching. We adjust the molecular concentration by co-depositing CBP as an inert, transparent filler material. The PL efficiency is positively correlated with increased intermolecular spacing consistent with concentration quenching

limited emission. For quenched films, H_2TFPP excitons undergo intermolecular Förster energy transfer (see Section 3.8.1 for discussion of Förster transfer) to CuPc which absorbs strongly between λ = 550 and 750 nm. To quantify the PL efficiency, the spectra were compared to a layer of aluminum tris(8-hydroxyquinoline) (AlQ_3) whose quantum efficiency has been previously measured.[85] Using AlQ_3 as a reference film, the PL efficiencies of the four antenna layers are 0%, 2.4%, 3.5%, and 4.3% for H_2TFPP:CuPc, H_2TFPP, H_2TFPP:CBP(15%), and H_2TFPP:CBP(25%) films, respectively.

The external quantum efficiencies of these devices as a function of wavelength are shown in Figure 2.21. In Figure 2.21a, all devices exhibit similar external quantum efficiencies outside the region of strong antenna absorption for $\lambda > 450$ nm, indicating that interference effects do not cause differences in quantum efficiency. However, over the region of $350 < \lambda < 430$ nm, where H_2TFPP absorption is the strongest, the devices with functioning antenna layers exhibit increased external quantum efficiency. This increase in photodiode performance due to energy coupling is highlighted in Figure 2.21, where the increases in photocurrent relative to devices with non-emissive antennas are plotted. The maxima of increased photocurrent spectrally match the extinction coefficient of H_2TFPP and correlate with photoluminescence efficiency, consistent with our description of energy transfer.

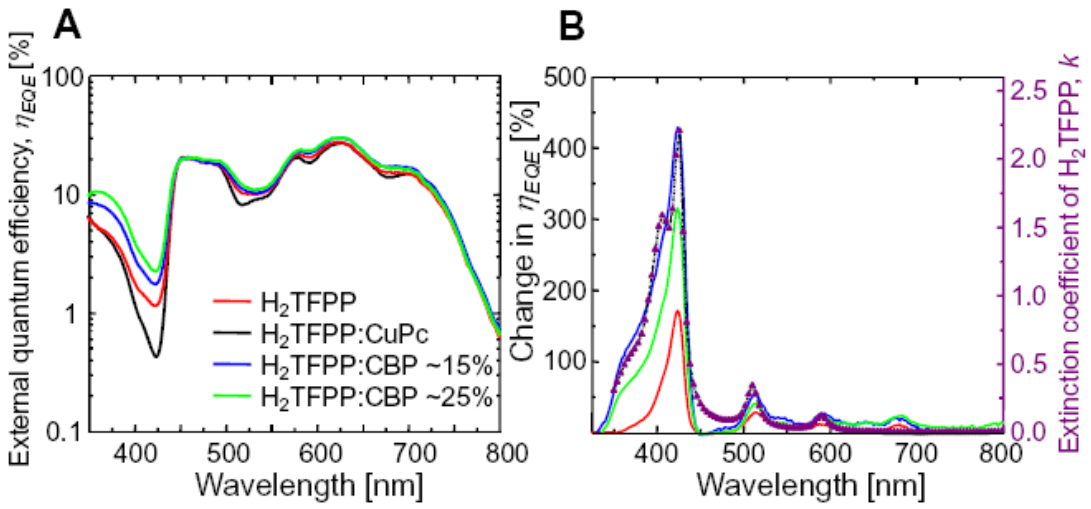

Figure 2.21 External quantum efficiency for antenna device

(A) Devices with functional (reemitting) H_2TFPP antenna layers exhibit **(B)** an increase in external quantum efficiency over the wavelength range where H_2TFPP absorption occurs (extinction coefficient of H_2TFPP: ▲). The photocurrent spectra are identical outside the spectral range where H_2TFPP absorbs. The structure of the diodes is glass/ Ag(180 Å)/ CuPc(245 Å)/ C_{60}(170 Å)/ BCP(85 Å)/ Ag(145 Å)/ H_2TFPP:*X*(700 Å). Functional antennas are either undoped (red) or employ the inert spacer molecule (*X* = CBP, green and blue), whereas nonfunctional antennas employ the quencher *X* = CuPc, black). Additional photocurrent due to energy transfer occurs strongly at the H_2TFPP Soret band maxima at λ = 425 nm and its Q-bands at 644 and 665 nm.

The increase in external quantum efficiency, $\Delta\eta_{EQE}$, originates in sequential completion of three processes:

$$\Delta\eta_{EQE} = \eta_{ABS}^{Antenna} \cdot \eta_{ET} \cdot \eta_{IQE} \tag{7}$$

where $\eta_{ABS}^{Antenna}$ is the normalized absorption in the antenna layer, η_{ET} is the energy transfer efficiency across the silver electrode and is dependent to the PL efficiency of the antenna molecules, and η_{IQE} is the internal quantum efficiency of the artificial reaction

center. The maximum energy transfer efficiency occurs where absorption is maximum. Using a transfer matrix formulism[49], we calculate absorption in the antenna layer and find $\eta_{ABS}^{Antenna}$ = 60% for all antenna compositions at λ = 430 nm, consistent with separate measurements of films on bare glass in Figure 2.21a.

The $\eta_{ET} \cdot \eta_{IQE}$ product represents a lower bound for total energy coupling efficiency across the silver film, η_{ET}. $\eta_{ET} \cdot \eta_{IQE}$ is greatest for the H_2TFPP:CBP(25%) antenna at 3.1%. This value is primarily limited by the relatively low quantum efficiency of reemission. If the efficiency of energy transfer is assumed to be a linear function of the free space photoluminescence efficiency, the ratio $\eta_{ET} \cdot \eta_{IQE} / \eta_{PL}$ for the H_2TFPP:CBP(25%) device is 72.1%, consistent with a modeled η_{ET} / η_{PL} of 108% when $\eta_{IQE} < 1$ and noting that the emission efficiency is enhanced over the free space condition. Other H_2TFPP based antennas yield similar values for $\eta_{ET} \cdot \eta_{IQE} / \eta_{PL}$.

H_2TFPP molecules absorb strongly but reemit with low efficiency. We also investigated antenna PVs with antenna films made from aluminum tris(8-hydroxyquinoline) (AlQ_3) doped with the laser dye 4-dicyanomethylene-2-methyl-6-(p-dimethylaminostyryl)-4*H*-pyran (DCM) and bilayer reaction centers based on CuPc and 3,4,9,10-perylenetetracarboxylicbis-benzimidazole (PTCBI). AlQ_3:DCM layers absorb less light but emit with higher solid state quantum yield.

We have measured reflection and transmission to calculate total absorption in the device with AlQ_3:CuPC antenna at the measured fluorescence maximum of DCM at λ = 615 nm and calculate η_{IQE} =5%. These values result in a total energy coupling efficiency across the silver film of $\eta_{EnergyTransfer}$= 46%, similar to the porphyrin antenna devices. The

overall gain in η_{EQE} is limited by low absorption in the antenna layer. These devices show significantly lower relative increases in photocurrent in the emissive versus non-emissive case, as there is a significant baseline photocurrent resulting from direct transmission through the antenna film. These devices demonstrate that energy transfer is not unique to the H_2FTPP system.

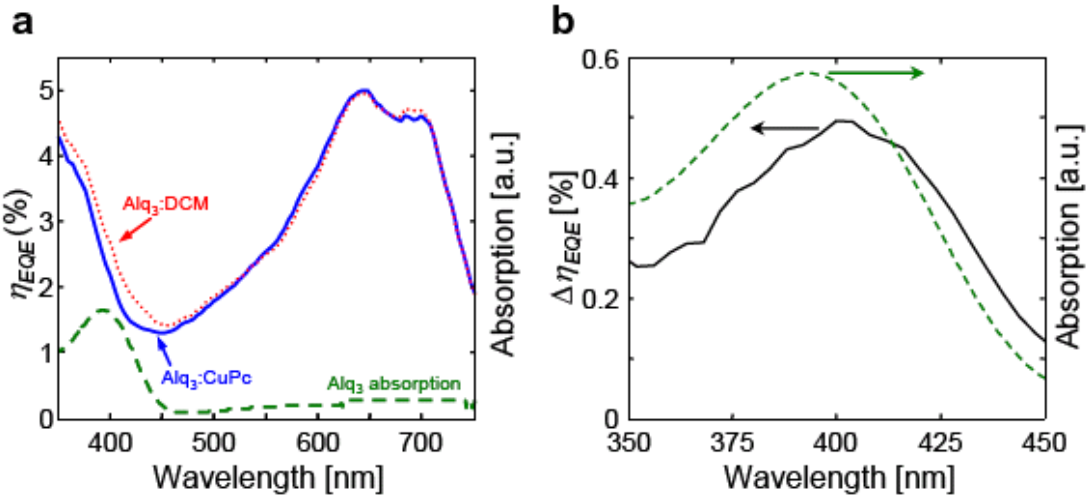

Figure 2.22 External quantum efficiency for antenna device

(A) Devices with external AlQ_3 functional antenna layers (dotted) exhibit an increase in external quantum efficiency over the wavelength range where AlQ_3 absorption occurs (dashed). The photocurrent spectra are identical outside the spectral range where AlQ_3 absorbs. **(B)** The change in external quantum efficiency correlates well with AlQ_3 absorption.

2.9 Cavity antenna organic solar cells

Efficient SPP-mediated energy transfer requires highly efficient photoluminescent (PL) antenna materials. Unfortunately, the PL efficiency of highly absorptive organic semiconductors is typically diminished by intermolecular energy transfer known as concentration quenching. To exploit less absorptive materials with higher PL efficiencies,

η_{PL}, we enclose the antenna within a resonant cavity. As shown in Figure 2.23a, the resonant antenna is employed in place of the silver mirror on the back of the cell. Off resonance the antenna acts as a mirror, but near the resonant wavelength the antenna absorption is significantly enhanced, and energy is fed back into the PV cell via SPP-mediated energy transfer. Thus, the resonant antenna structure supplements the performance of the PV cell at resonance, with no degradation off-resonance.

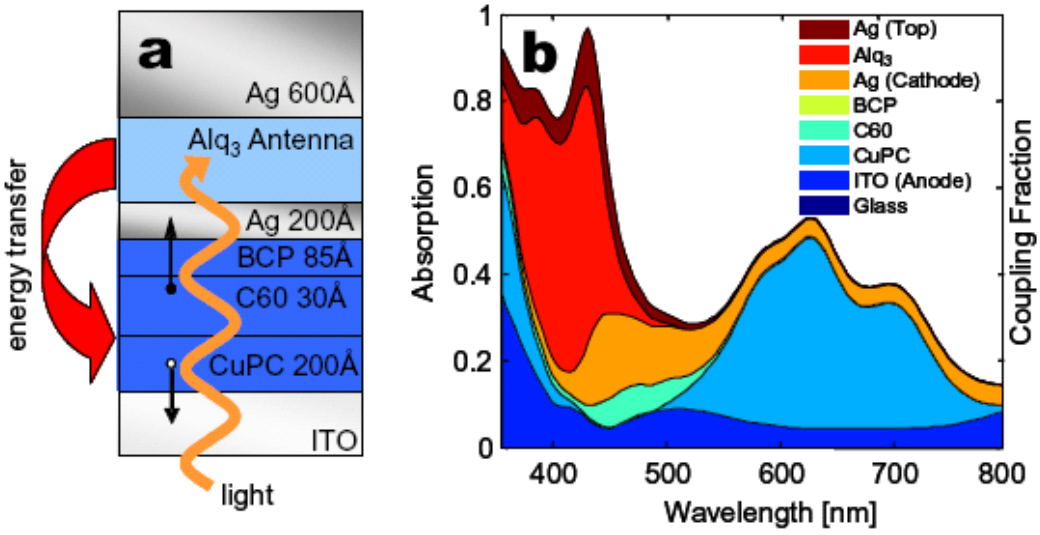

Figure 2.23 Structure and absorption characteristics of cavity antenna solar cells

(A) Devices with resonant antenna cavities have the structure: glass/ Ag (200 Å)/ CuPC (200Å)/ C60 (250Å)/ BCP (85Å)/ Ag (200Å)/ antenna / Ag (600Å). The tris(8-hydroxyquinoline) aluminum (AlQ_3)-based antenna is 700Å thick. To tune the PL efficiency of the AlQ_3 antenna we introduce either CuPC or 4-dicyanomethylene-2-methyl-6-(p-dimethylaminostyryl)-4*H*-pyran (DCM) at 1% weight ratio. To highlight the effect of the AlQ_3 antenna effect the C60 thickness is reduced to 30Å. (For devices with thicker C_{60} layers see Reference 86.) The devices are illuminated from the glass side. **(B)** Absorption in all device layers with illumination from glass side and an AlQ_3-based antenna thickness of 700Å. The tuned cavity results in significantly increased absorption in the antenna layer.

We couple resonant antennas to phthalocyanine-based PV cells, which exhibit a gap in their absorption spectra between the Q and Soret bands. To help fill this gap, we use rubrene, a common organic light emitting device material, which has an absorption coefficient of $\alpha \sim 10^4$ cm^{-1} at $\lambda \sim 550$nm. Rubrene functions as the Förster energy transfer donor for the laser dye 4-(dicyanomethylene)-2-*t*-butyl-6-(1,1,7,7-tetramethyljulolidyl-9-enyl)-4H-pyran (DCJTB), which has high photoluminescence efficiency; $\eta_{PL} = (90\pm10)\%$.

To tune the resonant antenna PV shown in Figure 2.23a, we calculate the expected optical absorption in each layer.[49] A 1250Å-thick film of 30% rubrene and 2% DCJTB in transparent carbazole biphenyl (CBP) tunes the cavity close to the $\lambda \sim 500$ nm absorption peak of rubrene. The wavevector dependence of energy transfer from the antenna to the PV is shown in Figure 2.24a. Energy transfer occurs predominantly via non-radiative coupling, mediated by SPP modes with $u > 1$. Near the cathode, $\eta_{ET} = 54\%$, but the efficiency decreases beyond ~85nm. Averaged over the antenna, $\eta_{ET} = 31\%$.

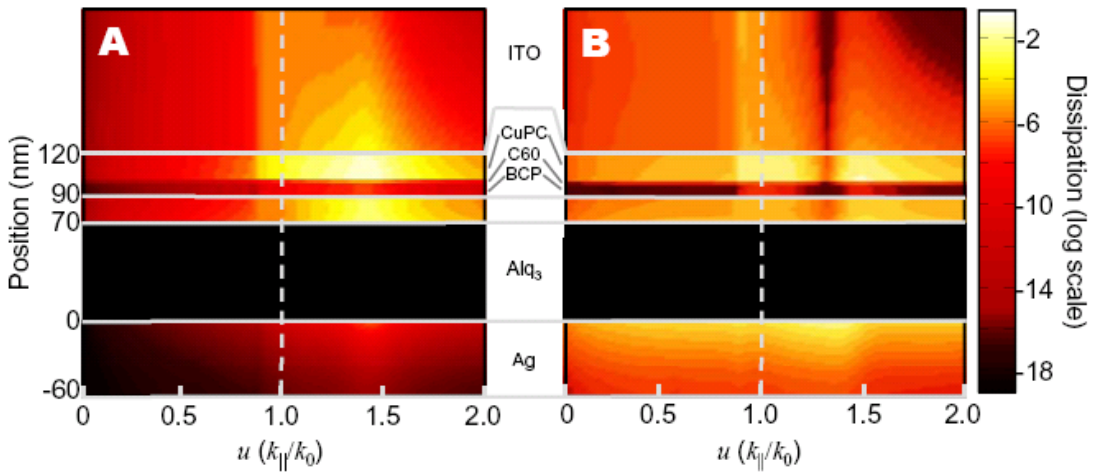

Figure 2.24 Spectral dependence of energy transfer for dipoles oriented perpendicular (A) and parallel (B) to the device plane

Coupling is greatest for perpendicularly oriented dipoles into modes with u>1, corresponding to SPPs. Coupling to dielectric waveguide modes with u<1 is also strong for dipoles oriented parallel to the Ag-antenna interface. Coupling is strongest to the CuPC layer.

To demonstrate the potential improvement possible using an external resonant antenna in conventional C60/CuPC PV cells, we compare a control device without the antenna to devices with an antenna composed of 30% rubrene and 2% DCJTB in CBP. Quenched antennas were also fabricated with the addition of 2% of the quenching material CuPC instead of DCJTB. External quantum efficiency measurements were made using a xenon lamp with monochromator, chopped at $f = 90$ Hz, and measured using a lock-in amplifier. Light intensity was measured with a calibrated silicon photodiode. The external quantum efficiencies of these devices as a function of wavelength are shown in Figure 2.25 and compared to the reflectivity of the antenna cavity. The absorption of the antenna (from Figure 2.23b) and the internal quantum efficiency at the PL maximum of DCJTB, $\eta_{IQE} = (30\pm10)\%$ at $\lambda = 640$nm, is used to

determine η_{ET}. This yields $\eta_{ET} = (25\pm10)\%$, consistent with the calculated result of $\eta_{ET} = 31\%$. As illustrated, with improved energy transfer, the efficiency in the spectral gap between absorption peaks could be significantly improved. The absorption modeling also demonstrates that the improved quantum efficiency outside the region where the resonant cavity absorbs is due to reflectivity changes that modify the electric field profile within the device.

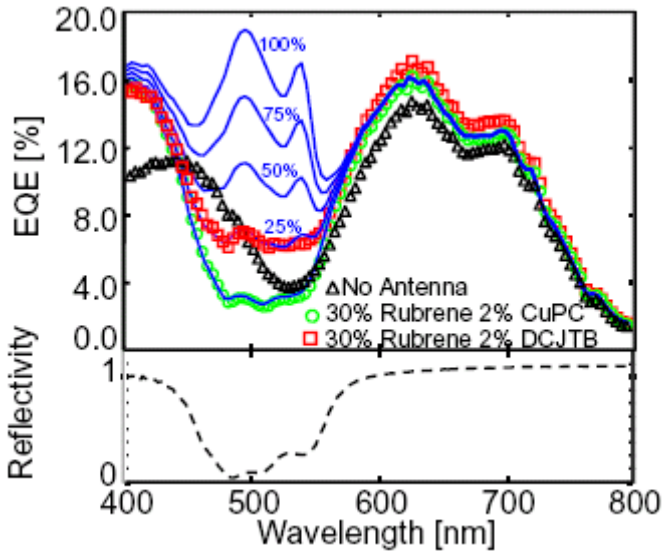

Figure 2.25 External quantum efficiency (EQE) for resonant antenna devices

Devices with functional external rubrene-based antenna layers exhibit an increase in EQE over the wavelength range where rubrene absorption occurs and the cavity reflectivity decreases. Functional antennas (□) employ the laser dye, DCJTB, whereas nonfunctional antennas (○) employ the quencher CuPC. The functional antenna shows a significant performance enhancement versus both the quenched antenna and devices fabricated without any antenna (**Δ**). Comparison with modeling (—) indicates that the energy transfer efficiency is approximately 25%. We also show the expected EQE for energy transfer efficiencies of 0%, 50%, and 75%.

2.10 Antenna PV outlook

On the basis of these results, we anticipate that energy coupling from external antenna layers into thin film photovoltaics provides a flexible route towards achieving high efficiency devices. Initial devices exhibit energy coupling of at least 30-50%, demonstrating plasmon mediated coupling is a viable and efficient method for optical pumping of solar cells. Although the introduction of the antenna adds a step into the energy transduction process, the decoupling of photon absorption and exciton dissociation can be exploited to increase overall absorption and internal efficiency separately through judicious device and process design. Due to increased photocurrent alone, this device architecture enables an increase of approximately 50% for identical PV materials.

The reaction center is freed from the constraint of broadband optical absorption, offering the opportunity to design an artificial reaction center on the basis of high internal quantum efficiency, low series resistance, and stability, negating the necessity for disordered bulk heterojunctions and thick resistive layers to achieve high external quantum efficiency.

Since the optically absorbent component need not conduct excitons or charge, new antenna materials are possible, including J-aggregates, quantum dots, and biomaterials, including photosynthetic antennas. Antenna materials should be chosen for high optical absorption and photoluminescent efficiency. With mixed antenna material and undergo cascade exothermic energy transfer, the photoluminescence requirements is moved to the terminal emitter and weak absorption can be mitigated by using many materials and the long spatial diffusion requirements can be relaxed; see Figure 2.26.

With graded dipole orientation control, overall antenna thickness can be reduced and energy transfer efficiencies can be increased.

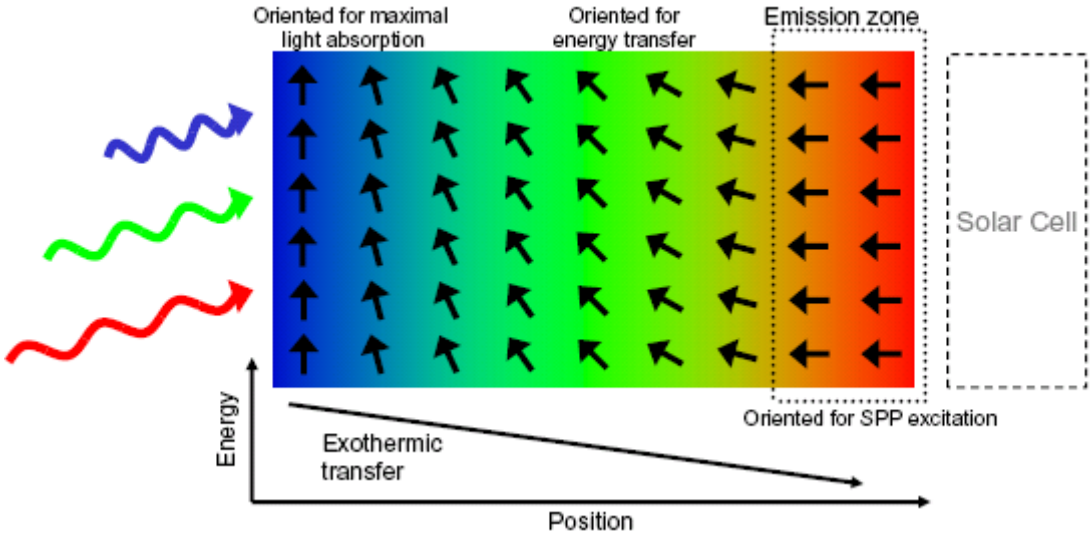

Figure 2.26 Idealized antenna configuration

To increase conversion efficiency in the antenna structure, it is desirable to have maximal optical absorption across the visible. This can be achieved if light collection is spatially separated from emission. To further increase the efficiency of each, the antenna materials can be oriented for maximal overlap with incoming or outgoing modes. An energy gradient with decreasing distance will make light collection more efficient, similar to exothermic energy coupling in biological light harvesting antennas (See Section 1.5.1).

Separation of the functions of light absorption and exciton dissociation constitutes a significant photosynthetic redesign, unaccompanied by the limitations of traditional organic PV. Initial device performances are modest yet promising. The separation of optical and electrical functionalities discussed here represents a completely synthetic implementation where the active materials of the artificial antenna and reaction center are amorphous films of pigment semiconductors. However, it is possible to construct devices

where one or both components are biological in origin. The excellent absorption characteristics of chlorosomes and charge separation characteristics of reaction centers are tempting, the tradeoff between performance and stability may dictate which type of devices yield high performance and reliability.

Chapter 3 Organic Solar Concentrators

3.1 Solar concentrators

Concentrators operate by partially separating the functions of light collection and charge generation. They accomplish this by using an optical system to concentrate sunlight onto solar cells, allowing for a reduction in the cell area required for generating a given amount of power. Concentrators can significantly reduce electricity cost by replacing expensive PV converter area with a less expensive optical collector, which also provides the opportunity to use very high performance solar cells that would otherwise be prohibitively expensive.

Conventional concentrators use reflection or refraction to focus light and are referred to as geometric or passive concentrators. High photon flux carries with it extra considerations:

1. As photons with energies greater than the electrical bandgap thermalize after absorption, high optical concentration of broadband light will result in increased heating. Since solar cell conversion efficiency drops as its

temperature increases, cooling is usually employed to manage these increased thermal loads, adding complexity, capital, and operations/maintenance costs. Cell packaging to accommodate the cooling system also complicates solar cell and module design. Typical normalized efficiency temperature degradation coefficients are 0.2-0.4%/^{o}C.[87]

2. The level of concentration is limited by the sine brightness equation to $C \leq 1/\sin^2\theta$ where θ is the acceptance angle of the optical collector.[88] For very high concentration levels (>500), θ becomes vanishingly small (see Figure 3.1 and Section 3.3.1). Practically, these means the collector must track the sun, adding complexity, capital, and operations/maintenance costs.

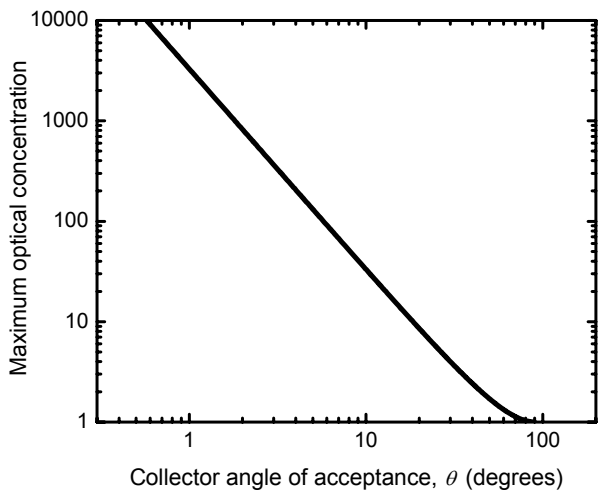

Figure 3.1 Maximum concentration versus acceptance angle

Under geometric concentration, optical flux is conserved. As the beam area is decreased after passing through the concentrator, the angular divergence increases. Concentration is achieved by trading angle for beam area. High passive optical concentration is only possible by restricting the angle of acceptance, so only direct rays can be collected and the light source must be mechanically tracked to maintain line of sight.

3. The electrical current that passes through the solar cell increases linearly with light flux. Thermal power dissipated through joule heating grows as the square of the current, the electrical resistance to current flow must be reduced as much as possible to manage resistive heating. Very low resistance solar cells are expensive to produce, adding to overall system cost.
4. Unlike flat solar modules, large tracking systems will shadow each other during parts of the day if not placed far apart. Since each system must be surrounded by a buffer zone, real estate costs increase the system price.

Concentrating systems are not well suited to the current solar electric market that typically serves small loads. Because they require maintenance, increased land use, and can operate at very high temperatures, they are better suited for large utility scale applications with dedicated oversight. Utility scale installations must generate electricity at much lower costs than residential rooftop systems due to the differential rate structure that exists in most markets. For these reasons, costs are too high to compete with wind or conventionally generated electricity and solar utilities have not surpassed pilot status. Although there are many variations of optical collectors that mitigate some of these strict requirements, they typically do so by trading some of the major benefits, and they too are not economically competitive.

3.2 Fluorescent concentrators

In 1976, Weber and Lambe proposed a new type of concentrator that utilized the sequential absorption and emission of light into confined modes of a simple light guide to focus light.[89,90] These active, fluorescent concentrators can collect both diffuse and direct radiation to levels above those dictated by the sine brightness equation.

In its initial design, a plastic or dielectric material is doped with an organic dye or fluorescent inorganic molecule. Light is absorbed at one energy and is re-emitted at a lower energy. A portion of the light is trapped in the plate via total internal reflection and is collected at the edge exit apertures; see Figure 3.2.

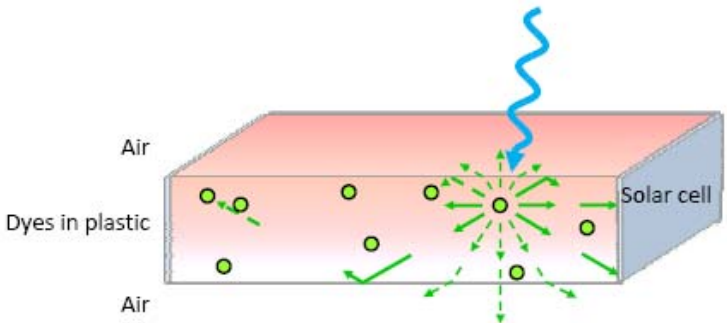

Figure 3.2 Structural configuration of a fluorescent concentrator

Active chromophores are dispersed in a macroscopic host matrix. For high efficiency, the substrate must be transparent to directly incident and emitted light. One or more edge faces is covered with either solar cells or mirrors. Dashed lines represent light eventually lost due to waveguide outcoupling or self-absorption.

The process is quantum and does not rely on geometric optics. The absorbing molecules operate as optical heat pumps, where thermal energy is dissipated to increase the chemical potential of photons in other modes. Because of this, the maximum levels of

concentration are limited by the thermodynamics of Boson gases, dependent on the Stokes shift; see Section 3.3.2.[88] The energy difference between absorption and emission isolates the guided photon population from the unguided incident photons. High optical is possible without tracking and light absorption occurs from both direct and diffuse radiation.

Fluorescent concentrators possess many favorable characteristics:

1. Energy is dissipated in each chromophore prior to emission. If the emitted photons possess energy nearly equal to the bandgap at the edge mounted solar cell, the cell will experience significantly lower thermal heating (see Section 3.6). Thus even at very high concentration levels, passive cooling through the module housing is possible.
2. Unlike passive concentrators, the angular acceptance of fluorescent collectors is limited by reflective entry and not conservation of light flux. In principle, very high concentration levels are possible without mechanical tracking.
3. Fluorescent concentrators can be configured in a flat plate geometry, so large inter-module spacing is not required, decreasing real estate costs. The flat panel shape is also identical to existing modules, which should ease adoption into solar markets.
4. The collector is compatible with low cost processing techniques like casting and molding and vastly simpler than PV cells. The only components are the waveguide, the dyes and a package. No conductive electrodes are required on the collector. This is important because the transparent conductive electrode is one of the most expensive component in thin film PV cells; see Section 1.3.[91]

The collector also does not require potentially scarce materials such as indium, gallium, or tellurium.

5. Localized dark spots on solar module can permanently damage individual solar cells in a series connection.[92] The photocurrent generated from non-shaded cells is forced through the dark devices like a current source. In the absence of local current generation, this current can only be accommodated by developing a large reverse bias (breakdown) voltage. Thus the shaded device will act a power sink for all illuminated devices and will rapidly heat and potentially fail. This process is alleviated by including bypass diodes placed to sink this excess power; although they preserve system integrity, conversion efficiency significantly drops. Since directionality is scrambled in fluorescent concentrators, they are intrinsically immune to localized dark spots.
6. Fluorescent concentrators are inherently tolerant of defects because of the many parallel paths available between luminescent dyes and the encircling PV cells. In contrast, short or open circuit failures in PV arrays can be fatal and render the whole device unusable.

There was great interest in fluorescent collectors in the late 1970s and early 1980s, but initial demonstrations were low efficiency and operated at very low optical flux gains, where the flux gain is the optical concentration corrected by the decrease in power conversion efficiency. The best reported system was from the California Institute of Technology which operated at a geometric gain of 68 and an efficiency of 1.3%,

resulting in a flux gain of 5.1.[93,94] Several dozen papers have been published since, but no significant breakthroughs have been reported.

Conversion efficiency and optical concentration are severely limited by the process of self-absorption, whereupon a ground state chromophore absorbs a photon en route to the exit aperture. No existing dyes simultaneously satisfied the strict requirements of chromophore self-transparency, high quantum yield of emission, and excellent stability. The prospects of solving these issues appeared grim, and most reviews and textbooks on photovoltaic concentrators neglect to mention the existence of fluorescent concentrators.

3.3 Thermodynamic concentration limits of solar concentrators

The limits of optical concentration are ultimately set by thermodynamics and can be derived from considerations of entropy and energy conservation and are different for elastic and inelastic processes.

3.3.1 Inelastic processes

This derivation closely follows that of Smestad et al 1990.[88] Considering an optical transformer with entrance aperture A_1 and exit aperture A_2, light enters the system with an angular spread defined by $\pm\theta_1$ and exits with spread $\pm\theta_2$.; see Figure 3.3. Photons pass through the system inelastically; that is, they leave the aperture unchanged in energy. The radiance of the light, L, is the flux per unit solid angle, Ω, per unit projected angle.

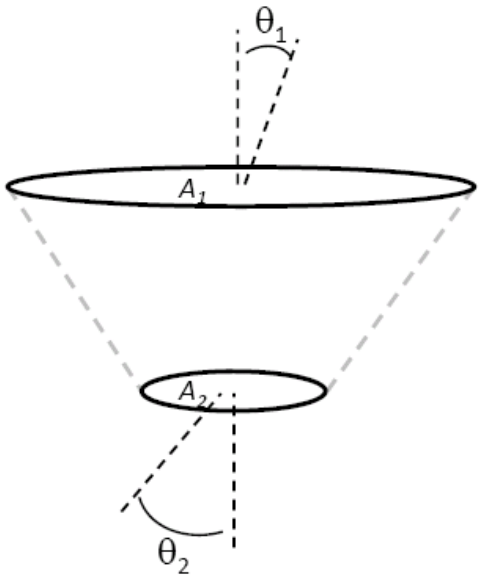

Figure 3.3 Optical transformer

The apertures has entrance areas A_1 and A_2, with angular spreads θ_1 and θ_2.

The flux incident on the top aperture from a Lambertian source is then given by the integral of the radiance times the area and projected solid angle, or

$$\Phi_1 = \int L_1 A_1 \cos\theta d\Omega = \int_0^{\theta_1} 2\pi L_1 A_1 \sin\theta \cos\theta d\theta = \pi L_1 A_1 \sin^2\theta_1 \tag{8}$$

and similarly for the flux leaving the exit aperture. The concentration is given by ratio of the illuminations of the exit and entrance apertures, or

$$G = \frac{\Phi_2 / A_2}{\Phi_1 / A_1} = \frac{L_2 \sin^2\theta_2}{L_1 \sin^2\theta_1} \tag{9}$$

For a passive, geometrical concentrator where the optical system does not affect the energy of each photon, flux and radiance are conserved throughout the transformer. This means that as the beam area is decreased, the divergence, is increased to compensate. Put another way, area is traded for angle to achieve optical concentration. The maximum concentration is then given by

$$G = \frac{\sin^2 \theta_2}{\sin^2 \theta_1} = \frac{1}{\sin^2 \theta_1} \tag{10}$$

where the maximum occurs when output aperture is fully divergent. If the concentrator is made of medium with refractive index n, then the concentration limit is increased by the factor n^2.

To reach high concentration levels (>500), θ becomes vanishingly small; this is only possible by orienting the optical system directly at the sun as it transmits the sky, adding complexity, capital, and operations/maintenance costs.

3.3.2 Elastic processes

Fluorescent concentrators are elastic systems, as vibrational relaxation of the absorbing chromophores decreases the energy of the emitted photon and the conservation of radiance no longer holds. The above derivation must be generalized to find the thermodynamic concentration limit. This section closely follows the treatment of Yablonovitch (1980).[95]

The entropy change associated with the loss of a photon from the incident Bose field is

$$\Delta S = -k \log\left(1 + \frac{8\pi n^2 \upsilon^2}{c^2 B}\right) \tag{11}$$

where υ is the frequency, n is the refractive index, k is the Boltzmann constant, and B is the brightness of the incident field in units of photons per unit area, bandwidth, time, and solid angle 4π. The entropy increase in the field inside the fluorescent collector is then

$$\Delta S = k \log\left(1 + \frac{8\pi n^2 \upsilon_2^2}{c^2 B_2}\right) + \frac{h(\upsilon_1 - \upsilon_2)}{T} \tag{12}$$

where additional term is the thermal dissipation of the Stokes shift, υ_1- υ_2 at temperature *T*. According to the second law of thermodynamics, the change in entropy of the input and output fields must be greater than zero, so:

$$k\log\left(1+\frac{8\pi n^2\upsilon_1^2}{c^2B_1}\right)\Bigg/\left(1+\frac{8\pi n^2\upsilon_2^2}{c^2B_2}\right)\leq\frac{h\left(\upsilon_1-\upsilon_2\right)}{T} \tag{13}$$

Under terrestrial condition, this inequality may be simplified find:

$$C\equiv\frac{B_2}{B_1}\leq\frac{\upsilon_2^2}{\upsilon_1^2}\exp\left(\frac{h\left(\upsilon_1-\upsilon_2\right)}{kT}\right) \tag{14}$$

Accordingly, fluorescent concentrators are not dependent on incident angular range and tracking is not required. The ultimate concentration limit is sensitively linked to the Stokes shift.

Light transport losses are also sensitively linked to the Stokes shift through the process of self absorption. The strict requirements of dye self-transparency have historically limited actual performance to at least two orders of magnitude lower than the thermodynamic limit.

3.4 Organic Solar Concentrators

The strict requirements of dye self transparency can be addressed if the physical structure of fluorescent concentrators is redesigned. In this work, we construct organic solar concentrators (OSCs) by depositing a thin film of dye molecules onto a clear substrate; see Figure 3.16a. If the refractive index of the coating and substrate match, the coated and cast structures are optically equivalent to guided light. However, the thin film geometry allows greater control over the microscopic separation between dye molecules, and we are able to apply the recent advances of organic optoelectronics to fluorescent collectors.

Notably, we employ Förster energy transfer,[96] solid state solvation,[97] and phosphorescence[98] to relax the constraints on the active optical materials. Thin film organic semiconductor technology allows us to precisely control intermolecular energy transfer using low-cost fabrication processes.

We continue with brief discussions of OSC trapping efficiency and thermally-set concentration limits, and review Förster energy transfer, solid state solvation, and phosphorescence.

3.5 OSC loss processes

In a simple cladding-core-cladding multimode waveguide populated with isotropically distributed electromagnetic radiators, the solid angle trapped by total internal reflection is

$$\Omega = 2\pi \int_{-\sin^{-1} n_{clad}/n_{core}}^{\sin^{-1} n_{clad}/n_{core}} d\theta \sin\theta \tag{15}$$

Normalizing by the full 4π solid angle gives the trapping efficiency, η_{trap}

$$\eta_{trap} = \sqrt{1 - \frac{n_{clad}^{\ 2}}{n_{core}^{\ 2}}} \tag{16}$$

Equation 1 is plotted in Figure 3.4 when $n_{clad} = 1$. For the simple air-clad glass waveguide, with a core refractive indices of $n_{core} = 1.5$, approximately 75% of the re-emitted photons will be trapped. To maximize η_{trap} in this simple structure, it is desirable to make n_{core} as high as possible.

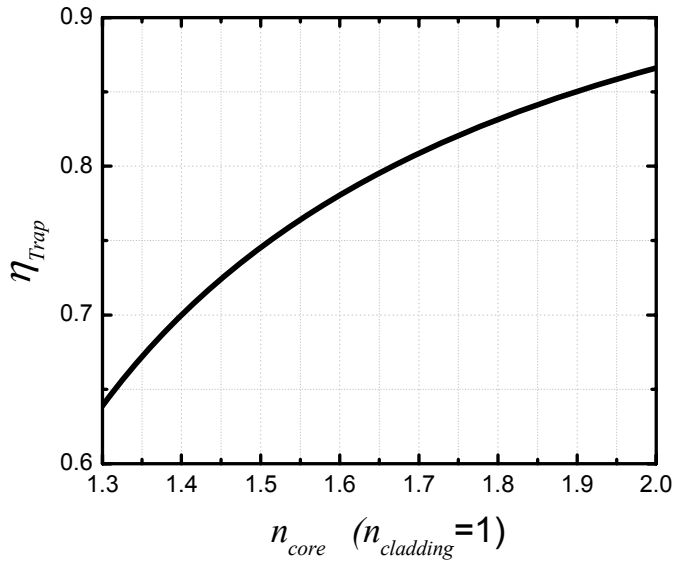

Figure 3.4 Confinement efficiency in a simple air-clad core structure

A high index medium surrounded by low index media will preferentially guide light. For isotropically emitting radiators, the index mismatch between core and cladding should be as high as possible to maximize the confined luminescence fraction.

In OSCs, it is desired to have light guided in the coating-substrate system, which requires an index of refraction matching between coating and substrate. If $n_{coating} > n_{substrate}$, the probability of light trapping in the coating, $\eta_{coating\ guiding}$, can be high:

$$\eta_{coating\ guiding} = \sqrt{1 - \frac{n_{substrate}^{\ 2}}{n_{coating}^{\ 2}}}\,. \tag{17}$$

See Figure 3.5. For light guided in the coating layer, the self transparency requirements are increased by a factor of the ratio of coating to substrate thickness, $t_{substrate}/t_{coating}$. For $t_{substrate} = 1$ mm and $t_{coating} = 1$ μm, this ratio is 10^3, so all coating-guided light is immediately lost.

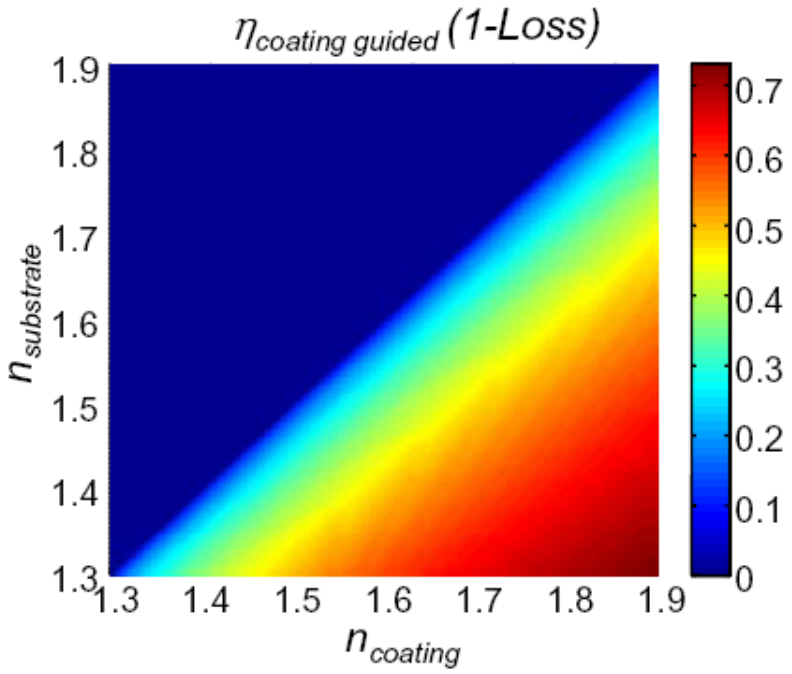

Figure 3.5 Organic trapping efficiency

In an OSC, it is desirable to guide light in the composite substrate-coating system as opposed to only the coating, which exhibits much higher loss, 1-$\eta_{coating\ guiding}$. For a coating of index 1.75 and substrate of 1.5, over 50% of trapped light is trapped in the film and lost for collection.

To decrease trapping losses and coating guiding, the preceding discussion suggests that $n_{substrate}$ should be as high as possible, and $n_{substrate} \geq n_{coating} \geq n_{cladding}$, if possible. In this work, only systems of this type are explored.

Although not explored here, there are two methods one can employ to increase η_{trap}:

1. Like electromagnetic antennas, molecular antennas have directionality. If many microscopic dipoles are isotropically distributed, the macroscopic emission profile will be isotropic. However, for static, aligned emitters, strong

directionality will increase η_{trap},[99] increasing OSC optical quantum efficiency, η_{OQE}.

2. Wavelength dependent omnidirectional reflectors[100] would enable η_{trap} = 100%. For instance, the transmission characteristic of a 19-layer stack of zinc selenide/cryolite films is shown in Figure 3.6b. To increase OSC η_{OQE}, the mirror must be transparent to light coupled into the guide and perfectly reflective for guided light. For example, the mirror shown in Figure 3.6b exhibits transmission below the λ = 600 nm cutoff and complete reflectivity above that wavelength.

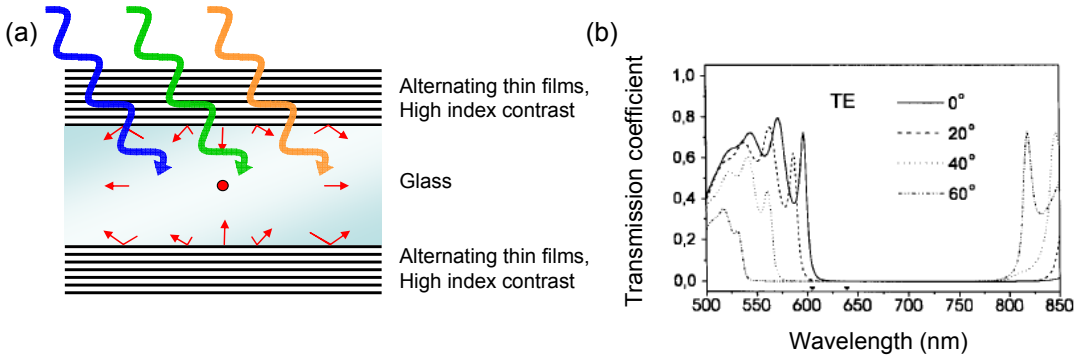

Figure 3.6 Omnidirectional reflectors for OSCs

(A) A schematic implementation of an omnidirectional reflector. **(B)** One of the first examples[101] employed a 19 layer stack of Na_3AlF_6/ZnSe. The materials were chosen for their relatively large index contrast. Note the absence of transmission between λ= 600 and 800 nm. Although this stack is an excellent reflector for emitted light between λ= 600 and 800 nm, its non-unity transmission for light of λ< 600 nm will significantly diminish total collector performance.

3.6 Thermal model

To investigate the thermal performance of OSCs under solar illumination, we investigate a simple heat transfer model here. In conventional single junction solar cell, photons with energy less than the bandgap, E_G, are transmitted though the device and are lost. Photons with energy greater than the bandgap are absorbed and the difference heats the device; see Figure 3.7. By integrating the AM1.5G solar spectrum and assuming perfect charge generation and current collection, we can calculate the maximum possible power and minimum thermal conversion efficiency. These results are shown as a function of bandgap energy in Figure 3.8.

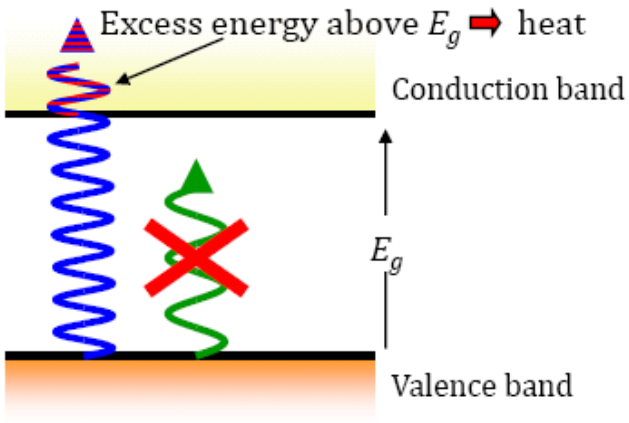

Figure 3.7 Light interaction with a semiconductor

Photons with energies less than E_g are not absorbed and are transmitted through the material. Photons with energies greater than E_g are absorbed but the difference is converted to heat. Although the chromophores considered here do not exhibit band transport, similar thermalization principles apply where the E_g is the energy difference between the lowest unoccupied and highest unoccupied molecular orbitals.

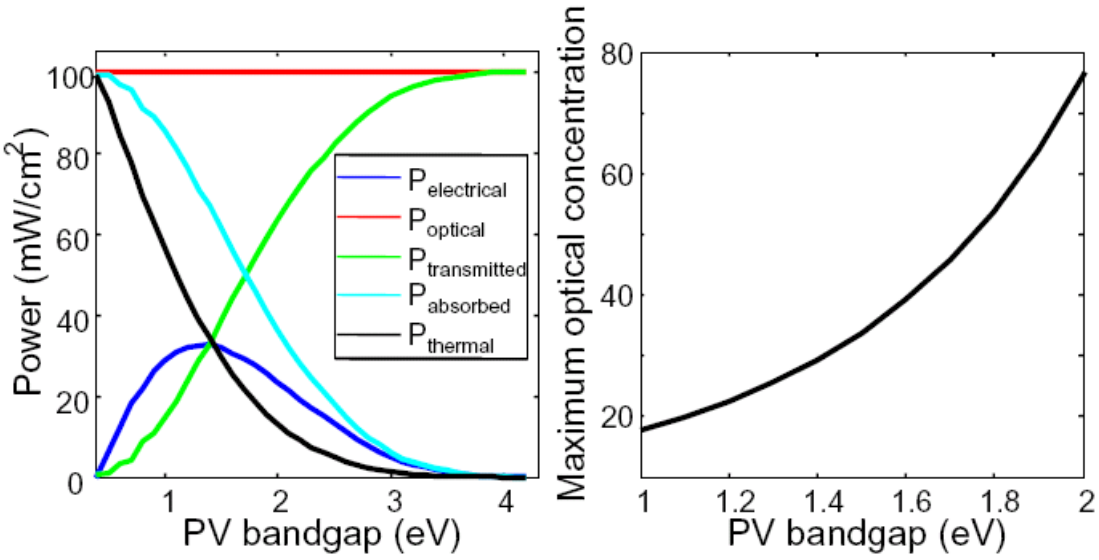

Figure 3.8 Power flow and maximum optical concentration in a single junction solar cell. In **(A)**, perfect electrical energy conversion is assumed (dark blue). Under these conditions, thermal heating is least (black). Light is incident with the power spectrum of the sun (red). The minimum possible thermal load sets the maximum possible optical concentration **(B)** if thermal power sinking is assumed. In practice, the thermal load is higher and maximum concentration limits are lower.

The ratio of the electrical power harvested by the solar cell, $P_{electrical}$, and the incident optical power, $P_{optical}$, is the power conversion efficiency. The shape matches the single junction conversion efficiency limit calculated by Shockley and Queisser,[102] with an optimum bandgap of $\approx$1.3 eV. Transmitted optical power approaches 100% for large E_G, while absorbed power approaches 100% for low E_G. Most single junction solar cells have bandgaps within 0.3 eV of the optimum value.[§] In this range, solar cells must dissipate at least 30-50 mW/cm^2 of thermal power, $P_{thermal}$.

[§] Silicon: 1.12 eV; CdTe: 1.5 eV; CIGS: 1.1 eV; GaAs: 1.4 eV; amorphous Si: 1.6 eV; InP: 1.3 eV[100]

Actual thermal dissipation requirements depend on local solar insolation levels, ambient temperature, and convective wind velocity. However, we can estimate the maximum optical concentration levels using the standard AM1.5G spectra and assume heat dissipation limits. If cell temperature is not adequately controlled, the normalized efficiency degradation is approximately 0.2-0.4%/^{o}C.[103]

The thermal dissipation requirements under non-concentrated illumination are manageable, although it is preferable to operate cells as low temperature as possible. Under optical concentration, the thermal resistance to heat conduction from the cell is highly dependent on cell geometry. Practical (both measured and modeled) concentration limits for linear arrays of single junction solar cells is 10-20 suns equivalent (1-2 W/cm^2).[103-107] This coincides well with the simple model explored here which calculates upper limits; see Figure 3.8b.

The tracking requirements of 1-D linear arrays are relaxed, but Figure 3.8b makes evident that very low concentration limits are possible when constrained by passive cooling. Since OSCs remove excess energy from photons that would otherwise heat the solar cell under direct illumination, the maximum optical concentration levels set by thermal constraints are higher. To investigate this, a simple thermal model is explored for an OSC. The AM1.5G spectrum is completely absorbed by the chromophore layer from $0 < \lambda < \lambda_{abs}$, see Figure 3.9. Photons are emitted with unity efficiency at $\lambda_{emission}$ to be absorbed by the solar cell. All photons are absorbed; as before, the excess energy heats the cell. The total thermal power remained after electrical conversion is calculated as a function of λ_{abs} and $\lambda_{emission}$ for two solar cells of interest, GaInP and GaAs, whose bandgaps are 1.7 eV and 1.4 eV, respectively. The relative amount of thermal energy

removed from each photon incident on the solar cell is $\left(\lambda_{PV}\cdot\left(\lambda_{emission}-\lambda_{abs}\right)/\lambda_{emission}\cdot\left(\lambda_{PV}-\lambda_{abs}\right)\right)$. For typical values of λ_{abs} = 500 nm, $\lambda_{emission}$ = 650 nm, and λ_{PV} = 730 nm, this reduction is 73%.

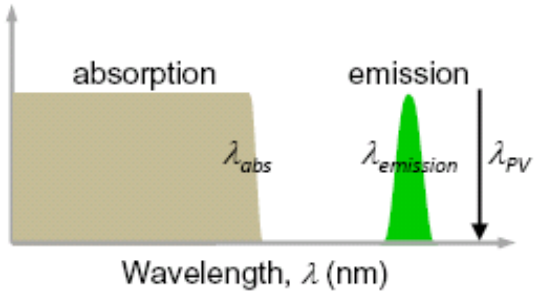

Figure 3.9 Thermal model parameters

In the simple model investigated here, light is collected from $0 < \lambda < \lambda_{abs}$ and emitted at $\lambda_{emission}$ for collection at a solar cell which has unity external quantum efficiency for $\lambda < \lambda_{PV}$.

The results for GaInP are shown in Figure 3.10 and GaAs in Figure 3.11. For all values of λ_{abs} and $\lambda_{emission}$, the thermal power load is 10-100 times lower than the direct illumination case, indicating that the thermally set maximal concentration levels are approximately 100 times higher. The plots are overlaid with contours to illustrate λ_{abs} and $\lambda_{emission}$ values that result in concentration levels of 200, 400, 600, and 900 times solar irradiance. These levels represent upper bounds since the model is simplistic. Since the since the model predicts (within a factor of two) the direct illumination concentration limit, the relative difference should be valid. Practically, the concentration limits set by self-absorption will limit optical concentration before thermal dissipation requirements

become an issue. These results also indicate that simple, passive mounting on metal strips are adequate thermal sinks for all concentration levels of interest.[103]

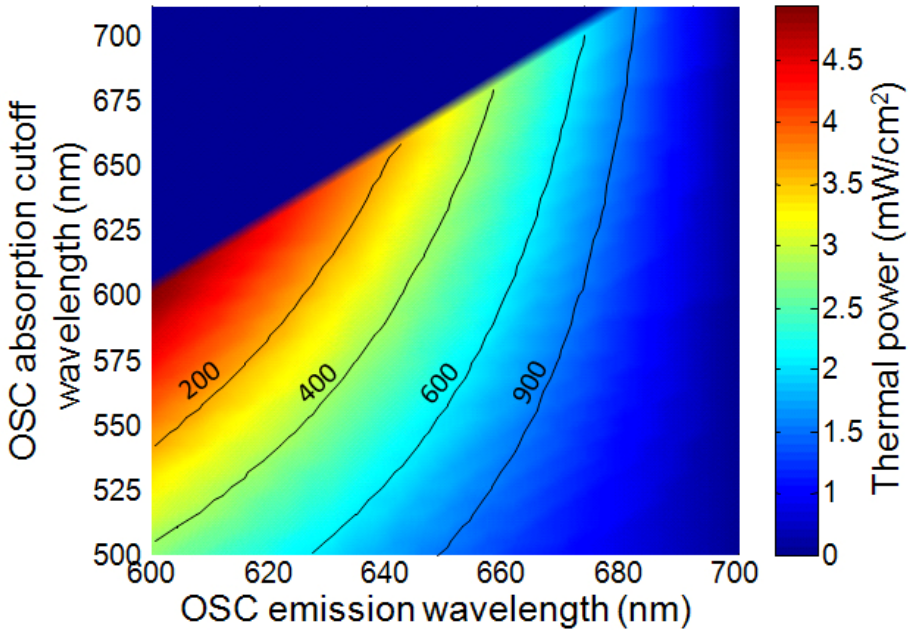

Figure 3.10 Thermal power loads and concentration limits for an OSC coupled to a GaInP PV

Thermal load increase as emission wavelength decrease (photon energy increases) and as OSC absorption cutoff wavelength increases (increasing collected photon number). Since the emission wavelength is constrained to be greater than the absorption cutoff wavelength, the upper left region is blank. Assuming a thermal power dissipation limit for a linear PV array of 1 W/cm^2, contours of maximum concentration are overlaid that are two orders of magnitude higher than direct incidence without wavelength conversion.

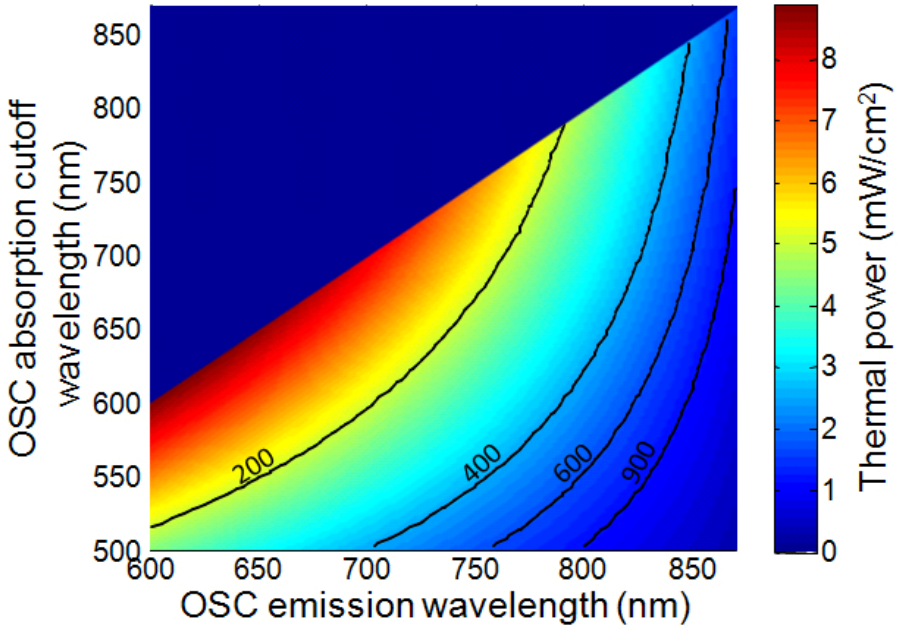

Figure 3.11 Thermal power loads and concentration limits for an OSC coupled to a GaAs PV

Thermal loads are similar in shape but higher in magnitude for GaAs cells compared to GaInP (Figure 3.10). To reach similar optical concentration, light emission must be pushed towards the infrared.

3.7 Dye stability

Photovoltaic modules have typical lifetimes of 20-30 years. OSCs must exhibit excellent stability to be commercially viable. The most likely candidate for failure is the organic dye, which will typically fail through loss of photoluminescence yield, then photo-bleaching (loss of absorption). The German chemical company BASF has developed a class of fluorescent concentrator dyes designed for very long lifetimes based on perylene derivatives. These dyes have been investigated by the ECN in the Netherlands and un-encapsulated dyes cast in polymethyl methacrylate and variants have been measured with system lifetimes of roughly four years.[108,109] Besides photostability, the dyes must be

chemically nonreactive with any stabilizers, fire retardants, and any other additives mixed in with the polymer sheets.

The organic dye molecules we investigate in this study were originally developed for organic light emitting diodes (OLEDs). Since the original fluorescent concentrator studies there has been significant investment in the research and development of OLEDs, resulting in devices that exhibit half-lives exceeding 300,000 hours, or thirty years.[110] Progress in OLED stability has been achieved through advances in dye molecule design and packaging. Both of these technologies are directly applicable to OSCs. Indeed, in this work we employ two dyes 4-(dicyanomethylene)-2-*t*-*butyl*-6-(1,1,7,7-tetramethyljulolidyl-9-enyl)-4*H*-pyran[111] (DCJTB) and platinum tetraphenyltetrabenzoporphyrin[112] (Pt(TPBP)) which have exhibited stabilities exceeding 1,000,000 and 100,000 hours in OLEDs, respectively.[113,114] Since they are thermally deposited onto glass, they do not interact with the substrate. We also note that OLED device stability requirements are more stringent. In OLEDs, electrical current is passed through the molecules and the films can reach high concentrations of triplet species which are highly reactive with oxygen. The quoted lifetimes were measured in systems packaged with steel backing, attached by epoxy. The failure modes of material utilized in OSCs must be evaluated carefully. External light filtering to remove especially harmful light is possible, although device efficiency will be sacrificed.

3.8 Thin film organic optoelectonics for OSCs

Fluorescent concentrators were initially proposed in 1976,[90] but demonstrations of high power conversion efficiencies has been especially frustrated by high self-absorption losses. Recent advances in organic optoelectronics gained in the development of organic semiconductor light emitting devices are directly applicable to OSCs. We discuss the relevant physical processes and their benefits in the Sections 3.8.1-3.8.3 .

3.8.1 Förster energy transfer

Förster recognized in 1959 that direct long range energy transfer could occur between two molecules if the emission spectrum of the donor molecule overlaps the absorption spectrum of the acceptor molecule.[96] This energy transfer couples the transition dipoles of neighboring molecules, can operate on the length scale of several nanometers, and occurs without the emission of a photon into the far field. Where strong overlap occurs, this process dominates others and will occur before radiative recombination and far field light emission.

The energy transfer process can be used to enhance the wavelength shift between self absorption and emission. In particular, Förster energy transfer, which couples the transition dipoles of neighboring molecules, can be exploited to couple a dye with short wavelength absorption to a dye with longer wavelength absorption. This process is schematically illustrated in Figure 3.12. Energy transfer that occurs without photon emission offers several advantages:

1. The waveguide must be transparent to emitted light to reduce self-absorption losses. Reducing the dye concentration is a simple way to do this, but absorption is lost. Energy transfer allows high concentrations of absorbers to be used with lower concentrations of emitters. The increased self-transparency will reduce transport losses and enable higher optical concentrations at the waveguide edges.
2. The strict requirements of high photoluminescence efficiency, η_{PL}, can be moved to the terminal emitter. Each emission process incurs with it additional losses associated with non-unity η_{PL}. Since energy transfer effectively competes with non-radiative recombination, low η_{PL} dye materials can be used to optically pump the emitting material with high efficiency.
3. Each emission event carries with it potential losses up to 1-η_{trap}. Removal of non-essential emission is preferred.
4. As dyes degrade in performance, η_{PL} typically precedes photo-bleaching; strict stability requirements can be eased for donor molecules.

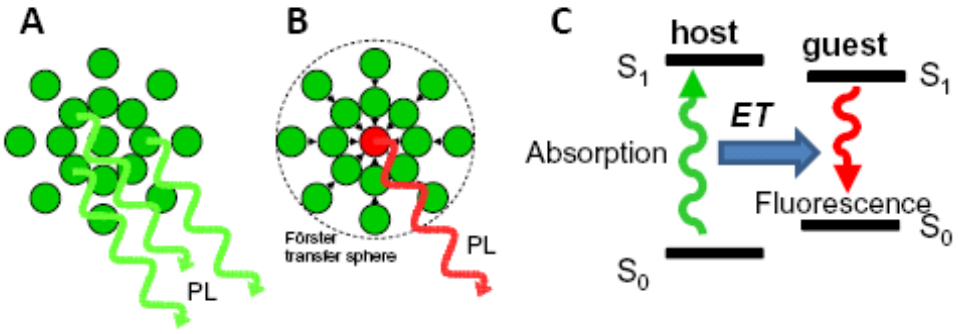

Figure 3.12 Spatial and energetic representation of Förster energy transfer

(A) In a pure film, absorption and emission of light is performed by the same molecular species. **(B,C)** When a second, lower energy dye is added, the host material can transfer energy to it *without emission of a photon*, introducing a substantial energy shift between absorption and emission. Near field energy transfer effectively competes with direct radiative recombination within the Forster transfer sphere.

Figure 3.12 suggests two ways in which energy transfer is possible. Since near field energy transfer requires intermolecular distances of several nanometers, these can be controlled through either physical linkages or high packing density. We employ thin, homogenous coatings to control dye spacing though film composition control.

3.8.2 Solid state solvation

The excited state of many organic dyes is highly polar. If such dyes are surrounded by a polar dielectric that stabilizes the excited state, the emission of the dye may be red-shifted. The Stokes shift will increase if the excited state is more polar than the ground state. This energy shift will similarly reduce the overlap between absorption and

emission, increasing the light transport efficiency. This effect is employed in organic light emitting diodes to adjust emission color.[97]

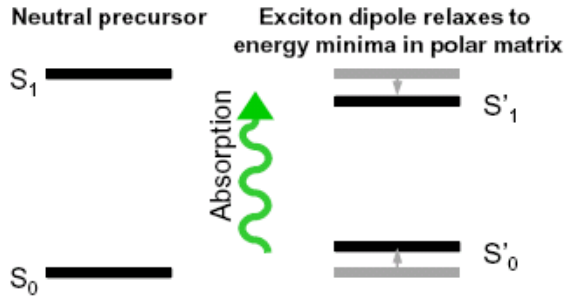

Figure 3.13 Energy level representation of solid state solvation

Although a stable charge dipole may exist in the neutral ground state due to non uniform electron density on a molecule, the charge separation that occurs after light absorption will typically increase its magnitude. If surrounded by a polar host matrix, additional nuclear or vibrational relaxation may occur to achieve a lowest energy state. This additional energy relaxation will result in emission that is red-shifted compared to the non polar host matrix case. The shift may increase dye self transparency.

3.8.3 Phosphorescence

The absorption of a photon by a dye molecule promotes an electron from the highest occupied molecular orbital (HOMO) to the lowest unoccupied molecular orbital (LUMO). Considering only the electrons in these frontier molecular orbitals, the excited state, or exciton, may be simplified to a two-electron system. Consequently, it may take one of four possible spin states: three “triplet” states with total spin 1, and one “singlet” state with total spin 0. For fluorescent molecules, only the singlet exciton state has a strongly allowed radiative transition to the ground state.

The exchange energy separating the fluorescent singlet state from the triplet is typically 0.7 eV. Because many excitons are generated in the triplet state in organic light emitting devices,[98,115] there has been much effort recently directed at the synthesis of efficient triplet emitters. Such dyes are known as organic phosphors, because the emission is typically only weakly allowed and therefore somewhat slower than fluorescence. The advantage of phosphors in OSCs is that the triplet state is only weakly absorptive, so they typically exhibit huge Stokes shifts and weak self absorption; see Figure 3.14.

.

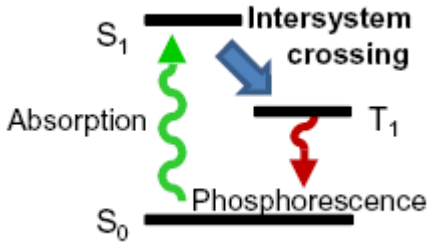

Figure 3.14 Phosphorescence

The energy level difference between excited singlet and triplet excitons arises from the exchange energy. This energy reduction shifts emission further to the red, increasing dye self transparency.

An example of the benefit of phosphorescence in reducing self absorption is shown in Figure 3.15. Here we first show the absorption and fluorescence of the classic fluorescent laser dye coumarin6 (C6).[116] It is then compared to a synthetic variant that couples the dye with the heavy metal atom Ir. Spin orbit coupling induced by the presence of Ir enhances phosphorescence from C6 without noticeably altering the absorption spectrum. The phosphorescent variant has substantially lower self-absorption.

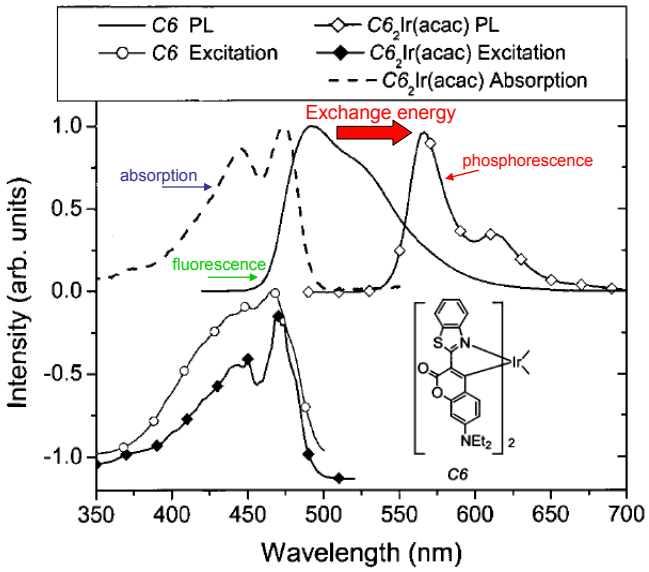

Figure 3.15 Phosphorescence to increase dye self-transparency

The heavy metal effect on the classic laser dye C6. Note the dramatic decrease in self-absorption. From Lamansky, *et al*.[116]

Organic phosphors offer a number of benefits:

1. Spin orbit coupling of heavy metal atoms, such as Pt and Ir, leads to short phosphorescent lifetimes (< 100 μs) and high phosphorescence efficiencies, enhancing photostability.
2. The large exchange energies in organic phosphors enable strong, narrow emission at near infrared wavelengths, leading to broadband spectral collection across the visible wavelengths.
3. Direct excitation of triplet states are undesirable, or self transparency will be compromised. Some organic phosphors exhibit weak triplet absorption coefficients, allowing high optical concentration.

4. Its desirable to utilize films with high chromophore loading, but low intermolecular spacing often leads to concentration quenching. Many phosphorescent compounds show marked self quenching at doping levels of 10% and higher, enabling optically dense thin films.

3.9 Device architectures

OSCs utilizing the above design elements were explored in several device architectures. In its simplest format, a single high refractive index waveguide is coated with micron-thick films of co-deposited organic materials. A silver mirror is placed behind the OSC, separated by an air gap; see Figure 3.16a. To obtain the highest power conversion efficiencies we construct tandem OSCs.[89] Incident solar radiation first encounters an OSC employing a short wavelength dye. Longer wavelengths are transmitted through the first OSC and absorbed by a longer wavelength dye in a second OSC (Figure 3.16b). Stacked solar cells allow more electrical power to be extracted from each photon compared to the single junction case.[117] However, the technical constraints of current matching, lattice matching, spectral fluctuations, and the requirement of additional tunnel junctions complicate the manufacturing and design of multijunction solar cells.[118] In comparison, the integration of two or more OSCs avoids these constraints. The bandgaps of the solar cells coupled to each of the OSCs are chosen such that absorption of guided radiation is complete, yet the energy shift is low to increase conversion efficiency and minimize heating.

A third configuration is possible whereupon the solar radiation transmitted through the top OSC can be gathered by a bottom PV cell (Figure 3.16c) or used to heat

water in a hybrid PV thermal system.[89] In this configuration, the OSC operates to improve the efficiency of an existing thin film PV system, potentially reducing total system cost.

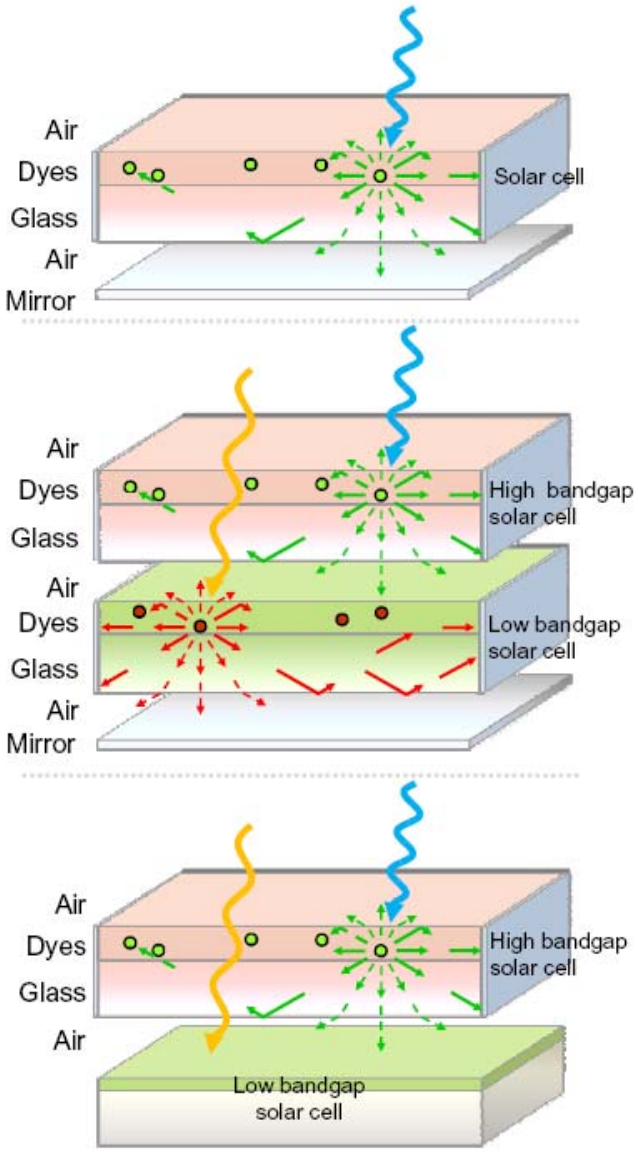

Figure 3.16 Physical configuration of Organic Solar Concentrators (OSCs)
(A) OSCs consist of a thin film of organic dyes deposited on high refractive index glass substrates. The dyes absorb incident solar radiation and re-emit it at a lower energy. Approximately 80% of the re-emitted photons are trapped within the waveguide by total internal reflection for ultimate collection by a PV device mounted on the substrate edges. Photon loss (dashed lines) occurs via non-trapped emission or absorption by other dyes. **(B)** Light transmitted through the first OSC can be captured and collected by a second OSC whose dyes absorb and emit light at lower energies for electrical conversion at a second, lower bandgap PV device. Confinement losses in the top OSC can be reduced if downward emitted light is collected in the bottom OSC. In each case, a mirror placed at the bottom of the stack increases absorption by allowing a second pass through the OSC. **(C)** The bottom OSC can be replaced by a low cost PV cell or used to heat water in a hybrid PV thermal system. All three configurations are explored in this work.

3.10 Materials for OSCs

Chromophore self transparency is the primary loss factor preventing high optical concentration in OSCs. Thin films of several microns absorb incoming radiation in the vertical dimension, but horizontal guided transport must occur over length scales of tens of centimeters. This sets steep requirements for very low overlap between absorption and emission spectra.

We quantify self absorption losses using the self absorption ratio, *S*, between the peak absorption of a given material and its absorption at its emissive wavelength. Previously, Batchelder and Zewail evaluated the spectral properties of 18 laser dyes for suitability for fluorescent concentrators.[93,94] They found DCM (4-dicyanomethylene-2-methyl-6-(p-dimethylaminostyryl)-4*H*-pyran) to have the highest photoluminescence efficiency and best spectral characteristics, with a Stokes shift of 150 nm, corresponding to $S = 25$; see Figure 3.17. When doped into polymethyl methacrylate planar guides in the device structure shown in Figure 3.2, they measured power conversion efficiencies of 1.3% at optical concentration levels of $G = 68$.

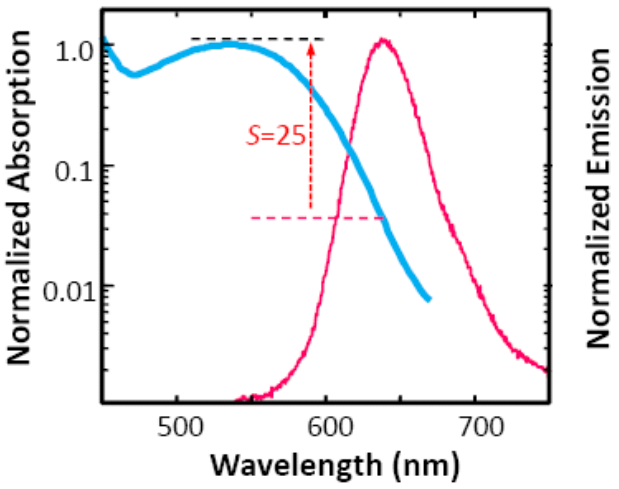

Figure 3.17 Optical absorption and emission spectra of DCM

The high photoluminescence efficiency of DCM made it an attractive candidate material for fluorescent collectors, despite its large overlap between absorption and emission, with a self absorption ratio of *S*=25.

We implemented Förster energy transfer to improve the performance of Zewail's DCM-based concentrator. In the new low-self absorption concentrator, DCM is employed in much lower concentrations. Optical absorption is instead performed by two common OLED materials, tris(8-hydroxyquinoline) aluminum (AlQ_3) and rubrene. Both materials are fluorescent at high concentrations and are therefore capable of energy transfer to a low density of DCM. Because Förster energy transfer is a short range (~3-4 nm) interaction, all the dyes are co-evaporated in a thin film. Earlier concentrators were made by diffusing dyes within a polymer substrate.[93,94] However, the low dye density in such devices precludes the use of Förster transfer to minimize self absorption. In this work, we study several new dyes, including DCJTB (4-(dicyanomethylene)-2-*t-butyl*-6-(1,1,7,7-tetramethyljulolidyl-9-enyl)-4*H*-pyran), a modern variant of DCM.

To control the concentration of DCJTB, it was co-deposited with the host material tris(8-hydroxyquinoline) aluminum (AlQ_3), which forms stable amorphous films.[119] The self absorption ratio is enhanced when AlQ_3 is used as the host, because both AlQ_3 and DCJTB are polar molecules. The polar environment red-shifts the DCJTB photoluminescence (PL) via the solid state solvation effect, which is employed in OLEDs to adjust the emission color.[97]

Förster energy transfer is used to reduce the required concentration, and hence the self absorption of the emissive dye. For example, in the rubrene-based OSC of Figure 3.18a, we employ rubrene and DCJTB in a 30:1 ratio. Förster energy transfer from rubrene to DCJTB increases the self absorption ratio of the rubrene-based OSC relative to the DCJTB-based OSC. Rubrene is non polar, however, and together with a slight reduction in the DCJTB concentration, this causes the DCJTB PL to shift approximately 20 nm back towards the blue. We also build OSCs using Pt(II)-tetraphenyltetrabenzoporphyrin (Pt(TPBP)), which is phosphorescent in the infrared at $\lambda = 770$ nm with a PL efficiency of approximately 50%. It emits from a weakly-allowed triplet state relaxation. Compared to conventional fluorescent dyes, an advantage of phosphorescent dyes is that the emissive state is only weakly absorptive. Thus, phosphors typically exhibit large Stokes shifts, eliminating the need for Förster transfer to a longer wavelength terminal dye. Indeed, the self absorption ratio for the Pt(TPBP)-based OSC is approximately $S = 500$; see Figure 3.18b. To fill the gap in the Pt(TPBP) absorption spectrum between the Soret band at $\lambda = 430$ nm and the Q band at $\lambda = 611$ nm, we add DCJTB, which efficiently transfers energy to Pt(TPBP).

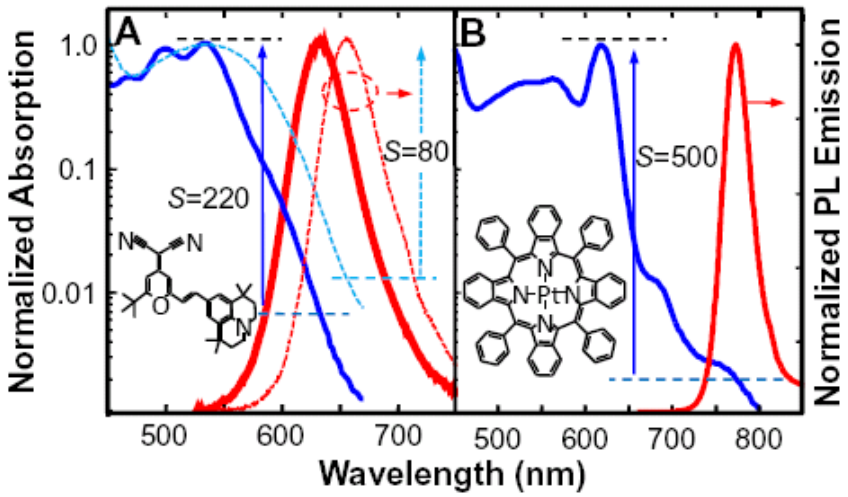

Figure 3.18 Normalized absorption and emission spectra of OSC films

(A) The ratio between the peak absorption coefficient and the absorption coefficient at the emission wavelength provides a measure of the self absorption in an OSC film. The self absorption ratio in a DCJTB-based OSC is $S = 80$ (dotted lines). A larger self absorption ratio of $S = 220$ is obtained in a rubrene-based OSC (solid lines). The self absorption ratio increases because the amount of DCJTB is reduced by a factor of three. Its absorption is replaced by rubrene, which then transfers energy to DCJTB. Inset: DCJTB chemical structure. **(B)** Phosphorescence is another method to reduce self-absorption. The self absorption ratio in a Pt(TPBP)-based OSC is $S = 500$. Inset: Pt(TPBP) chemical structure.

Organic solar concentrators (OSCs) were fabricated using vacuum ($< 3 \times 10^{-6}$ Torr) thermal evaporation. Film thickness and deposition rates were controlled using quartz crystal monitors. The DCJTB-based OSC is a 5.7-μm-thick film of 2% DCJTB in AlQ_3. The rubrene-based OSC is a 1.6-μm-thick film of 30% rubrene and 1.0% DCJTB in AlQ_3. The Pt(TPBP)-based OSC is a 5.9-μm-thick film of 2% DCJTB and 4% Pt(TPBP) in AlQ_3. The rubrene, DCJTB and Pt(TPBP) concentrations within AlQ_3 were chosen to minimize concentration quenching of their photoluminescent efficiencies.[120]

The thickness of each OSC was adjusted to obtain the desired optical absorption. The absorption spectra were measured with an Aquila spectrophotometer.

3.11 Optical quantum efficiency spectra

The optical quantum efficiency (OQE), defined as the fraction of incident photons emitted from the edges of the OSC substrates, was determined within an integrating sphere. Devices were fabricated on glass with refractive index $n = 1.82$. We distinguish between edge and facial emission by selectively blocking edge emission from some samples using black tape and permanent black marker. The excitation source for all experiments was a Xenon lamp coupled into a monochromator and chopped at 90 Hz, yielding an optical intensity at the sample of approximately 5 mW/cm^2. All OSCs were backed by a silvered mirror separated by an air gap. The tandem OSC was backed by a single mirror behind the bottom collector. Photoluminescence was detected synchronously using a calibrated Si photodetector mounted directly on an integrating sphere.

The ratio of the area of the concentrator to the area of the PV cell is the geometric gain, G, also known as the geometric concentration factor. The OQEs of the single waveguide OSCs at low geometric gain ($G = 3$) are compared in Figure 3.19a. For the two dye fluorescent system (red), AlQ_3 absorbs and DCJTB both absorbs and emits. In the three dye fluorescent system (blue), the absorption function of DCJTB is replaced by rubrene, lowering the self absorption but also reducing the spectral bandwidth. For the phosphorescent system (green), AlQ_3 and DCJTB absorb and PtTPTBP both absorbs and emits.

A tandem waveguide OSC was constructed using the rubrene-based OSC on top to collect blue and green light and the Pt(TPBP)-based OSC on the bottom to collect red light. Together, this tandem OSC combines higher efficiency collection in the blue and green with lower efficiency performance further into the red, as shown in Figure 3.19b.

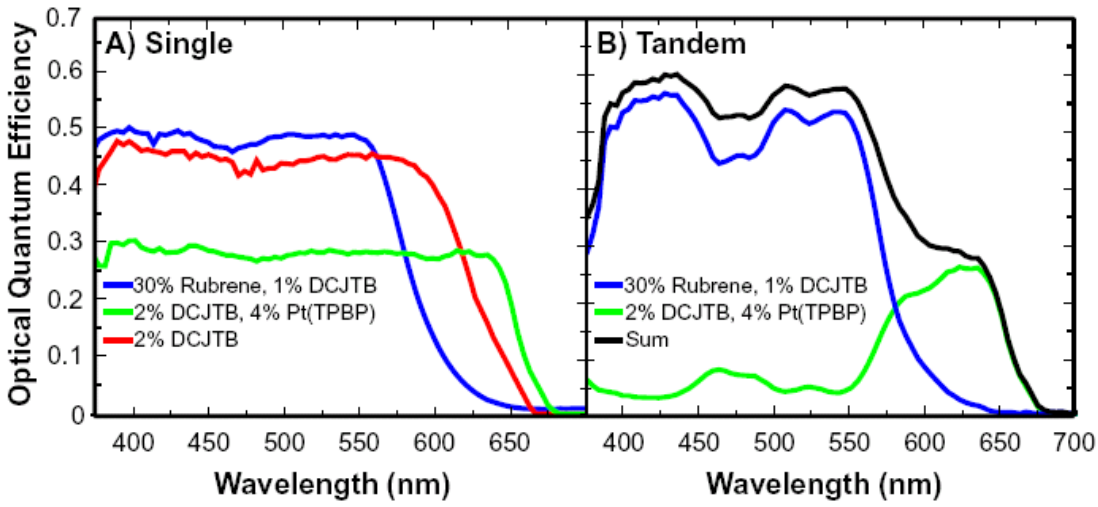

Figure 3.19 Optical quantum efficiency (OQE) spectra at a geometric gain of $G = 3$.
The OQE is the fraction of incident photons that are emitted from the edges of the substrate. In **(A)** we plot the OQE spectra of the DCJTB, rubrene and Pt(TPBP)-based single waveguide OSCs. The DCJTB-based OSC is a 5.7-μm-thick film of 2% DCJTB in AlQ_3. The rubrene-based OSC is a 1.6-μm-thick film of 30% rubrene and 1% DCJTB in AlQ_3. The Pt(TPBP)-based OSC is a 5.9-μm-thick film of 2% DCJTB and 4% Pt(TPBP) in AlQ_3. **(B)** In the tandem configuration light is incident first on the rubrene-based OSC (blue). This filters the incident light incident on the second, mirror-backed, Pt(TPBP)-based OSC (green). The composite OQE is shown in black.

Power conversion efficiencies were obtained by integrating the product of the OQE, AM1.5G spectrum, and solar cell external quantum efficiency. OSCs with emission from DCJTB are paired with GaInP solar cells;[121] those with emission from Pt(TPBP) are paired with GaAs.[122] We assume ideal optical coupling to an attached solar

cell. We also consider the use of CdTe or Cu(In,Ga)Se_2 solar cells to absorb the long wavelength radiation transmitted through a rubrene-based OSC. Table 3.1 summarizes the PV quantum efficiency (η_Q), open circuit voltage (V_{OC}), fill factor (FF), PV power conversion efficiency (η_{PV}) of each solar cell. The power efficiencies of tandem OSCs were calculated by filtering the AM1.5G spectrum with the direct transmission function of the top OSC. We confirmed that facial emission is evenly distributed between the top and bottom face by collecting facial photoluminescence with a Si detector. Light emitted through the bottom face of the top OSC can be absorbed by the bottom OSC; these incident photons are included in the tandem power conversion efficiency calculation.

The DCJTB-rubrene-AlQ3 OSC has $\eta_{PCE} = 5.5\%$, while for DCJTB in AlQ3 alone , $\eta_{PCE} = 5.9\%$. The efficiency of the tandem OSC peaks at 6.8%. We also calculate the power efficiency of tandem systems consisting of a top rubrene-based OSC whose transmission is incident on a CdTe or Cu(In,Ga)Se_2 (CIGS) PV cell.[123,124] The OSC is predicted to increase the efficiency of in-production CdTe and CIGS cells from 9.6% and 13.1% to 11.9% and 14.5%, respectively; see Figure 3.20.

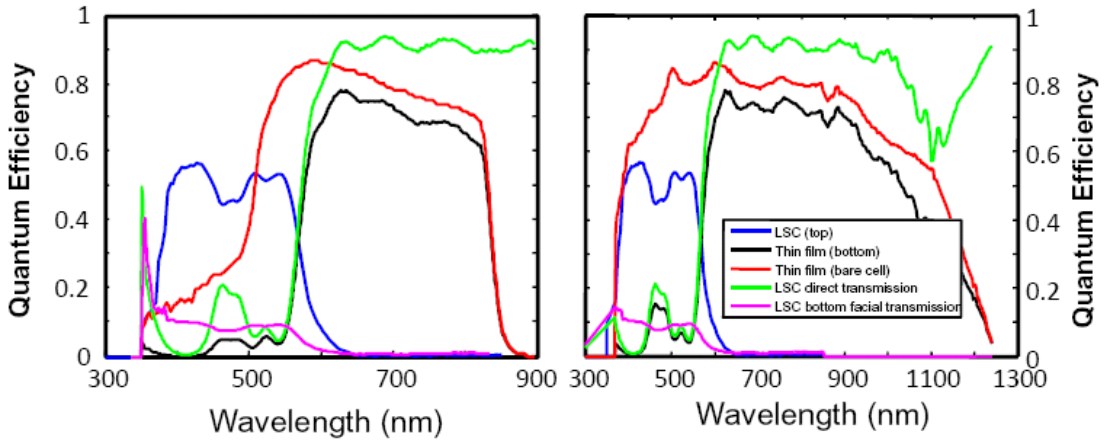

Figure 3.20 Hybrid OSC thin film PV system quantum efficiency

In-production thin film topped with the rubrene based OSC (OQE in blue) described in this work show increased power conversion efficiency compared to the direct illumination case. Direct incidence is filtered by the transmission function of the OSC (green), reducing its effective external quantum efficiency (from red to black). The performance increase is larger for the cadmium telluride cell since it suffers from poor performance at blue wavelengths.

PV	η_Q	V_{OC}	FF	η_{PV}(%)	Reference
GaInP	0.83	1.34	0.83	18.1	[121]
GaAs	0.91	1.02	0.87	25.1	[122]
CdTe	0.83	0.79	0.62	9.6	[123]
$Cu(In,Ga)Se_2$	0.82	0.59	0.67	13.1	[124]

Table 3.1 Inorganic solar cell parameters

The electrical performance of the solar cells used in the OSC power conversion efficiency calculations. GaInP and GaAs solar cells were used because their absorption cutoff is closely matched to the emission spectrum of the OSC terminal emitters. The CdTe and $Cu(In,Ga)Se_2$ thin film PVs used in modeling the OSC-thin film tandem devices are commercially available.

3.12 Performance versus optical concentration

The external quantum efficiency (EQE) is the number of harvested electrons per incident photon and includes the coupling losses at the PV interface and the quantum efficiency of the PV. EQE was measured as a function of geometric gain, G, at $\lambda = 534$ nm for the fluorescent devices and $\lambda = 620$ nm for the phosphorescent devices. OSCs used in the external quantum efficiency measurements were fabricated on glass with refractive index $n = 1.72$. The current was measured with an attached, 125 mm × 8 mm PV cell manufactured by Sunpower with $\eta_Q > 0.85$. The OSC was excited at normal incidence along a line bisecting the glass substrate and perpendicular to the attached PV cell. The measured photocurrent was then corrected for the solid angle to determine the external quantum efficiency as a function of G. The correction factor, g, as a function of distance, d, from the PV is derived from geometrical considerations:

$$g = \pi / \tan^{-1}\left(L/2d\right) \tag{18}$$

where L is the length of the OSC substrate.

To compare the measured external quantum efficiency (EQE) data to theory, we follow the treatment of Batchelder, *et al*. [94]:

$$\eta_{EQE} = \eta_Q \cdot \eta_{abs} \frac{\eta_{PL} \cdot \eta_{trap}\left(1-r\right)}{1 - r \cdot \eta_{PL} \cdot \eta_{trap}} \tag{19}$$

where r is the average probability that an emitted photon will be reabsorbed, η_{abs} is the fraction of incident photons that are absorbed, η_{PL} is the photoluminescent yield of the OSC, and η_{trap} is the OSC trapping efficiency. Under the condition of isotropically oriented emitters in the organic layer, the efficiency of waveguide trapping is

$$\eta_{trap} = \sqrt{1 - \frac{n_{clad}^{\ 2}}{n_{core}^{\ 2}}} \tag{20}$$

where the waveguide core and cladding refractive indices are n_{core} and n_{clad}, respectively. For air cladding and an organic thin film refractive index of $n_{core} = 1.7$, $\eta_{trap} \approx 80\%$. The only variable in Equation (19) that varies with geometric gain is r. We use a simplified calculation for r that accounts for the square geometry of our samples and uses the self-absorption ratio outlined in the text. The self-absorption probability, r, is a function of the overlap between the normalized emission spectrum of the dye $f(\lambda)$ and the absorption coefficient of the dye $\alpha(\lambda)$. The absorption coefficient must be scaled by the concentration of the dye within the waveguide. We express the concentration as the effective thickness of the dye layer, t, divided by the total thickness of the waveguide, t_0, which is assumed to be index-matched to the dye layer. For a dye molecule in the center of a square OSC with length L, the self absorption probability is given by

$$r = \frac{\int_0^{\infty} d\lambda \int_{\theta_{crit}}^{\pi/2} \sin\theta d\theta \int_{-\pi/4}^{\pi/4} d\phi f(\lambda)\left(1 - \exp\left[-\alpha(\lambda)\frac{t}{t_0}\frac{L}{2}\Big/\sin\theta\cos\phi\right]\right)}{\int_0^{\infty} d\lambda \int_{\theta_{crit}}^{\pi/2} \sin\theta d\theta \int_{-\pi/4}^{\pi/4} d\phi f(\lambda)} \tag{21}$$

where θ is the azimuth defined relative to the normal of the OSC plane, ϕ is the zenith coordinate, and $\theta_{crit} = \sin^{-1}\left(n_{clad}/n_{core}\right)$ is the total internal reflection cutoff. Noting that $G = L/4t_0$, yields

$$r = \frac{\int_0^{\infty} d\lambda \int_{\theta_{crit}}^{\pi/2} \sin\theta d\theta \int_{-\pi/4}^{\pi/4} d\phi f(\lambda)\left(1 - \exp\left[-2\alpha(\lambda)tG/\sin\theta\cos\phi\right]\right)}{\int_0^{\infty} d\lambda \int_{\theta_{crit}}^{\pi/2} \sin\theta d\theta \int_{-\pi/4}^{\pi/4} d\phi f(\lambda)} \tag{22}$$

Next, we approximate the emission spectrum by a single wavelength

$$f(\lambda) = \delta(\lambda - \lambda_{PL}) \tag{23}$$

which yields

$$r = 1 - \frac{\int_{\theta_{crit}}^{\pi/2} \sin\theta d\theta \int_{-\pi/4}^{\pi/4} d\phi \exp\left[-2AG\log 10/S\sin\theta\cos\phi\right]}{\frac{\pi}{2}\cos\theta_{crit}} \tag{24}$$

where A is the single pass peak absorbance of the OSC. The self absorption ratio is $S = \alpha_{max}/\alpha_{PL}$, where α_{max} is the absorption coefficient at the peak absorption wavelength, and α_{PL} is the absorption coefficient at the emission wavelength λ_{PL}. Equation (24) is most accurate for low self absorption since it does not model the progressive red shift in the waveguided light due to self absorption. Many OSCs, however, will likely operate with only weak self absorption. Under this condition, Equation (24) provides a convenient design tool since it expresses self absorption losses in terms of the macroscopic OSC specifications G, S and A. More accurate models are also available; see References 94,125-127.

We used Equation (24) to model the G dependence of the DCJTB, rubrene and Pt(TPBP)-based OSCs in Figure 3.21a of the text with the parameters listed in Table 2. The quantum efficiency of the Sunpower Si solar cell including coupling losses was measured to be $\eta_Q = 0.85$. The trapping efficiency was measured in the integrating sphere by distinguishing between facial and edge emission using black tape and permanent marker to blacken the substrate edges. The measured trapping efficiency was consistently lower than predicted by Equation (20), suggesting that photon re-emission within the OSC is not isotropic. The self absorption ratio was used as a fit parameter and compared to the data in Figure 3.18 of the text. Overall the agreement is very good given the assumption of monochromatic emission in Equation (23).

OSC	η_{abs}	η_{PL}	η_{trap}	S (fit)	S (measured)
DCJTB	0.88	0.71	0.68	150	80
rubrene	0.90	0.77	0.73	250	220
Pt(TPBP)	0.92	0.46	0.72	1500	500

Table 3.2 Theoretical model fit parameters

To compare measured EQE to theory, Eqns (19) and (24) were solved using these input parameters. The quantum efficiency of the Sunpower cell including the coupling loss was taken to be $\eta_Q = 0.85$.

Figure 3.21a shows the dependence of the EQE with G for each of the films, measured at $\lambda = 534$ nm for the fluorescent systems, and $\lambda = 620$ nm for the

phosphorescent system. The DCJTB-based OSC shows the strongest self absorption. The self absorption is lower in the rubrene-based OSC, consistent with the spectroscopic data in Figure 3.18a. The results are summarized in Table 3.3.

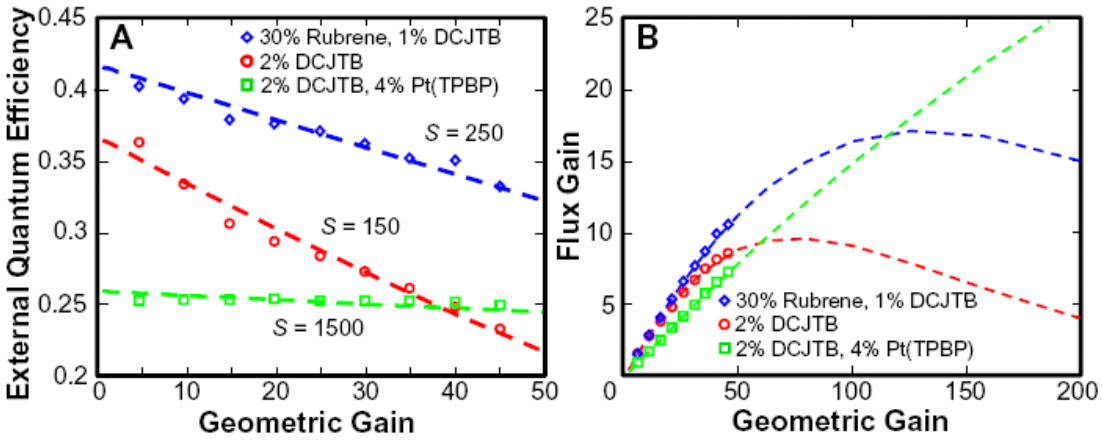

Figure 3.21 OSC efficiency and flux gain as a function of geometric gain

(A) With increasing G, photons must take a longer path to the edge-attached PV, increasing the probability of self-absorption losses. The fit lines are theoretical fits using S as in input parameter. **(B)** The flux gain increases with G, but reaches a maximum when the benefit of additional G is cancelled by self absorption losses. Near field energy transfer and phosphorescence substantially improve the flux gain relative to the DCJTB-based OSC.

The Pt(TPBP)-based OSC shows no observable self absorption loss for $G < 50$. The data matches the theoretical performance[93,94] assuming self absorption ratios of $S = 150$, $S = 250$ and $S = 1500$, for DCJTB, rubrene and Pt(TPBP)-based OSCs, respectively.

OSC	Power conversion efficiency at $G = 3$, 50	Flux gain at $G = 50$	Projected maximum flux gain
DCJTB	5.9%, 4.0%	9	12 ± 2 at $G = 80$
rubrene	5.5%, 4.7%	11	17 ± 2 at $G = 125$
Pt(TPBP)	4.1%, 4.1%	7	46 ± 15 at $G = 630$
Tandem OSC	6.8%, 6.1%	-	-
Tandem OSC-CdTe PV	11.9%, 11.1%	11	17 at $G = 125$
Tandem OSC-CIGS PV	14.5%, 13.8%	11	17 at $G = 125$

Table 3.3 Performance of OSCs

The rubrene and Pt(TPBP)-based OSCs demonstrate the best preservation of power efficiency at high *G*. Their benefits are combined in the Tandem OSC. The highest efficiencies are obtained from combinations of the rubrene-based OSC with CdTe or CIGS PV cells. The baseline efficiencies of the production CdTe and CIGS cells are 9.6% and 13.1%, respectively.[123,124]

3.13 Biological OSCs

Naturally occurring photosynthetic antennas possess many favorable characteristics for OSC collector materials. Over two billion years of evolutionary adaptation have optimized the functionality of these antennas:

1. They position dense chromophore arrays in proteinaceous scaffolds with sub-nanometer precision, controlling both relative concentrations and orientations. As a result, they can exhibit broad spectral harvesting and high efficiency energy transfer efficiencies. Compared to the amorphous films describe in the work above, photosynthetic antennas are well designed molecular machinery.

2. Through spatial control of multiple chromophore types, antennas can exothermically funnel excitons over large distances (~50 nm) with quantum efficiencies of 95% through an energy cascade.[24] By controlling energy flow, antennas can use multiple components optimized for their specific functions, like high photoluminescence efficiency.

These characteristics have found use of one class of antennas, the phycobilisomes of red algae and cyanobacteria, as fluorescent markers.[128] Their energy cascade structure is well suited for high self-transparency. Their structure is schematically represented in Figure 3.22. Phycoerythrins (PE) at the periphery absorb light and funnel it to allophcocyanin (APC) proteins at the core, which are less in number. The absorption and emission of PE is shown in Figure 3.22b. When isolated, they have considerable self overlap between absorption and emission, an undesirable trait for OSCs. But when present in their full complex, light absorbed by PEs are funneled to APCs, whose spectra is also shown in Figure 3.22b. The Stokes shift increases by approximately 125 nm.

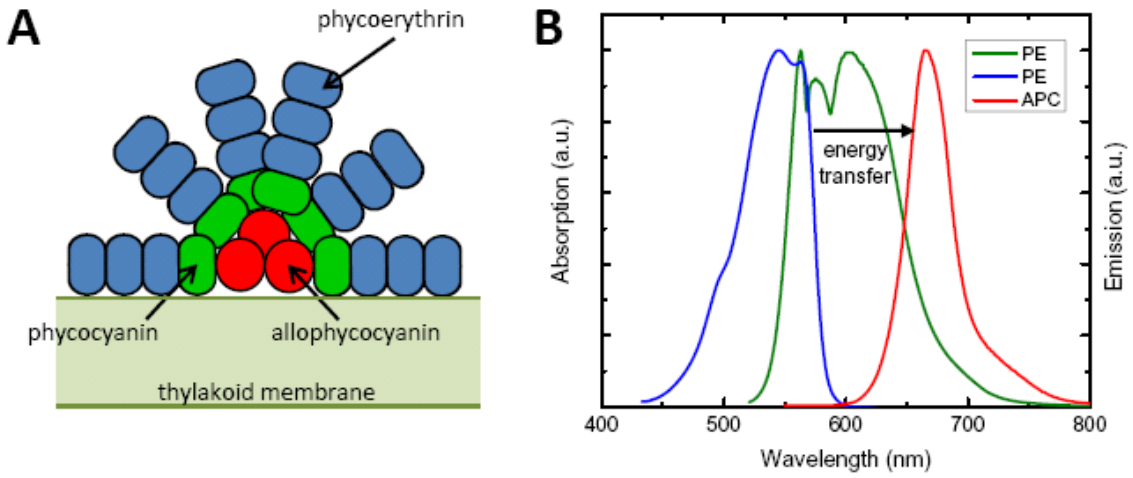

Figure 3.22 Phycobilisome structure and optical spectra

(A) Phycobilisomes in hemispherical in a core-periphery structure. Light is absorbed by phycoerythrin proteins and exothermically funneled to the reaction center, which sits below allophcocyanin. **(B)** Isolated phycoerythrin absorb light (blue) and undergo emission (green) with minimal energy shift. If excitons are funneled to APC, emission is bathochromically shifted by approximately 125 nm, considerably lowering the probability of self-absorption by decreasing the overlap of absorption and emission spectra.

3.14 OSC performance limits

3.14.1 Single OSC

We can construct a simple model for a tandem guide OSC performance potential by idealizing absorption, photoluminescence efficiencies, and self-absorption losses into the single product of optical quantum efficiency (OQE). The power conversion efficiency of a single OSC coupled to a GaInP cell is shown in Figure 3.23 as a function of cutoff absorption wavelength, λ_{top}, and OQE. The conversion efficiency increases as OQE increases and as λ_{top} approaches the absorption cutoff of GaInP, eventually approaching

the values of bare GaInP. We can see that losses from λ_{top} decreasing by 50 nm are similar to decreases in OQE by 20%.

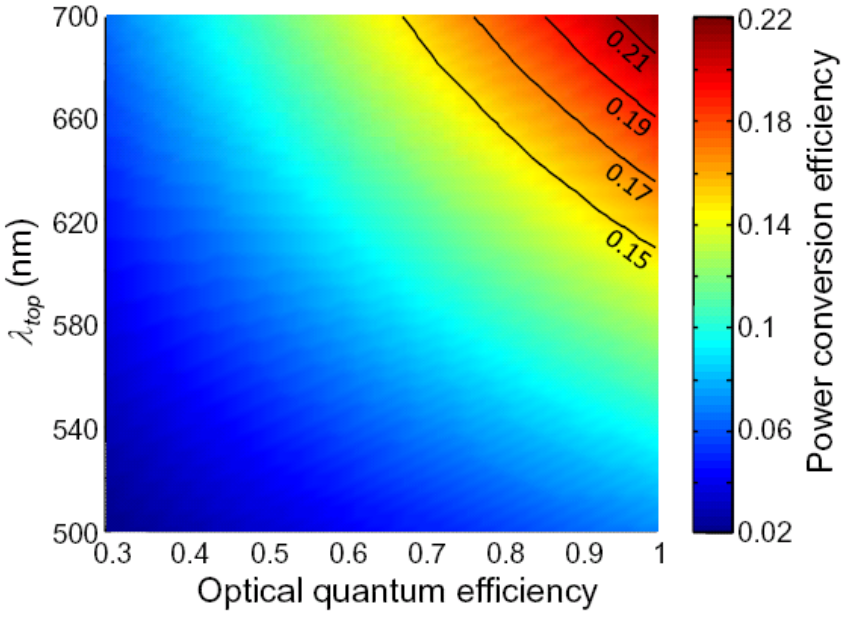

Figure 3.23 Single OSC performance limit

In this calculation, the OSC is coupled to a GaInP with an open circuit voltage of V_{OC}=1.34 V, a fill factor FF=0.9, and quantum efficiency at the emission wavelength of η_{EQE}=0.9.

3.14.2 Dual guide OSC

To understand losses inherent to the tandem OSC, the conversion efficiency of a system of two single junction conventional solar cells is shown in Figure 3.24 as a function of the cutoff wavelengths λ_{top} and λ_{bot}. The current and voltages were modeled using the method of Green,[129] excepting that the currents passing through each junction were not constrained to match. A system comprised of these two cells is not realizable in practice, as current matching is always required. The system peaks at an efficiency of 45% for a

top cell with that absorbs all of the visible and a bottom cell cutting off in the near infrared at approximately 1100 nm.

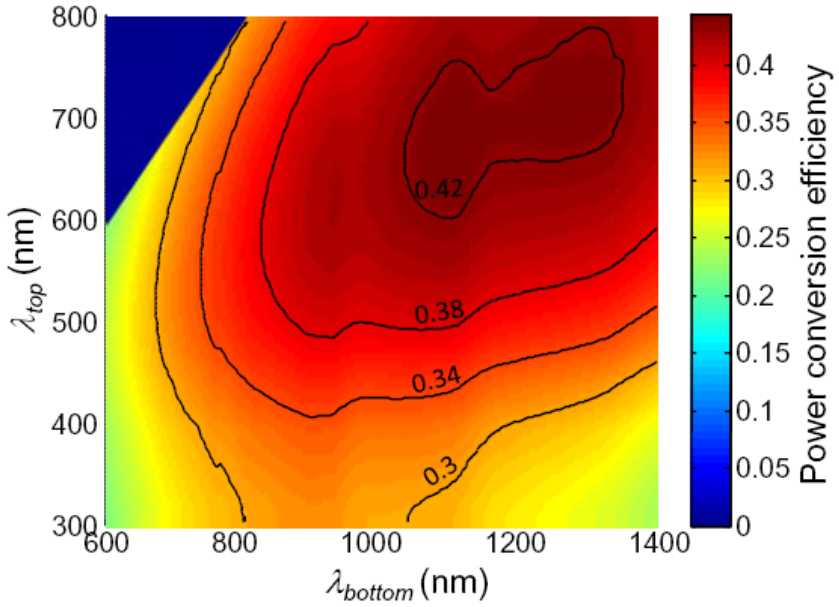

Figure 3.24 Tandem double junction PV efficiency limits

In this calculation, two stacked solar cells covert light to current with unity quantum efficiency; their currents are not constrained to match. The maximum power conversion efficiency as a function of cutoff absorption wavelengths is shown. For cutoff wavelengths of 700 and 1200 nm, efficiencies of approximately 45% are possible. In practice the two cells are serially constrained to pass equal currents; realizable efficiencies are lower.

We desire to know the efficiency limits effect of dual guide OSCs. We first idealize OQE as unity and assume a 100 nm Stokes shift between the absorption and emission peaks of the chromophores in each guide. For high optical concentration, a 100 nm shift or more is required. As illustrated in Figure 3.25, the efficiency landscape changes little in shape, but the maximum efficiency has been diminished by

approximately 8%. The effect of imperfect OQE is found by direct multiplication by the scale. For a more realistic value of 75%, the maximum conversion efficiency is about 25%, a full 20% absolute lower than the dual solar cells comparison case.

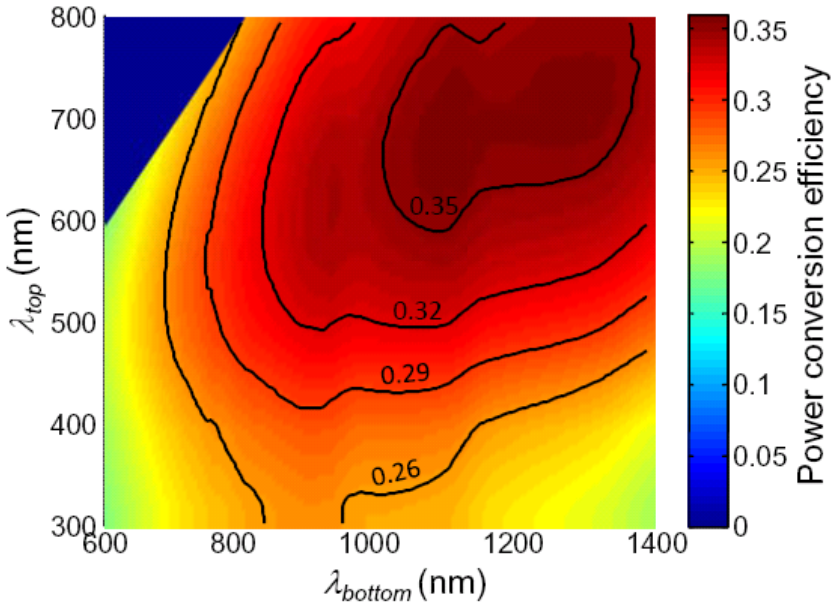

Figure 3.25 Tandem OSC conversion efficiency limits

The two OSCs operate at unity optical quantum efficiency and coupling to the solar cell is 100%. A rigid wavelength shift of 100 nm is assumed for each guide to lower self-absorption.

3.14.3 Hybrid OSC- thin film PV

In a hybrid OSC-thin film PV system, sunlight incident on the bottom cell is filtered though the top OSC. To maximize total conversion efficiency, we desire to choose the bottom semiconductor to extract maximum electrical power from the filtered spectrum. Treating the top OSC as a long pass filter on the AM1.5G spectrum, we generate design curves showing the ideal bottom PV bandgap as a function of top OSC absorption cutoff.

These curves are shown in Figure 3.26. As the cutoff wavelength increases, the bandgap yielding maximum conversion efficiency shifts to the lower energies. For direct incidence, we see that cadmium telluride (CdTe) solar cells possess the nearly ideal bandgap for maximum possible efficiency. As the light is filtered through the OSC, the PV bandgap of maximum possible conversion decreases in energy and silicon and cadmium indium gallium selenide (CIGS) are better suited.

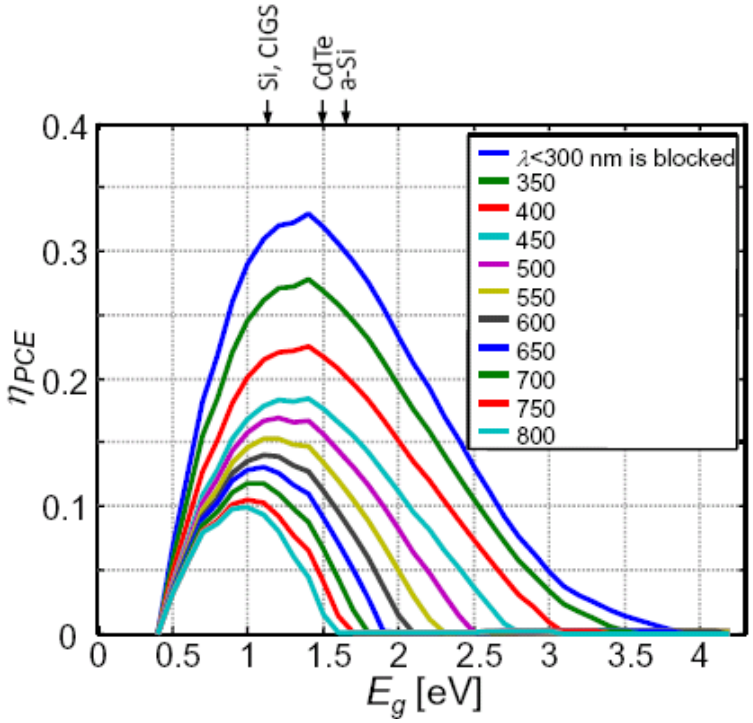

Figure 3.26 Hybrid OSC-thin film PV bandgap selection curves

As the incident AM1.5G solar spectrum is long pass filtered by a top OSC, the bandgap that results in maximum conversion efficiency for the thin film alone shifts to lower energies. In direct sunlight, cadmium telluride is nearly ideal, but for a realistic OSC absorption cutoff of 650-700 nm, cadmium indium gallium selenide or silicon has a higher conversion limit.

These curves are useful as design guides. We can further calculate the maximum possible conversion efficiency as a function of λ_{top} and λ_{bot}; the result is shown in Figure 3.27. Efficiency peaks at roughly 38%, in between the maxima for the dual solar cell and dual OSC cases.

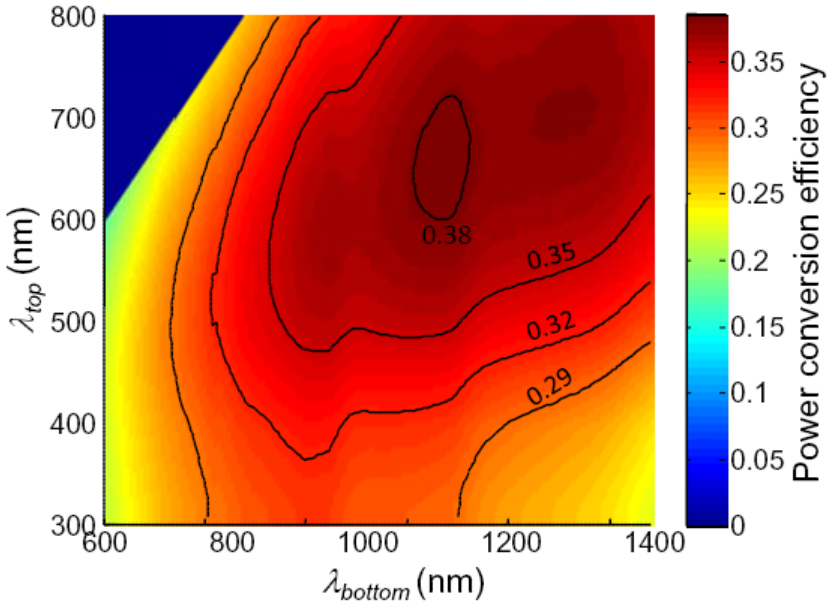

Figure 3.27 Hybrid OSC-thin film PV cutoff absorption wavelength selection curves
For the hybrid system, the maximum possible is between the dual junction PV and dual guide OSC cases.

It is worthwhile to consider the maximum system η_{PCE} as the top OSC is matched with an existing in-production thin film PV device. We set the top OSC to be coupled to a GaInP solar cell. The result, as a function of λ_{top} and OQE, is shown in Figure 3.28a and Figure 3.29a for CdTe from First Solar and CIGS from Shell Solar, respectively. The relative proportion of power conversion between the top OSCs and bottom PV devices

can be understood from Figure 3.28b and Figure 3.29b. In each case, the bottom PV cell performance steadily diminishes as the top OSC shadows the device completely.

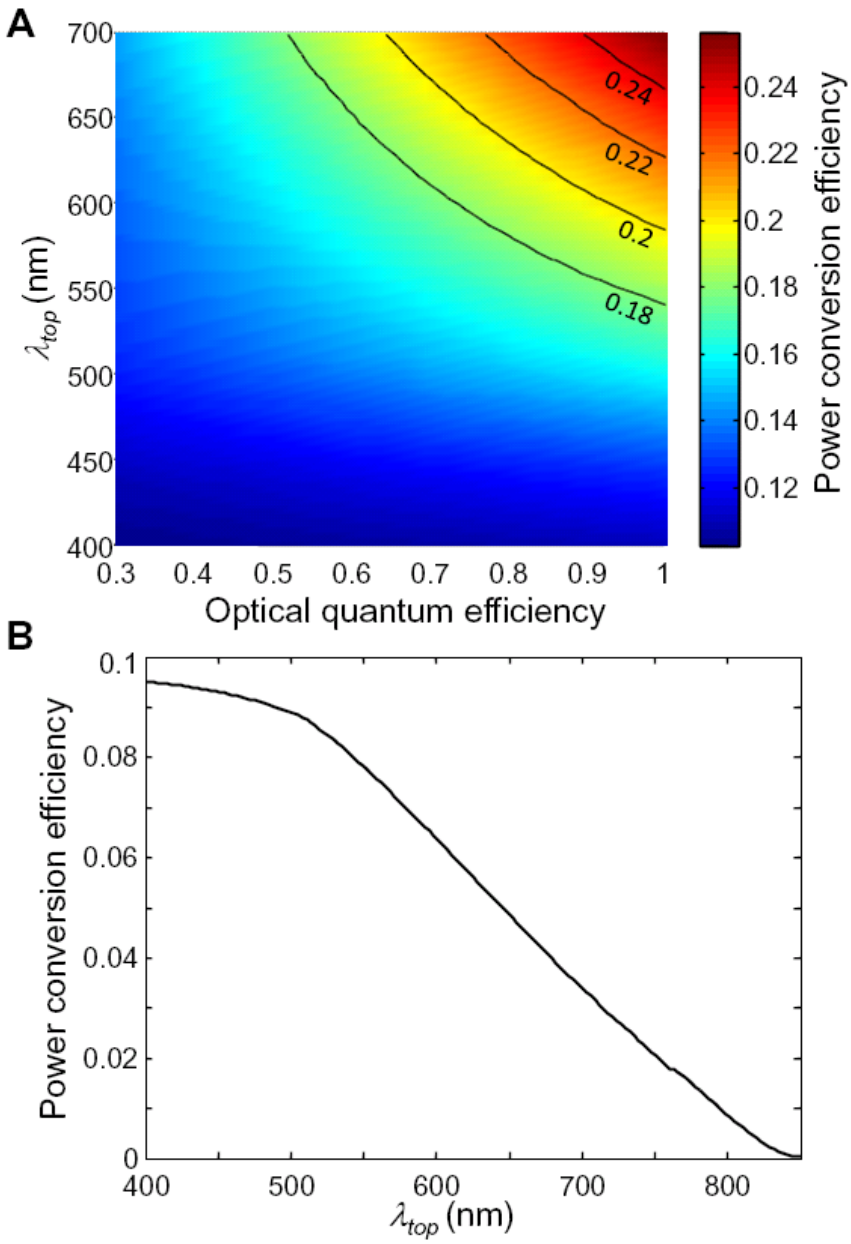

Figure 3.28 Hybrid OSC-production CdTe performance expectation.

(A) The more practical case of a top OSC coupled to GaInP over an in-production cadmium telluride cell is dependent on both OSC absorption cutoff wavelength and OSC optical quantum efficiency. A decrease in OQE by 30% is equivalent to sacrificing 125 nm of absorption. In this calculation, the thin film performance parameters are shown in Table 3.1 and the GaInP parameters are listed in the caption of Figure 3.23. **(B)** The conversion efficiency of the bottom CdTe cell alone steadily diminishes as the top OSC absorbs more light.

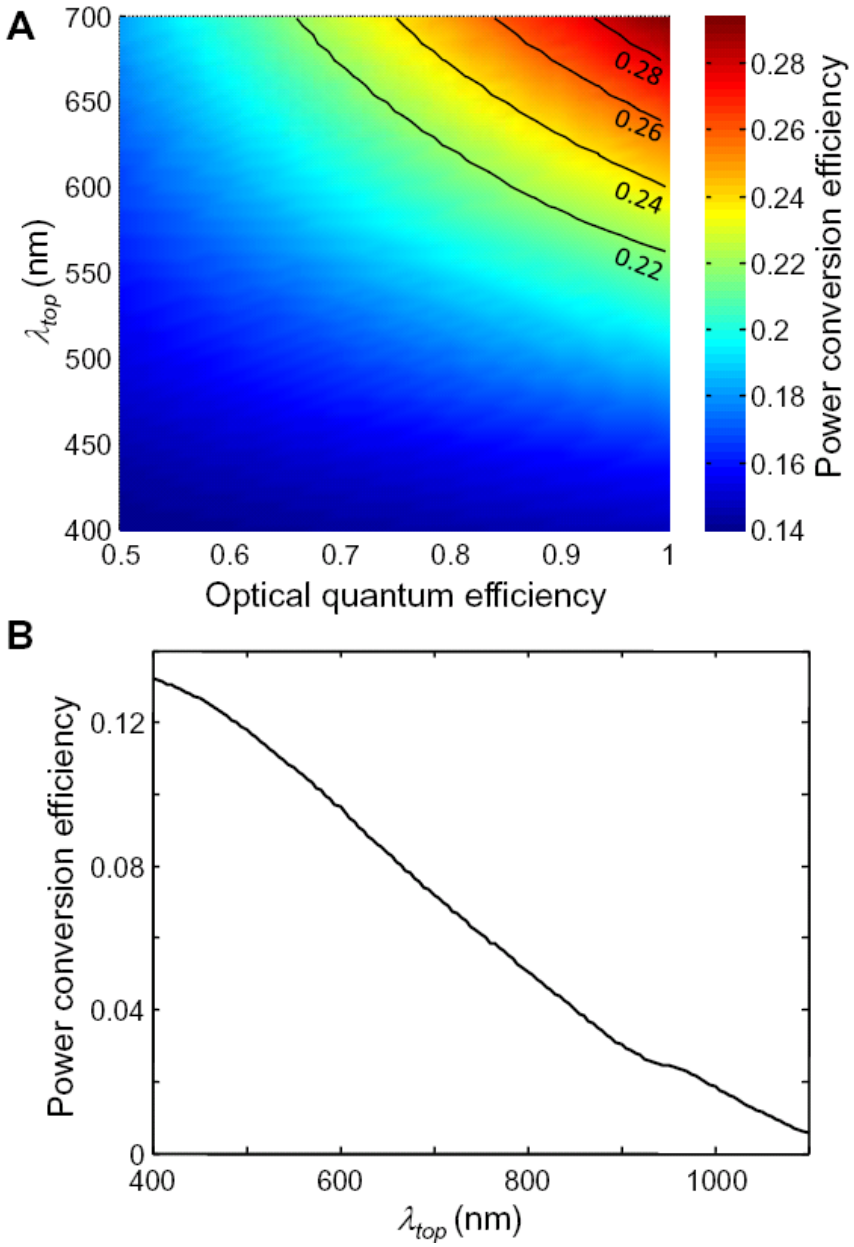

Figure 3.29 Hybrid OSC-production CIGS performance expectation

(A) System power conversion efficiency. Thin film performance parameters are shown in Table 3.1. **(B)** Conversion efficiency of the bottom CIGS cell alone.

The device configuration of an OSC coupled to GaInP provides an attractive route to increasing efficiencies of existing low cost thin film solar cells.

3.15 OSC costs

The cost of a PV concentrator measured in cost per peak Watt generated, $(\$/W_p)_{conc}$, is determined by its flux gain, which is equal to the geometric gain corrected for efficiency losses in the concentrator, i.e. $F = G\eta_{conc}/\eta_{PV}$ and

$$\left(\$/W_p\right)_{conc} = \frac{\text{collector cost}}{\eta_{conc} L} + \frac{1}{F}\left(\$/W_p\right)_{PV}, \tag{25}$$

where L is the solar intensity, $(\$/W_p)_{PV}$ is the cost of the PV cell, and the power efficiencies of the concentrator and PV are η_{conc} and η_{PV}, respectively.[93,94] Thus, the design of a solar concentrator requires: (*i*) minimizing the collector cost, (*ii*) maximizing η_{conc} (to defray the collector cost) and (*iii*) maximizing $G\eta_{\text{conc}}$ (to defray the PV cost). To compete with conventional power generation, $(\$/W_p)_{conc}$ must be < $\$1/W_P$.[8] In the sections that follow, we address the projected costs of the solar cells and collector.

3.15.1 Solar cell costs

The ideal cells for the OSCs considered in this work are single junction GaInP cells. These are not produced in large quantities so manufacturing costs are uncertain. However, we can begin an analysis by using costs for the more complex triple junction solar cells designed for high concentration (500-1500x) systems.

Emcore recently contracted the supply of the largest single order for triple junction solar cells (where the top cell in the stack was GaInP) at a cost of approximately \$8/cm^2 for 0.1 MW_P.[130] The devices are 37% efficient, translating to $\left(\$/W_p\right)_{PV} = \$218/W_P$.

Since light is being downconverted in an OSC to a narrow range of wavelengths, commercially available multijunction cells are not a good fit to receive the concentrated light. The current matching requirements of multijunction cells make their design highly dependent on incident spectral load. However, we can use the multijunction price as a proxy to evaluate the required flux gains to make an OSC system commercially viable. If the cells cannot cost more than 30% of the module cost, then this treatments dictates F>700.

The flux gain threshold for commercial viability set by solar cell costs is too high. This is in part due to the market niche that triple junction solar cells occupy. The Emcore cells considered here are operated at G=1100 and F=1360 and are well suited for operation in 2 axis parabolic dish concentrators. For very high F, the cell efficiency affects the system costs more strongly than cell cost, and there is little incentive to make the cells less expensive, especially if efficiency were to decrease.

Middle range concentrator PV systems, such as the kind considered here, are conspicuously absent from the market, as is the strong motivation to reduce cell costs. A major fraction of costs of these cells resides in the germanium wafer. Lattice matched semiconductors and substrates are used to reduce defect density and trapping centers. Commercially available triple junction cells utilize germanium (Ge) and gallium arsenide (GaAs) cells, which has 4% lattice mismatch to silicon.[131] If high efficiencies were

possible, Si wafers are preferred for their larger size (up to 12" diameter), greater technical maturity, and lower cost per unit area.

Several academic groups and companies are pursuing techniques to replace expensive GaAs or Ge wafer with silicon for photovoltaics and integrated optoelectonics applications through a number of approaches, including hydrophobic direct wafer bonding,[132] graded SiGe buffer layers,[131] epitaxial necking[133] or aspect ratio trapping,[134] cycle thermal annealing,[135] epitaxial lateral overgrowth,[136] and strained layer superlattices.[137] However, defect densities are far greater than single crystal wafers.

If we assume that OSCs are possible with F=200 and the solar cell cannot be greater than 30% of total system cost, then the cells are constrained to cost no more than \$60/W_P. With an assumed cell conversion efficiency of 18%, this translates to \$1.80/cm^2, a reduction in cost of 78% compared to the triple junction on Ge cells. With wafer substitution, this is entirely achievable, especially if the current 4" wafers could be increased such that the fixed costs associated with metalorganic chemical vapor deposition epitaxial growth can be distributed over larger areas and manufacturing throughput increases. In fact, much lower costs are possible; Algora[138] suggests wafer replacement could reduce triple junction cell costs to €2/cm^2, so single junction GaInP cells should be much less expensive, as far fewer layers are needed and the design constraints of very low series resistance, current matching, and high quantum efficiencies across the solar spectrum are eliminated or relaxed.

For a hybrid OSC-thin film PV device configuration, modularization costs can be shared and further diluted by the higher efficiencies. To fully achieve a low cost system,

the collector cost must also be low. Two main costs in the collector are materials (substrate and chromophores) and processing.

3.15.2 Collector costs: materials

There are two approaches to consider dye materials costs. We can take representative costs for emissive organic chromophores used in organic light emitting diode (OLED) displays, which have similar performance requirements to OSCs. Alternatively, we can consider costs for existing OSC compatible materials that other groups are considering for fluorescent concentrators that do not employ thin films, which are employed in other industries in large volumes.

The OLED display industry is growing quickly. Sony recently started shipping 11" displays, so commercial production exists. Estimates for emissive materials costs are roughly \$500/g.[139] If coating requirements are 0.1 g/m^2 and 100% materials use efficiency is assumed, for a 10% efficient OSC, these emitters would cost \$0.5/W_P.

The perylene dye class of is an ideal candidate for fluorescent concentrator materials for its excellent stability, absorption characteristics, and optical tenability,[108,109] and are available from several major chemical companies in quantities exceeding 1,500,000 kg annually.[34] At these much larger volumes, materials cost approximately \$50/kg. After thermal purification process, these costs could increase by a factor of ten; even so, this is 1000 times less expensive than OLED materials.

Materials for OSCs will likely lie somewhere in between. Existing perylene dyes may need to be modified and more expensive, lower yield variants may be needed. But low cost OSC materials appear feasible.

3.15.3 Collector costs: processing

Thermal evaporation is used in OLED display manufacturing and can be made on Generation 5 glass (1.1 x 1.3 m). These machines are very expensive, but like triple junction PVs, OLEDs are complex multilayer stacks and simple single thick layers with relaxed thickness control requirements could easily lead to a 75% decrease in cost. A conservative estimate used in OLED manufacturing is that per unit area, materials and processing costs are nearly the same. These numbers suggest that manufacturing costs of $\$0.12/W_P$ are possible for thermal evaporation. These costs are manageable, but they can potentially be reduced if solution based processing is possible.

Chapter 4 Conclusions and Outlook

The thesis of this work is that the separation of light harvesting and charge generation offers several advantages in the design of organic photovoltaics and organic solar concentrators for the ultimate end goal of achieving a lower cost solar electric conversion. This path is motivated by 1) the existence of cadmium telluride thin film technology, which has succeeded in drastically reducing semiconductor cost, 2) the desire for very high conversion efficiencies, and 3) utilizing existing high efficiency PV cells in a more economic configuration.

We traveled down this path using organic materials, whose optical characteristics and manufacturing compatibility are especially attractive for low cost systems. In Chapter 2, we sought to increase the efficiency of existing organic photovoltaic devices by utilizing external energy transfer from an adjacent organic antenna film. This unique architecture was analyzed for its functionality and the efficiencies of each added step was quantified. Although the introduction of additional energy transduction will ultimately introduce more losses, bypassing the exciton diffusion bottleneck offered the potential for increased efficiency through judicious device and process design.

The organic charge generating reaction center is freed from the constraint of broadband optical absorption, offering the opportunity to design an artificial reaction center on the basis of high internal quantum efficiency, low series resistance, and stability, negating the necessity for disordered bulk heterojunctions and thick resistive layers to achieve high external quantum efficiency.

Since the optically absorbent component need not conduct excitons or charge, new antenna materials are possible, including J-aggregates, quantum dots, and biomaterials, including photosynthetic antennas. Antenna materials should be chosen for high optical absorption and photoluminescent efficiency. With mixed antenna material and undergo cascade exothermic energy transfer, the photoluminescence requirements is moved to the terminal emitter and weak absorption can be mitigated by using many materials and the long spatial diffusion requirements can be relaxed.

We also sought to enable the use of high efficiency inorganic solar cells in organic solar concentrators, which aim to exploit high performance of the PV cells in low cost, non-tracking configurations. By utilizing thin films of organic chromophores on high refractive index glass substrates, we were able to apply the recent advances of organic optoelectonics to the fluorescent concentrator platform, including near field energy transfer, solid state solvation, and phosphorescence. By reducing self-absorption losses, we demonstrated optical flux gains an order of magnitude greater than previously published results and thereby reduce the effective cost of inorganic solar cells by at least a factor of ten. Combined with the potential for low cost solution processing, the high flux gains and power efficiencies realized here should enable a new source of inexpensive solar power.

Appendix

Non-emissive molecular structures

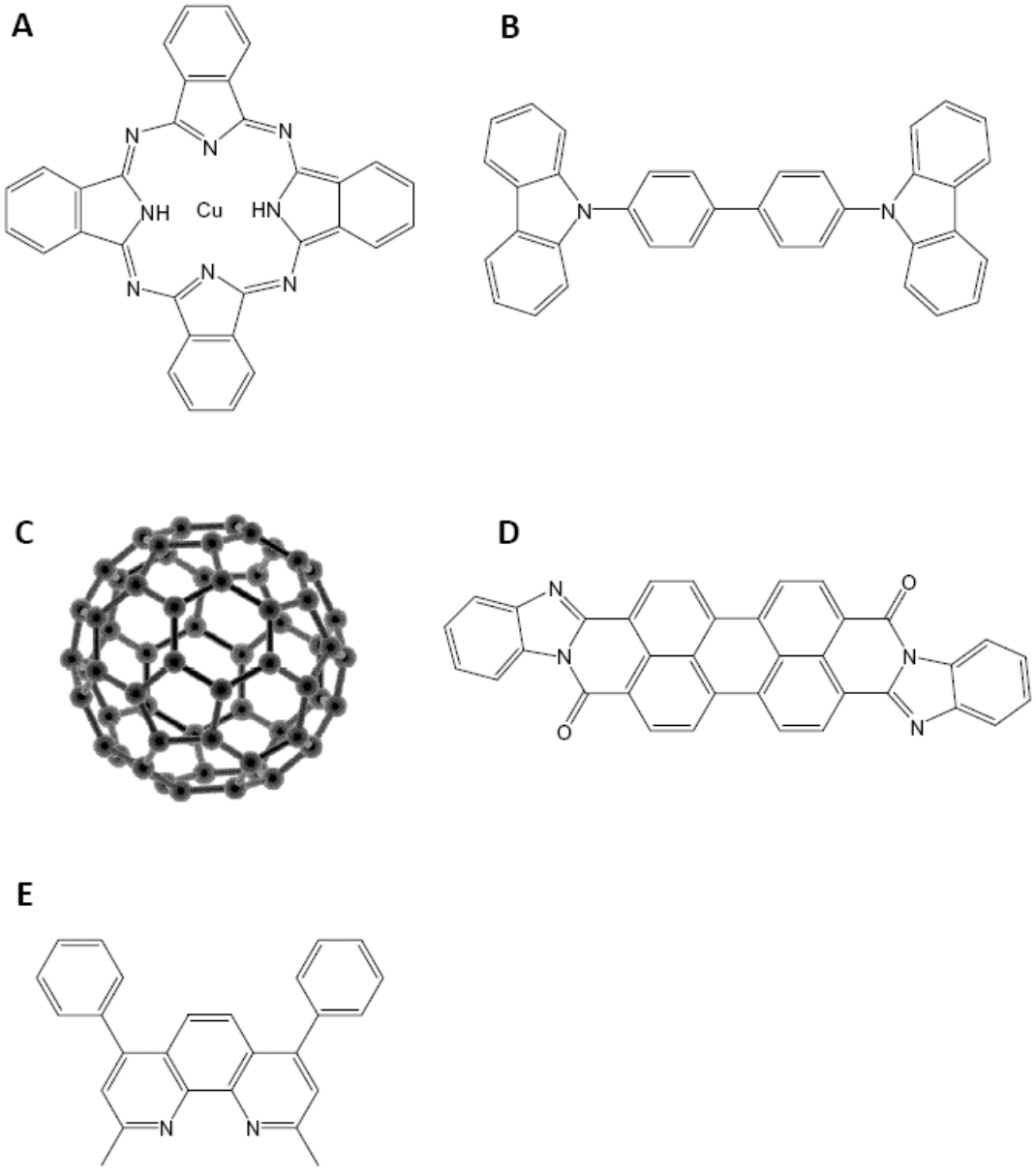

A, copper phthalocyanine (CuPC)[140]
B, carbazole biphenyl (CBP)[141]
C, buckminister fullerene (C_{60})[49]
D, 3,4,9,10-perylenetetracarboxylicbis-benzimidazole (PTCBI)[49]
E, bathocuproine (BCP)[49]

Emissive molecular structures

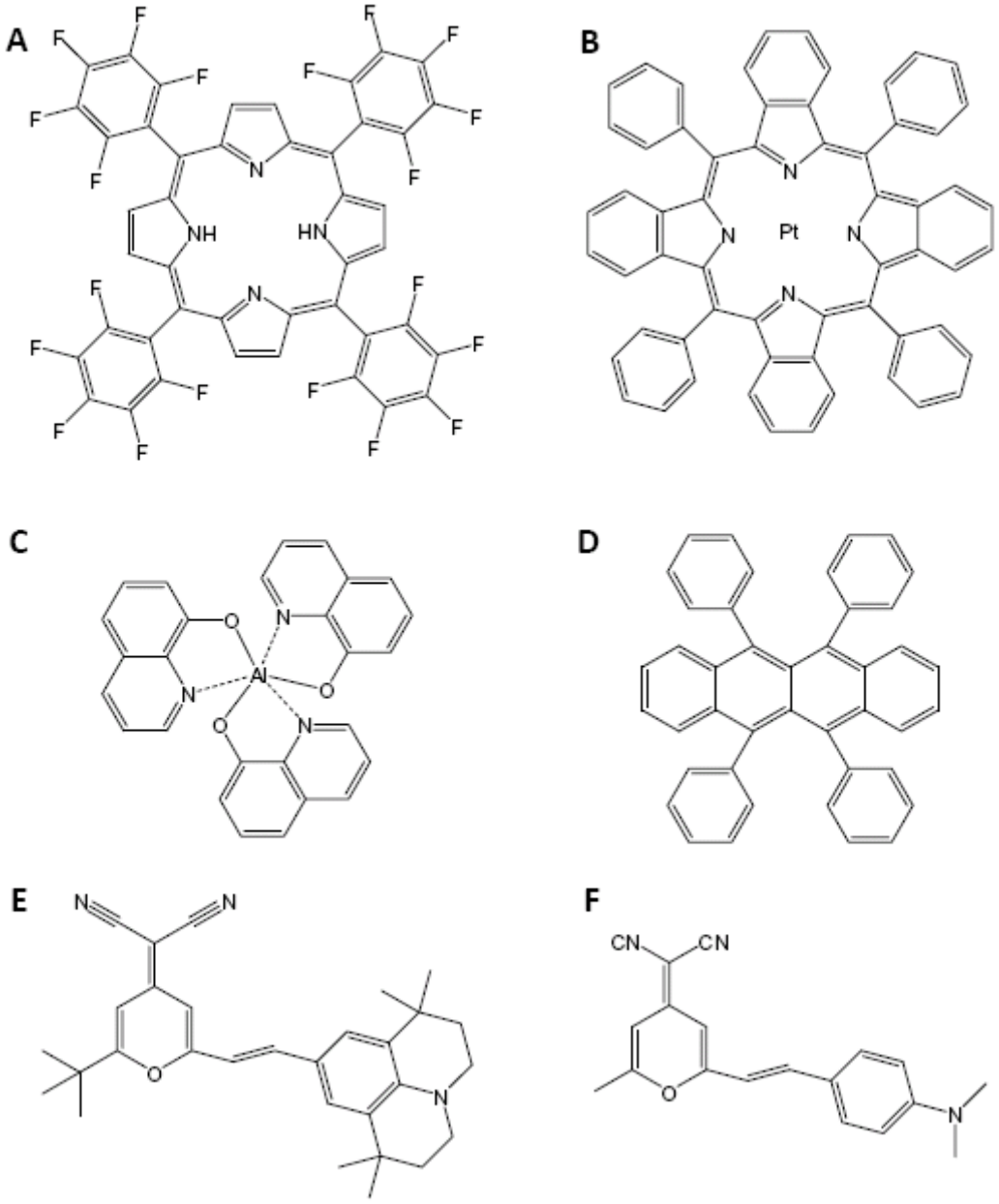

A, tetrakis(pentafluorophenyl)porphyrin (H_2FTPP)
B, Pt(II)-tetraphenyltetrabenzoporphyrin (Pt(TPTBP))[142]
C, tris-(8-hydroxyquinoline) aluminium (AlQ3)[140]
D, 5,6,11,12-tetraphenylnaphthacene, (rubrene)[143]
E, 4-dicyanomethylene-2-t-butyl-6-(1,1,7,7-tetramethyljulolidyl-9-enyl)-4*H*-pyran (DCJTB)[144]
F, 4-dicyanomethylene-2-methyl-6-(p-dimethylaminostyryl)-4*H*-pyran (DCM)[145]

Bibliography

[1] U.S. Department of Energy, "International Energy Outlook" (2007).

[2] U.S. Department of Energy, "Basic Research Needs for Solar Energy Utilization" (2005).

[3] E. Becquerel, Comptes Rendus **9,** 561 (1839).

[4] D. Chapin, C. Fuller, and G. Pearson, Journal of Applied Physics **25,** 676 (1954).

[5] S. Kurtz, D. Myers, and J. Olson, in *Proceedings of the 26th IEEE Photovoltaic Specialists Conference*, 1997, p. 875-878.

[6] Solarbuzz, "Marketbuzz," (2007).

[7] DeutscheBank, "Solar Photovoltaics," (2007).

[8] K. Zweibel, "The terawatt challenge for thin-film PV," Report No. NREL/TP-520-38350 (2005).

[9] M. S. Keshner and R. Arya, "Study of potential cost reductions resulting from super-large-scale manufacturing of PV modules," (2004).

[10] DeutscheBank, "First Solar (Global Markets Research)," (2007).

[11] K. Zweibel, Solar Energy Materials and Solar Cells **63,** 375-386 (2000).

[12] K. Zweibel, Solar Energy Materials and Solar Cells **59,** 1-18 (1999).

[13] R. R. King, D. C. Law, K. M. Edmondson, C. M. Fetzer, G. S. Kinsay, H. Yoon, R. A. Sherif, and N. H. Karam, Applied Physics Letters **90,** 183516 (2007).

[14] "Mineral Commodity Summaries (Mineral Resources Program)," (http://minerals.usgs.gov/minerals/pubs/mcs/2005/mcs2005.pdf).

[15] M. Bosi and C. Pelosi, Progress in Photovoltaics: Research and Applications **15,** 51-68 (2007).

[16] R. M. Swanson, Progress in Photovoltaics: Research and Applications **8,** 93-111 (2000).

[17] J. Siemer, in *Photon International* (10/2007).

[18] G. T. Byrd and P. A. May II, Crop Science **40,** 1271-1277 (2000).

[19] K. A. Cassida, J. P. Muir, M. A. Hussey, J. C. Read, V. B. C., and W. R. Ocumpaugh, Crop Science **45,** 673-680 (2005).

[20] G. A. Montano, B. P. Bowen, J. T. LaBelle, N. W. Woodbury, V. B. Pizziconi, and R. E. Blankenship, Biophysical Journal **85,** 2560 (2003).

[21] A. Sussman, Journal of Applied Physics **38,** 2738-2748 (1967).

[22] D. Walker, *Energy, Plants and Man* (Oxygraphics, Brighton, 1992).

[23] W. K. Purves, *Life, the science of biology*, 7th ed. (Sinauer, Sunderland, 2004).

[24] B. R. Green and W. W. Parson, *Light-Harvesting Antennas in Photosynthesis*, Vol. 13 (Kluwer Academic, Dordrecht, 2003).

[25] R. E. Blankenship, *Molecular Mechanisms of Photosynthesis*, 1 ed. (Blackwell Science, Oxford, 2002).

[26] A. J. Hoff and J. Deisenhofer, Physics Reports **287,** 1-247 (1997).

[27] W. Humphrey, A. Dalke, and K. Schulten, J. Molec. Graphics **14,** 33-38 (1996).

[28] J. R. Sheats, Journal of Materials Research **19,** 1974-1989 (2004).

[29] J. Y. Kim, K. Lee, N. E. Coates, D. Moses, T. Q. Nguyen, M. Dante, and A. J. Heeger, Science **317,** 222-225 (2007).

[30] J. G. Xue, B. P. Rand, S. Uchida, and S. R. Forrest, Advanced Materials **17,** 66-+ (2005).

[31] S. R. Forrest, MRS Bulletin **30,** 28-32 (2005).

[32] R. R. Chance, A. Prock, and R. Silbey, Advances in Chemical Physics **37,** 1 (1978).

[33] N. B. McKeown, *Phthalocyanine materials: synthesis, structure, and function* (Cambridge University Press, Cambridge, U.K. ; New York, 1998).

[34] M. Greene, in *High Performance Pigments*, edited by H. M. Smith (Wiley-VCH, 2002).

[35] D. Wohrle, Macromolecular Rapid Communications **22,** 68-97 (2001).

[36] B. A. Gregg, Journal of Physical Chemistry B **107,** 4688-4698 (2003).

[37] H. Hoppe and N. S. Sariciftci, Journal of Materials Research **19,** 1924-1945 (2004).

[38] J. Nelson, Current Opinion in Solid State & Materials Science **6,** 87-95 (2002).

[39] B. P. Rand, J. Genoe, P. Heremans, and J. Poortmans, Progress in Photovoltaics: Research and Applications **15,** 659-676 (2007).

[40] M. Gratzel, Progress in Photovoltaics **8,** 171-185 (2000).

[41] M. Gratzel, Nature **414,** 338-344 (2001).

[42] M. Gratzel, Journal of Photochemistry and Photobiology C-Photochemistry Reviews **4,** 145-153 (2003).

[43] M. Gratzel, Journal of Photochemistry and Photobiology A-Chemistry **164,** 3-14 (2004).

[44] M. Gratzel, Inorganic Chemistry **44,** 6841-6851 (2005).

[45] M. Gratzel, MRS Bulletin **30,** 23-27 (2005).

[46] K. M. Coakley, Y. X. Liu, C. Goh, and M. D. McGehee, MRS Bulletin **30,** 37-40 (2005).

[47] K. M. Coakley and M. D. McGehee, Applied Physics Letters **83,** 3380-3382 (2003).

[48] I. Gur, N. A. Fromer, M. L. Geier, and A. P. Alivisatos, Science **310,** 462-465 (2005).

[49] P. Peumans, A. Yakimov, and S. R. Forrest, Journal of Applied Physics **93,** 3693-3723 (2003).

[50] M. Pope and C. Swenberg, *Electronic Processes in Organic Crystals*, 1st ed. (Oxford University Press, Oxford, 1982).

[51] E. A. Silinsh and V. Capek, *Organic Molecular Crystals: Interaction, Localization, and Transport Phenomena* (AIP Press, New York, 1994).

[52] G. Zerza, C. J. Brabec, G. Cerullo, S. De Silvestri, and N. S. Sariciftci, Synthetic Metals **119,** 637-638 (2001).

[53] G. Li, V. Shrotriya, J. S. Huang, Y. Yao, T. Moriarty, K. Emery, and Y. Yang, Nature Materials **4,** 864-868 (2005).

[54] P. Peumans, S. Uchida, and S. R. Forrest, Nature **425,** 158-162 (2003).

[55] W. U. Huynh, J. J. Dittmer, and A. P. Alivisatos, Science **295,** 2425-2427 (2002).

[56] M. Law, L. E. Greene, J. C. Johnson, R. Saykally, and P. D. Yang, Nature Materials **4,** 455-459 (2005).

[57] C. J. Brabec, N. S. Sariciftci, and J. C. Hummelen, Advanced Functional Materials **11,** 15-26 (2001).

[58] P. Peumans, V. Bulovic, and S. R. Forrest, Applied Physics Letters **76,** 2650-2652 (2000).

[59] C. J. Brabec, G. Zerza, G. Cerullo, S. De Silvestri, S. Luzzati, J. C. Hummelen, and S. Sariciftci, Chemical Physics Letters **340,** 232-236 (2001).

[60] B. P. Rand, P. Peumans, and S. R. Forrest, Journal of Applied Physics **96,** 7519-7526 (2004).

[61] E. H. Sargent, Advanced Materials **17,** 515-522 (2005).

[62] W. L. Barnes, A. Dereux, and T. W. Ebbesen, Nature **424,** 824-830 (2003).

[63] H. Raether, *Surface plasmons on smooth and rough surfaces and on gratings*, Vol. 111 (Springer-Verlag, Berlin, 1987).

[64] P. B. Johnson and R. W. Christy, Physical Review B **6,** 4370-4379 (1972).

[65] E. Kretschmann and H. Raether, Zeitschrift für Naturforschung **23A,** 2135–2136 (1968).

[66] J. Homola, S. S. Yee, and G. Gauglitz, Sensors and Actuators B-Chemical **54,** 3-15 (1999).

[67] T. Wakamatsu, K. Saito, Y. Sakakibara, and H. Yokoyama, Japanese Journal of Applied Physics Part 1-Regular Papers Short Notes & Review Papers **36,** 155-158 (1997).

[68] T. Kume, S. Hayashi, and K. Yamamoto, Japanese Journal of Applied Physics Part 1-Regular Papers Short Notes & Review Papers **32,** 3486-3492 (1993).

[69] P. Peumans and S. R. Forrest, Applied Physics Letters **79,** 126-128 (2001).

[70] K. Suemori, M. Yokoyama, and M. Hiramoto, Journal of Applied Physics **99,** 036109 (2006).

[71] B. P. Rand, J. Li, J. G. Xue, R. J. Holmes, M. E. Thompson, and S. R. Forrest, Advanced Materials **17,** 2714-2718 (2005).

[72] G. V. Morozov, R. G. Maev, and G. W. F. Drake, Quantum Electronics **31,** 767-773 (2001).

[73] T. Inagaki, K. Kagami, and E. T. Arakawa, Applied Optics **21,** 949-954 (1982).

[74] J. Moreland, A. Adams, and P. K. Hansma, Physical Review B **25,** 2297-2300 (1982).

[75] H. Tajima, M. Haraguchi, and M. Fukui, Surface Science **323,** 282-287 (1995).

[76] L. A. A. Pettersson, L. S. Roman, and O. Inganas, Journal of Applied Physics **86,** 487-496 (1999).

[77] W. H. Weber and C. F. Eagen, Optics Letters **4,** 236-238 (1979).

[78] W. L. Barnes, Journal of Modern Optics **45,** 661-699 (1998).

[79] P. Andrew and W. L. Barnes, Science **306,** 1002-1005 (2004).

[80] D. H. Drexhage, *Progress in Optics XII* (North-Holland, Amsterdam, 1974).

[81] K. Celebi, T. D. Heidel, and M. A. Baldo, Optics Express **15,** 1762-1772 (2007).

[82] P. Peumans, V. Bulovic, and S. R. Forrest, Applied Physics Letters **76,** 2650-2652 (2000).

[83] G. Calzaferri, M. Pauchard, H. Maas, S. Huber, A. Khatyr, and T. Schaafsma, Journal of Materials Chemistry **12,** 1-13 (2002).

[84] P. Peumans, V. Bulovic, and S. R. Forrest, Applied Physics Letters **76,** 3855-3857 (2000).

[85] H. Mattoussi, H. Murata, C. D. Merritt, Y. Iizumi, J. Kido, and Z. H. Kafafi, Journal of Applied Physics **86,** 2642-2650 (1999).

[86] T. D. Heidel, J. K. Mapel, M. Singh, K. Celebi, and M. A. Baldo, Applied Physics Letters **91,** 093506 (2007).

[87] S. Bailey and R. Raffaelle, in *Handbook of Photovoltaic Science and Engineering*, edited by A. Luque and S. Hegedus (John Wiley & Sons, 2003), p. 413-448.

[88] G. Smestad, H. Ries, R. Winston, and E. Yablonovitch, Solar Energy Materials **21,** 99-111 (1990).

[89] A. Goetzberger and W. Greubel, Applied Physics **14,** 123-139 (1977).

[90] W. H. Weber and J. Lambe, Applied Optics **15,** 2299-2300 (1976).

[91] K. Zweibel, Solar Energy Materials & Solar Cells **63,** 375-386 (2000).

[92] A. Woyte, J. Nijs, and R. Belmans, Solar Energy **74,** 217-233 (2003).

[93] J. S. Batchelder, A. H. Zewail, and T. Cole, Applied Optics **18,** 3090-3110 (1979).

[94] J. S. Batchelder, A. H. Zewail, and T. Cole, Applied Optics **20,** 3733-3754 (1981).

[95] E. Yablonovitch, Journal of the Optical Society of America **70,** 1362-1363 (1980).

[96] T. Förster, Discussions of the Faraday Society **27,** 7-17 (1959).

[97] V. Bulovic, A. Shoustikov, M. A. Baldo, E. Bose, V. G. Kozlov, M. E. Thompson, and S. R. Forrest, Chemical Physics Letters **287,** 455-460 (1998).

[98] M. A. Baldo, D. F. O'Brien, Y. You, A. Shoustikov, S. Sibley, M. E. Thompson, and S. R. Forrest, Nature **395,** 151-154 (1998).

[99] M. G. Debije, C. W. M. Bastiaansen, D. J. Broer, M. J. Escuti, and C. Sanchez, edited by W. I. P. Organization (NL, 2006).

[100] Y. Fink, J. N. Winn, S. H. Fan, C. P. Chen, J. Michel, J. D. Joannopoulos, and E. L. Thomas, Science **282,** 1679-1682 (1998).

[101] D. N. Chigrin, A. V. Lavrinenko, D. A. Yarotsky, and S. Gaponenko, Applied Physics a-Materials Science & Processing **68,** 25-28 (1999).

[102] W. Shockley and H. J. Queisser, Journal of Applied Physics **32,** 510-519 (1961).

[103] A. Royne, C. J. Dey, and D. R. Mills, Solar Energy Materials & Solar Cells **86,** 451-483 (2005).

[104] M. W. Edenburn, in *14th IEEE Photovoltaic Specialists Conference* (1980).

[105] K. T. Feldman, D. D. Kenney, and M. W. Edenburn, in *15th IEEE Photovoltaic Specialists Conference* (1981).

[106] L. W. Florschuetz, C. R. Truman, and D. E. Metzger, Journal of Heat Transfer **103,** 337-342 (1981).

[107] A. Luque, G. Sala, J. c. Arboiro, T. Bruton, D. Cunningham, and N. Mason, Progress in Photovoltaics: Research and Applications **5,** 195-212 (1997).

[108] R. Kinderman, L. H. Slooff, A. R. Burgers, N. J. Bakker, A. Buchtemann, R. Danz, and J. A. M. v. Roosmalen, Journal of Solar Engineering **129,** 277-280 (2007).

[109] L. H. Slooff, T. Budel, A. R. Burgers, N. J. Bakker, A. Buchtemann, R. Danz, T. Meyer, and A. Meyer, in *The luminescent concentrator: stability issues*, Milan, 2007.

[110] M. S. Weaver, R. C. Kwong, V. A. Adamovich, M. Hack, and J. J. Brown, Journal of the Society for Information Display **14,** 449-452 (2006).

[111] J. Shi and C. W. Tang, Applied Physics Letters **70,** 1665-1667 (1997).

[112] C. Borek, K. Hanson, P. I. Djurovich, M. E. Thompson, K. Aznavour, R. Bau, Y. R. Sun, S. R. Forrest, J. Brooks, L. Michalski, and J. Brown, Angewandte Chemie-International Edition **46,** 1109-1112 (2007).

[113] V. V. Jarikov, D. Y. Kondakov, and C. T. Brown, Journal of Applied Physics **102** (2007).

[114] M. Thompson, MRS Bulletin **32,** 694-701 (2007).

[115] M. A. Baldo, D. F. O'Brien, M. E. Thompson, and S. R. Forrest, Physical Review B **60,** 14422-14428 (1999).

[116] S. Lamansky, P. Djurovich, D. Murphy, F. Abdel-Rezzaq, H.-E. Lee, C. Adachi, P. E. Burrows, S. R. Forrest, and M. E. Thompson, Journal of the American Chemical Society **123,** 4304-4312 (2001).

[117] F. Dimroth and S. Kurtz, MRS Bulletin **32,** 230-235 (2007).

[118] J. M. Olson, D. J. Friedman, and S. Kurtz, in *Handbook of Photovoltaic Science and Engineering*, edited by A. Luque and S. Hegedus (John Wiley & Sons, 2003).

[119] C. W. Tang and S. A. VanSlyke, Applied Physics Letters **51,** 913-915 (1987).

[120] Y. Kawamura, J. Brooks, J. J. Brown, H. Sasabe, and C. Adachi, Physical Review Letters **96,** - (2006).

[121] C. Baur, A. W. Bett, F. Dimroth, G. Siefer, M. Meuw, W. Bensch, W. Kostler, and G. Strobl, Journal of Solar Energy Engineering-Transactions of the ASME **129,** 258-265 (2007).

[122] R. P. Gale, R. W. McClelland, D. B. Dingle, J. V. Gormley, R. M. Burgess, N. P. Kim, R. A. Mickelson, and B. F. Stanbery, in *High-efficiency GaAs/CuInSe2 and AlGaAs/CuInSe2 thin-film tandem soalr cells*, Kissimimee, 1990, p. 53-57.

[123] S. H. Demtsu and J. R. Sites, in *Quantification of Losses in Thin-Film CdS/CdTe Solar Cells*, Cape Canaveral, 2005, p. 347-350.

[124] J. Palm, V. Probst, W. Stetter, R. Toelle, S. Visbeck, H. Calwer, T. Niesen, H. Vogt, O. Hernandez, M. Wendl, and F. H. Karg, Thin Solid Films **451-52,** 544-551 (2004).

[125] A. R. Burgers, L. H. Slooff, R. Kinderman, and J. A. M. Roosmalen, in *Modeling of luminescent solar concentrators by raytracing*, Barcelona, 2005, p. 394-397.

[126] A. J. Chatten, K. W. J. Barnham, B. F. Buxton, N. J. Ekins-Daukes, and M. A. Malik, Solar Energy Materials and Solar Cells **75,** 363-371 (2003).

[127] A. A. Earp, G. B. Smith, P. D. Swift, and J. Franklin, Solar Energy **76,** 655-667 (2004).

[128] S. J. Zoha, S. Ramnarain, J. P. Morseman, M. W. Moss, F. C. T. Allnut, Y. H. Rogers, and B. Harvey, Journal of Fluorescence **9,** 197-208 (1999).

[129] M. A. Green, *Solar Cells* (Prentice Hall, 1982).

[130] Emcore, in *Press Release: http://www.emcore.com/news/release.php?id=163 Accessed February 5, 2008.* (2007).

[131] S. A. Ringel, J. A. Carlin, C. W. Leitz, M. Currie, T. Langdo, E. A. Fitzgerald, M. Bulsura, D. M. Wilt, and E. V. Clark, in *III-IV space solar cells on Si substrates using graded GeSi buffers*, Glasgow, 2000.

[132] J. M. Zahler, C. G. Ahn, S. Zaghi, H. A. Atwater, C. Chu, and P. Iles, Thin Solid Films **403,** 558-562 (2002).

[133] T. A. Langdo, C. W. Leitz, M. T. Currie, E. A. Fitzgerald, A. Lochtefeld, and D. A. Antoniadis, Applied Physics Letters **76,** 3700-3702 (2000).

[134] J. Z. Li, J. Bai, J. S. Park, B. Adekore, K. Fox, M. Carroll, A. Lochtefeld, and Z. Shellenbarger, Applied Physics Letters **91,** - (2007).

[135] M. Yamaguchi, A. Yamamoto, M. Tachikawa, Y. Itoh, and M. Sugo, Applied Physics Letters **53,** 2293-2295 (1988).

[136] Z. I. Kazi, P. Thilakan, T. Egawa, M. Umeno, and T. Jimbo, Japanese Journal of Applied Physics Part 1-Regular Papers Short Notes & Review Papers **40,** 4903-4906 (2001).

[137] N. Hayafuji, M. Miyashita, T. Nishimura, K. Kadoiwa, H. Kumabe, and T. Murotani, Japanese Journal of Applied Physics Part 1-Regular Papers Short Notes & Review Papers **29,** 2371-2375 (1990).

[138] C. Algora, in *Next generation photovoltaics: high efficiency through full spectrum utilization*, edited by A. Martí and A. Luque (Institute of Physics, Bristol, 2004), p. 123.

[139] iSuppli, "Organic Light Emitting Diode Displays," (2007).

[140] I. G. Hill, A. Kahn, Z. G. Soos, and R. A. Pascal, Chemical Physics Letters **327,** 181-188 (2000).

[141] M. A. Baldo, S. Lamansky, P. E. Burrows, M. E. Thompson, and S. R. Forrest, Applied Physics Letters **75,** 4-6 (1999).

[142] Y. Sun, C. Borek, K. Hanson, P. I. Djurovich, M. E. Thompson, J. Brooks, J. J. Brown, and S. R. Forrest, Applied Physics Letters **90,** - (2007).

[143] G. Li and J. Shinar, Applied Physics Letters **83,** 5359-5361 (2003).

[144] T. H. Liu, C. Y. Iou, S. W. Wen, and C. H. Chen, Thin Solid Films **441,** 223-227 (2003).

[145] C. W. Chang, Y. T. Kao, and E. W. G. Diau, Chemical Physics Letters **374,** 110-118 (2003).